Materials Today 90 (2025) 598–628

Contents lists available at ScienceDirect

Materials Today

journal homepage: www.elsevier.com/locate/mattod

Advances in metastable phase catalysis with thermodynamic-kinetic adaptability

Yuanming Zhang [a,b], Yang Li [a], Yong Chen [c], Xiaoming Xu [a], Zhonghua Li [a], Tianxi Zhang [b], Wei Li Ong [b], Sergey M. Kozlov [d], Zhigang Zou [a], Ghim Wei Ho [b,e,*], Zhaosheng Li [a,**]

[a] Collaborative Innovation Center of Advanced Microstructures, National Laboratory of Solid State Microstructures, College of Engineering and Applied Sciences, Nanjing University, 22 Hankou Road, Nanjing 210093, China
[b] Department of Electrical and Computer Engineering, National University of Singapore, Singapore 117583 Singapore
[c] School of New Energy, Nanjing University of Science and Technology, Jiangyin 214400, China
[d] Department of Chemical and Biomolecular Engineering, National University of Singapore, Singapore 119260 Singapore
[e] Department of Materials Science and Engineering, National University of Singapore, Singapore 117575 Singapore

ARTICLE INFO

Keywords:
Metastable phase catalysis
Metastability
Phase transformation
Thermodynamic-kinetic adaptability
Machine learning

ABSTRACT

Owing to their unique electronic structures and extraordinary physicochemical properties, metastable phase materials are rapidly emerging as key players in catalysis, energy storage, and biological systems. These properties can be readily tailored by selecting specific crystal phases to avoid chemical complexity. Nevertheless, a critical impediment to the practical application of metastable phases lies in their inherent thermodynamic instability and unpredictable kinetics during both growth and reaction processes, rendering them highly susceptible to phase transitions from high-energy to more stable, low-energy structures. In this review, we first present the thermodynamic-kinetic adaptability of metastable phase materials that bridges the gap between experimental observations and theoretical predictions. We then provide state-of-the-art insights into the synthesis and applications of metastable phase materials and summarize key topics related to metastable phase catalysis (MPC). The high Gibbs free energy and the easily adjustable d-band center associated with metastable phases demonstrate excellent reactivity in photocatalysis, electrocatalysis, thermal catalysis and cross catalysis. We propose future directions for the field including advancements in preparation technologies, stabilization strategies and diverse applications. Additionally, we present the discussion on the discovery of metastable phase materials using machine learning and its implications for catalytic properties. This review provides valuable insights for developing systematic approaches to metastable phase materials, unlocking their immense potential for practical applications.

Introduction

The pursuit to minimize chemical complexity in the engineering of materials with new functions and properties has led to a sustained focus on phase diversity, encompassing both metastable and thermodynamically stable phases. Specifically, metastable phase engineering stands out as a powerful approach to improve material performance without resorting to compositionally complex strategies such as extensive doping, hybridization, or multi-element alloying. By identifying and stabilizing metastable polymorphs of thermodynamically stable materials, researchers can preserve the inherent chemical simplicity of the parent compound while unlocking novel or enhanced functionalities that are otherwise difficult to achieve. Metastability is characterized by a Gibbs free energy higher than that of the equilibrium state, persisting under kinetic constraints, and can be classified as thermodynamic (kinetically trapped) or dynamic (sustained only under non-equilibrium conditions). With advances in materials science, thermodynamically metastable phases now span from metals and compounds to frameworks and other crystalline polymers, while dynamically metastable systems include single-atom, high-entropy, and responsive framework materials.

* Corresponding author at: Department of Electrical and Computer Engineering, National University of Singapore, Singapore 117583, Singapore.
** Corresponding author.
E-mail addresses: elehgw@nus.edu.sg (G.W. Ho), zsli@nju.edu.cn (Z. Li).

https://doi.org/10.1016/j.mattod.2025.08.033
Received 4 July 2025; Received in revised form 19 August 2025; Accepted 31 August 2025
Available online 11 September 2025

Throughout this process, thermodynamic equilibrium phase diagrams provide essential predictive insights into the stable phases as a function of various state properties such as temperature, pressure, and chemical composition [1–3]. However, metastable kinetically trapped phases with positive free energies higher than the equilibrium state are far more numerous than low-energy phases [4]. To expand on this, when the phase diagram is complex, the source material often starts from the periphery of the phase diagram, generating more metastable phases as it transforms toward the target phase. The magnitude of the thermodynamic driving force is an effective descriptor of phase transition kinetics, and a phase transition occurs when this proxy changes. Metastable phase materials attract scientific attention not only due to thermodynamic-kinetic factors during their growth [5–8], but also as promising catalysts because of their distinct properties [9–17], high-energy structures [18–22], and unique electronic environments [23–26]. An impressive example is the anomalous Nernst effect observed at the intersection of Fermi liquid and strange metal phases in topological superconductors represented by metastable 2M-WS_2.

Metastable phase is capable of adapting to the driving forces of nucleation and growth, rather than directly transforming into the corresponding stable crystal phase. Moreover, in actual catalytic reactions, the geometric and electronic structure of the metastable phase can adapt to the adsorption and desorption of foreign molecules, optimize the reaction barrier, and accelerate the reaction kinetics. Therefore, metastable phase materials essentially exhibit unprecedented potential in various reactions as shown in Fig. 1. The tunable electronic structures and diverse chemical transformations of metastable phases facilitate a wide range of catalytic processes, central to the topic of MPC, including photocatalysis (PC), electrocatalysis (EC), thermal catalysis (TC) and cross catalysis (CC), which are distinguished by multiple forms of energy, such as photoelectrocatalysis, photothermal catalysis, etc. [27–31]. The clear advantages include a stronger charge transfer effect in electrocatalytic reactions, a tunable d-band center, enhanced light absorption and long-lived carrier excitation in photocatalytic processes, and optimized desorption and activation energies in thermocatalytic reactions.

This review begins with an overview of metastability, summarizing both traditional thermodynamic and dynamic perspectives to regulate the development of new materials. Then it not only summarizes the atomic-level mechanisms involved in the synthesis and stabilization of metastable phase materials, but also elaborates on their inherent advantages through the lens of thermodynamic-kinetic adaptability in a

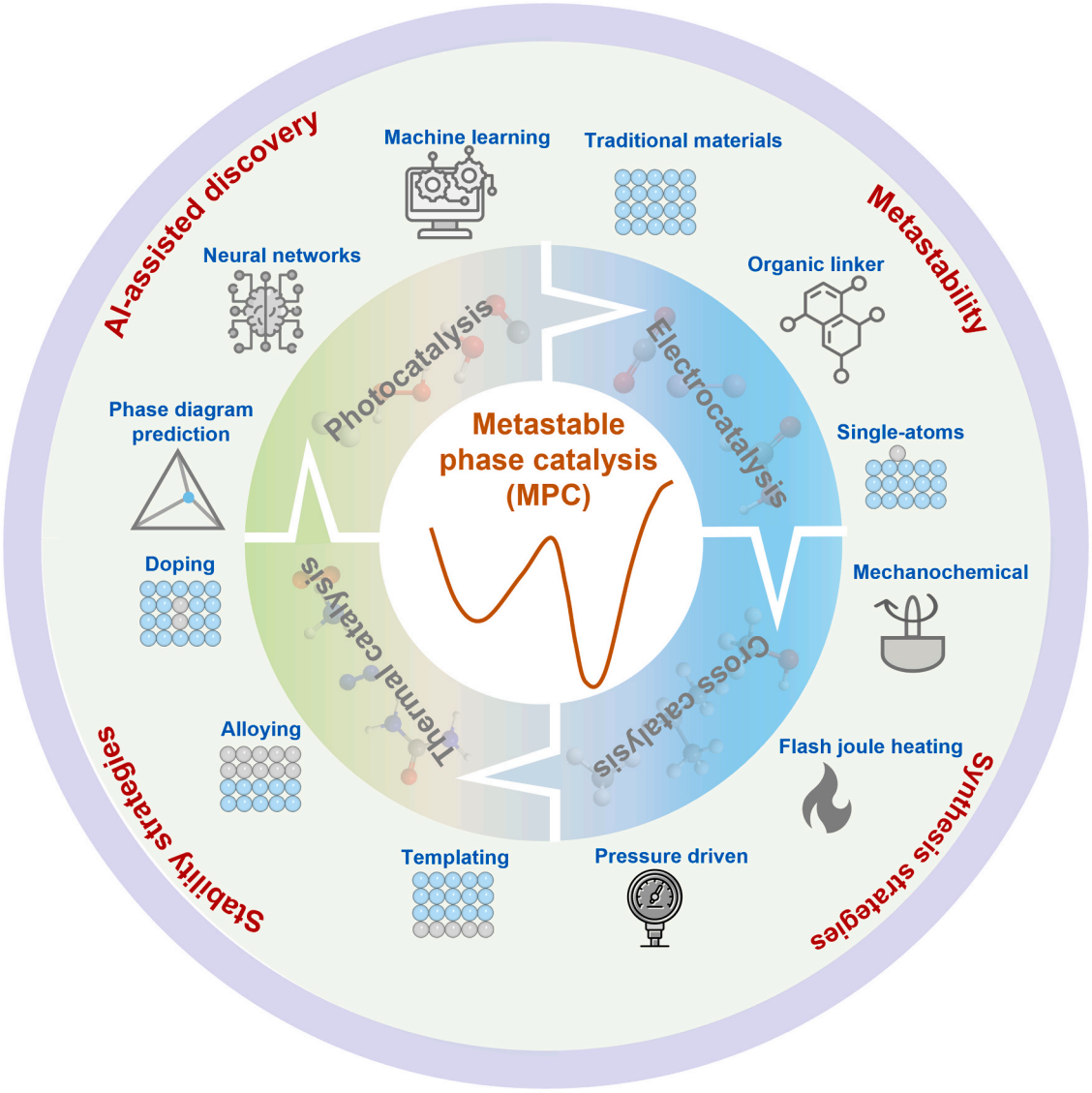

Fig. 1. Schematic diagram of the main content for MPC in this review.

wide range of energy-driven catalytic processes. Notably, their strong interaction with reactant molecules can be attributed to the easily tunable d-band center and high Gibbs free energy characteristic of metastable phase materials. In particular, there is growing interest in leveraging artificial intelligence (AI) technology to guide the discovery of new metastable phase materials, while also exploring its implications for catalytic development. Moreover, we also discuss several challenges and prospects regarding the future development of MPC. Finally, we outline the development roadmap for metastable catalysis. This review aims to offer fresh insights into metastable phase materials and to assist researchers in related fields in gaining a deeper understanding of their catalytic applications.

Metastability

The impact of metastability research

To date, metastable materials have been extensively investigated for catalytic applications, achieving enhanced yields and selectivities through crystal phase engineering and tailored interactions with reactant molecules (Fig. 2a, b). With the advancement of novel research techniques and theoretical frameworks, such as high-resolution electron microscopy for identifying materials reconstructions, the true active phases in catalytic reactions can be more accurately revealed [28,29,32–34]. Meanwhile, theoretical approaches are driving the

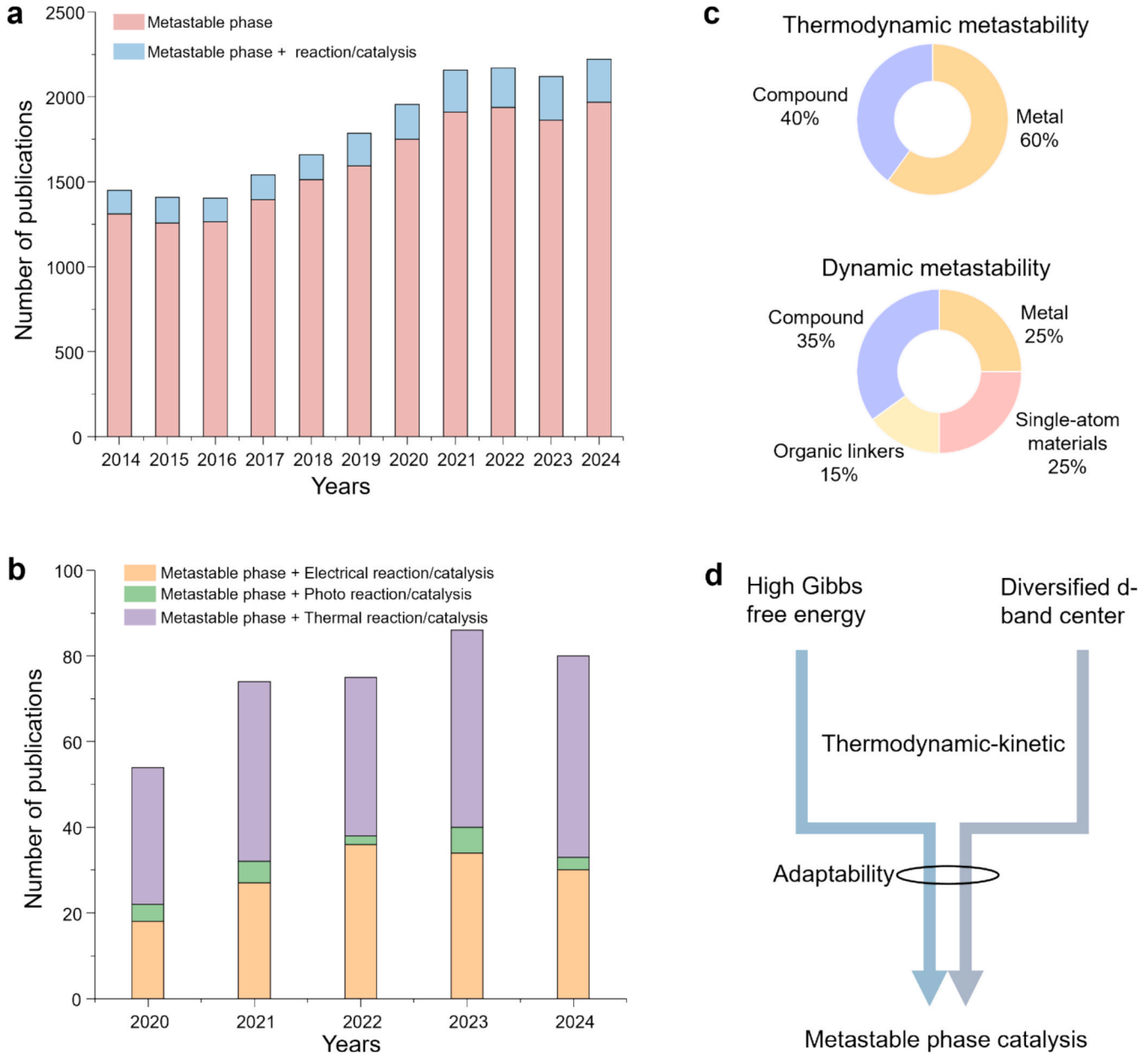

Fig. 2. Evaluation of the significance of the review on metastable phase catalysis. (a) The number of publications over the past ten years based on various keywords in the web of science database. The data was sourced from the Web of Science using the search keyword "Metastable phase" and "Metastable phase + reaction/catalysis". (b) The number of publications over the past five years based on various catalytic scenarios in the web of science database. The keywords are "Metastable phase + Electrical reaction/catalysis", "Metastable phase + Photo reaction/catalysis" and "Metastable phase + Thermal reaction/catalysis", respectively. (c) Transition from thermodynamic to dynamic metastability driven by the emergence of new materials. These data are based on a straightforward classification of the above literature and serve to illustrate the developmental trends of metastability. (d) Metastable phase catalysis is characterized by inherently high Gibbs free energy and diverse d-band centers, providing a foundation for unifying the concept of metastability across different catalytic systems.

prediction and synthesis of new materials, facilitating the transition from conventional thermodynamic metastable phases in metals and compounds to emerging dynamic metastable phase materials (Fig. 2c) [35–40]. In recent years and moving into the future, dynamic metastable phases are expected to play an increasingly prominent role in materials research, offering a pathway to reduce reliance on traditional materials.

From a catalytic perspective, metastable phases are distinguished by their inherently high Gibbs free energy and diverse d-band center configurations. Despite this growing attention, the interconnections among various catalytic forms and the key directions for future development remain insufficiently systematized and lack clear application frameworks. Drawing on years of research in metastable material catalysis and integrating insights from the broader scientific community, our team employs thermodynamic–kinetic adaptation to elucidate the unique advantages of metastable materials (Fig. 2d). This review acts as a roadmap for metastable phase catalysis, offering insights from synthesis to functional transitions and guiding future research with atomic-level and AI-enabled strategies.

From thermodynamic metastability to dynamic metastability

Metastability plays a crucial role in determining the properties and behavior of materials, ranging from traditional systems to emerging advanced frameworks. Thermodynamic metastability refers to a state in which a system resides in a local minimum of free energy but not in global minimum. At the atomic level, metastability arises due to kinetic energy barriers required for atomic rearrangements. These barriers originate from bonding energies, nucleation mechanisms and diffusion limitations, resulting in various atomic stacking structures such as SC, BCC, HCP and FCC (Fig. 3a). With the emergence of novel materials, thermodynamic metastability alone can no longer fully describe material behavior. Dynamic metastability is not solely determined by the system's thermodynamic or kinetic factors but is instead sustained by a continuous external drive, such as periodic excitation, fluid flow, magnetic fields, or electric fields. As long as the external drive persists, the system remains in a metastable state; however, once the drive is removed, the system will likely decay into a stable state. As shown in Fig. 3b, periodic structural units within soft matter materials undergo twisting and deflection under external field stimulation, characterised

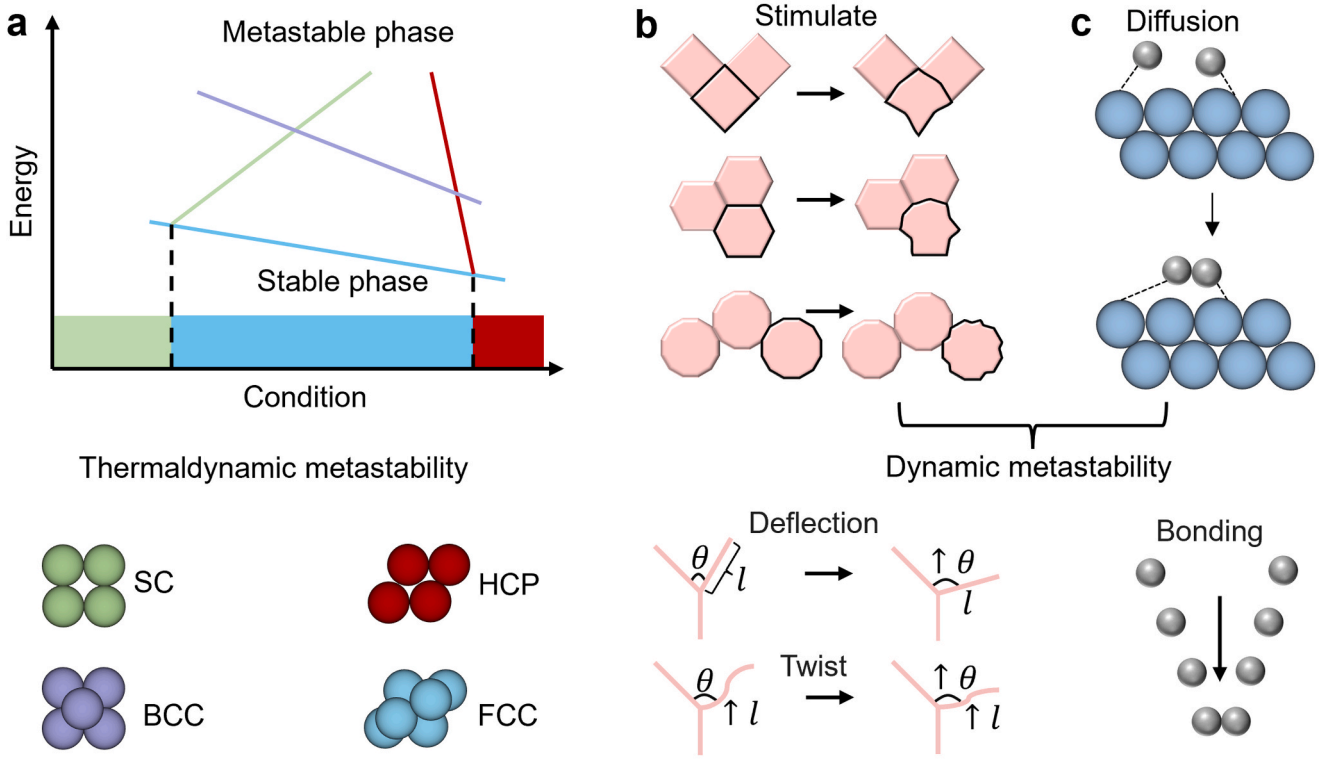

Fig. 3. Schematic diagram of metastability including conventional thermodynamic metastability and emerging dynamic metastability. (a) Conventional thermodynamic metastability is primarily governed by thermodynamic factors during material growth, exemplified by typical SC (simple cubic), BCC (body-centered cubic), HCP (hexagonal close-packed) and FCC (face-centered cubic). Adapted with permission [3]. Copyright 2024, Springer Nature. (b) Emerging dynamic metastability involves the deflection, twisting for soft matter materials, and (c) diffusion bonding of structural units for single atom materials induced by external stimuli. θ and l represent the deflection angle twisted length, respectively. (d) Comparison of material descriptions based on thermodynamic metastability and dynamic metastability.

by the deflection angle (θ) and the twisting bond length (l). Another example (Fig. 3c) demonstrates that single atoms on a substrate surface can also exhibit dynamic metastability. Under an external field, these atoms tend to diffuse and form bonds, resulting in changes to their local coordination environments and electronic structures. Based on the above summary, we describe a thermodynamic metastable state as a condition in which a material resides in a local, rather than global, minimum of free energy. In contrast, a dynamic metastable state refers to a non-equilibrium condition where the material's structure remains temporarily stable under continuous external stimuli such as electric fields, light excitation, strain, or pressure (Fig. 3d).

From thermodynamic metastable phases to dynamic metastable phases

In the current research paradigm, the emergence of new technologies has expanded the concept of metastable phases, reshaping the landscape of materials science. As illustrated in Fig. 4a, a broad range of materials can be classified as metastable phases, spanning from conventional all-inorganic and inorganic–organic hybrid materials to emerging organic materials. Conventional elementary substance (ES) and compounds (CP) constitute a thermodynamic metastable phase (TMP) material library that encompasses all seven crystal systems including triclinic, monoclinic, orthorhombic, tetragonal, hexagonal, trigonal and cubic. Additionally, emerging materials composed of organic linkers such as polymers, metal–organic frameworks (MOFs), covalent-organic frameworks (COFs), H-bonded organic frameworks (HOFs) and single-atom (SA) materials exist in dynamic metastable phases (DMP) due to their highly variable coordination configurations. As shown in Fig. 4b and c, from the perspective of the free energy landscape, TMP materials typically undergo a unidirectional transition from a higher energy metastable state to a lower-energy stable state [41]. In contrast, DMP materials experiences a dynamic, bidirectional transitions, sustained by continuous external stimuli.

Thermodynamic-kinetic adaptability

The unique structures of metastable phase materials enable various applications, particularly in catalytic reactions, where active centers and electronic structures are influenced by both thermodynamic and kinetic factors. To further simplify the analysis, we define this characteristic as thermodynamic-kinetic adaptability. Firstly, one approach to determining the synthesis conditions including pH, concentration and redox potential for metastable phase materials is to minimize the relative free energy difference between the desired phases and competing phases [3]. Generally, thermodynamic driving forces appear in kinetic equations governing nucleation, diffusion, and growth, which indicates that these processes are irreversible. However, the kinetic rates of nucleation and growth can be adapted to the reaction environment and can also be artificially manipulated. This makes it possible to synthesize phase-pure metastable phase materials in a stable manner, either by increasing free energy of phase transition (ΔG) or by decreasing nucleation or diffusion rates, by taking advantage of thermodynamic-kinetic adaptability during growth (Fig. 5a and b). From the perspective of size effects, it is widely recognized that decreasing the dimensions of nanomaterials leads to a marked increase in their surface energy, which plays a pivotal role in modulating the equilibrium dispersity of metastable phase materials. This mechanism effectively counterbalances the inherent thermodynamic propensity of the synthesized material for phase

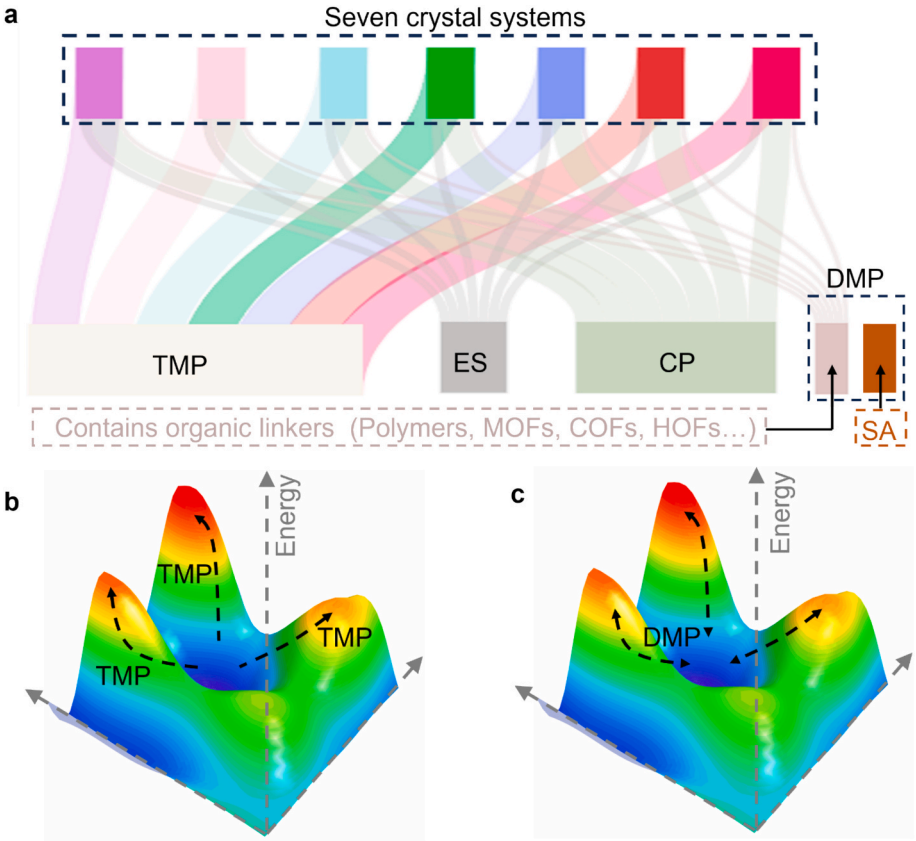

Fig. 4. Schematic diagram illustrating the differentiation between TMP materials and DMP materials based on their energy landscapes. (a) Classification of TMP and DMP materials. (b) TMP materials eventually transform into a stable energy state; in other words, it cannot undergo reversible transformations within the same energy regime. The blue well represents the metastable phase. Adapted with permission [41]. Copyright 2020, Wiley-VCH. (c) DMP materials remain in a dynamic energy state; in other words, it can undergo reversible transformations within the same energy regime. The blue well represents the metastable phase. (For interpretation of the references to colour in this figure legend, the reader is referred to the web version of this article.)

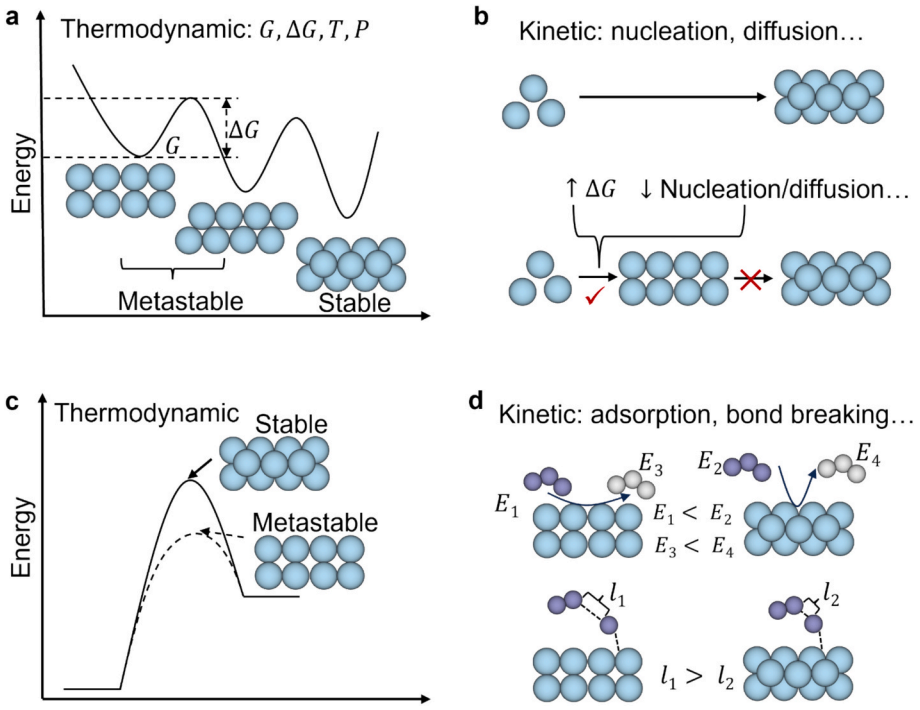

Fig. 5. Thermodynamic-kinetic adaptability in the growth and catalytic applications of metastable phase materials. (a) Metastable phase materials exhibit thermodynamic preferred gowth pathway. Adapted with permission [42]. Copyright 2021, American Chemical Society. (b) Metastable phases can be synthesized by increasing the free energy barrier for phase transitions (ΔG) or by reducing nucleation and diffusion rates, which represents a kinetic preferred gowth pathway. (c) Metastable phase materials exhibit thermodynamic preferred catalysis reaction process. (d) Metastable phase materials exhibit enhanced adsorption (E_1), desorption (E_3), and chemical bond dissociation (l_1) of reactant molecules in catalytic processes compared to the stable phase, which represents a kinetic preferred catalysis reaction process.

transformation, thereby stabilizing the metastable phase through an intricate balance of energetic and structural optimization. Structural optimization involves reducing surface energy and internal stress through factors such as atomic arrangement and lattice defects in nanomaterials, thereby enhancing the stability of metastable phases. This balance is not merely an energy minimization process, but a complex interplay of structural factors and external conditions, including stress, temperature, and chemical environment.

For different catalytic reactions, the developed metastable phase materials exhibit multiple advantages, primarily stemming from their intrinsically high Gibbs free energy and the diversity of d-band centers. (1) The inherently high Gibbs free energy of metastable phase materials corresponds to increased surface reactivity, as the system tends to minimize its free energy through interactions with adsorbates. As a result, metastable phase catalysts frequently exhibit higher adsorption energies for reactant molecules, thereby facilitating bond activation steps that are rate-limiting in catalytic processes. Moreover, the thermodynamic driving force associated with the high Gibbs free energy can promote surface reconstruction or local rearrangements under reaction conditions, leading to the dynamic formation of transient active sites. For example, if both molecular adsorption and desorption energies are simultaneously reduced, the conversion rate of reactants and the selectivity of products can be effectively balanced (Fig. 5c and d). These features are particularly advantageous for reactions requiring flexible surface environments, such as redox or multi-electron transfer processes. Thus, the non-equilibrium nature of metastable phases, while energetically unfavorable in bulk, becomes a strategic asset in heterogeneous catalysis. (2) The diversity of d-band centers in metastable phase structures plays a critical role in tuning catalytic activity and selectivity. In transition-metal-based catalysts, the position and shape of the d-band center relative to the Fermi level directly influence the adsorption strength of reactants and intermediates. Metastable structures often exhibit distorted coordination environments, lattice strain, or altered symmetry, all of which lead to a broader distribution or splitting of d-band states. This results in multiple active sites with distinct electronic properties, allowing the catalyst to simultaneously optimize adsorption for different reaction steps or species. Such d-band diversity can lower activation barriers, suppress side reactions, and enhance reaction pathways that are inaccessible on stable-phase catalysts.

Catalysis-related keywords

We introduce a comprehensive set of catalysis-related keywords, elucidating their complex interrelations as depicted in Fig. 6a. These keywords obtained through data-driven methodologies include not only bond length, bond angle, and spin configuration, but also other critical structural, electronic, and thermodynamic parameters. Catalytic processes, characterized by a range of energy input modalities, serve to rigorously test the nuanced properties of materials. In particular, cross catalysis encompasses a vast array of factors influencing reaction mechanisms, with crystal structure variations playing a pivotal role.

As shown in Fig. 6b, yield and selectivity are critical metrics in catalytic processes. We have systematically analyzed the influence of different energy modalities on these parameters, providing valuable insights to guide researchers in tailoring material properties for specific reaction objectives. For instance, the emerging modulation of transition metal spin configurations has demonstrated a profound impact on reaction yield and selectivity across photothermal and electrochemical domains. This effect is primarily attributed to variations in orbital electron occupancy and can be explained using d-band center theory. The intrinsic advantages of metastable phases over their stable counterparts in enhancing the yield and selectivity of catalytic reactions are summarized here under consistent reactor configurations and electrolyte compositions. Future studies on electrolyte-involved reactions should also focus on the interactions between electrolyte composition, such as ion species, pH, and buffering capacity, and metastable surface

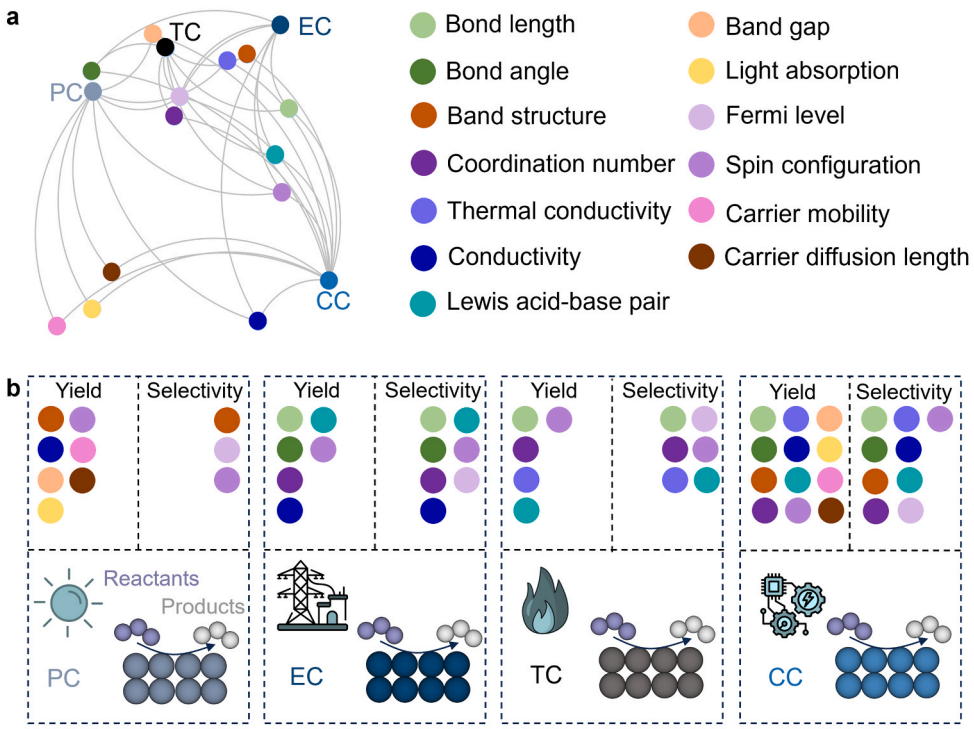

Fig. 6. Summary of the key terms related to thermodynamic-kinetic adaptability in various catalysis application. (a) Keywords and interaction networks across various catalytic scenarios, illustrating the adaptability features that distinguish metastable phases from stable phases. (b) Overview of intrinsic factors influencing yield and selectivity across various catalytic processes, namely photocatalysis (PC), electrocatalysis (EC), thermocatalysis (TC) and cross-catalysis (CC).

structures. Advanced characterization techniques and theoretical modeling can provide insights into how interfacial ion dynamics at metastable surfaces influence catalyst stability and reaction pathways. Furthermore, coupling metastable structures with tailored electrolytes, including ionic liquids or confined environments in porous or hydrophobic systems, may uncover catalytic behaviors that are not accessible in equilibrium systems. Integrating these insights presents a promising strategy to achieve more precise control over catalytic activity and selectivity.

Abundance of metastable phase materials

To demonstrate the abundance of metastable phase materials, several representative cases are selected and presented in Fig. 7. Fig. 7a shows that elemental carbon, composed solely of carbon atoms, exhibits a variety of properties due to its diverse arrangements of carbon atoms [1]. Diamond is the hardest naturally occurring substance and typically forms under high pressure; while graphite is one of the softest minerals and is usually more stable at lower pressure. Amorphous carbon, such as charcoal, coke and activated carbon, etc, lacks an unequivocal crystal structure. The polymorphs of inorganic compounds and organic materials are more complex. Just as the symmetry breaking of Ti in $BaTiO_3$ crystals gives rise to four distinct crystal forms (Fig. 7b), the diverse interpenetration of adamantane-1,3,5,7-tetracarboxylic acid (ADTA) crystals (Fig. 7c) produces an even wider range of variations than inorganic materials [43] due to dynamic metastability. In particular, materials with a higher proportion of organic molecular frameworks, exhibit more pronounced dynamic distortion or deflection under external field stimulation (Fig. 7d). Single-atom materials also differ significantly from their equilibrium and bulk phases, with high metal site dispersion imparting unique properties (Fig. 7e). However, their poor resistance to thermal agglomeration and sintering limits their application in certain specific reactions. To maintain the focus of this review, dynamic metastability will be discussed briefly.

Functional advantages of MPC

Metastable phase materials, characterized by their higher energy states, often exhibit unique structural and electronic properties that make them ideal candidates for catalytic applications. These phases possess tunable features, such as diverse atomic configurations, electronic band structures, and reaction pathways, that can be harnessed to improve catalytic efficiency and selectivity. Among the many materials explored, metal oxides have seen significant advancements due to their adaptability and multifunctional properties, making them a focal point of metastable phase research. One notable example is Fe_2O_3, an earth-abundant low-cost material, which serves as a model for analyzing the multifunctional differences between metastable and stable phases, as shown in Fig. 8a. Fe_2O_3 can exist in three space groups with varying symmetry features. The polyhedra structure which include regular octahedra, distorted octahedra, and tetrahedra, lead to significant differences in the electronic structures of these phases. These variations are crucial as they determine whether the material behaves as a direct or indirect bandgap semiconductor (Fig. 8b), a factor that greatly influences its performance in catalytic reactions. In oxide photocatalysis, as shown in Fig. 8c, minority carrier diffusion lengths typically are in the order of 5–100 nm, making the process highly sensitive to charge recombination and localization through polaronic states, which are fundamental steps in photocatalysis [46]. Polarons or charge carriers that are coupled with local distortions in the crystal lattice, can introduce energy levels within different bandgaps (Fig. 8d and e). This not only affects charge mobility but can also significantly alter the energy levels of defects when polarons bind strongly to them. Such interactions can play a critical role in optimizing catalytic performance by adjusting the energy landscape of the material.

Additionally, metastable phase materials such as Fe_2O_3 exhibit other notable advantages, including enhanced light absorption properties due to the intrinsic electronic structures. The impact of crystal field effects, coupled with spin-induced magnetic properties (Fig. 8f–h), further

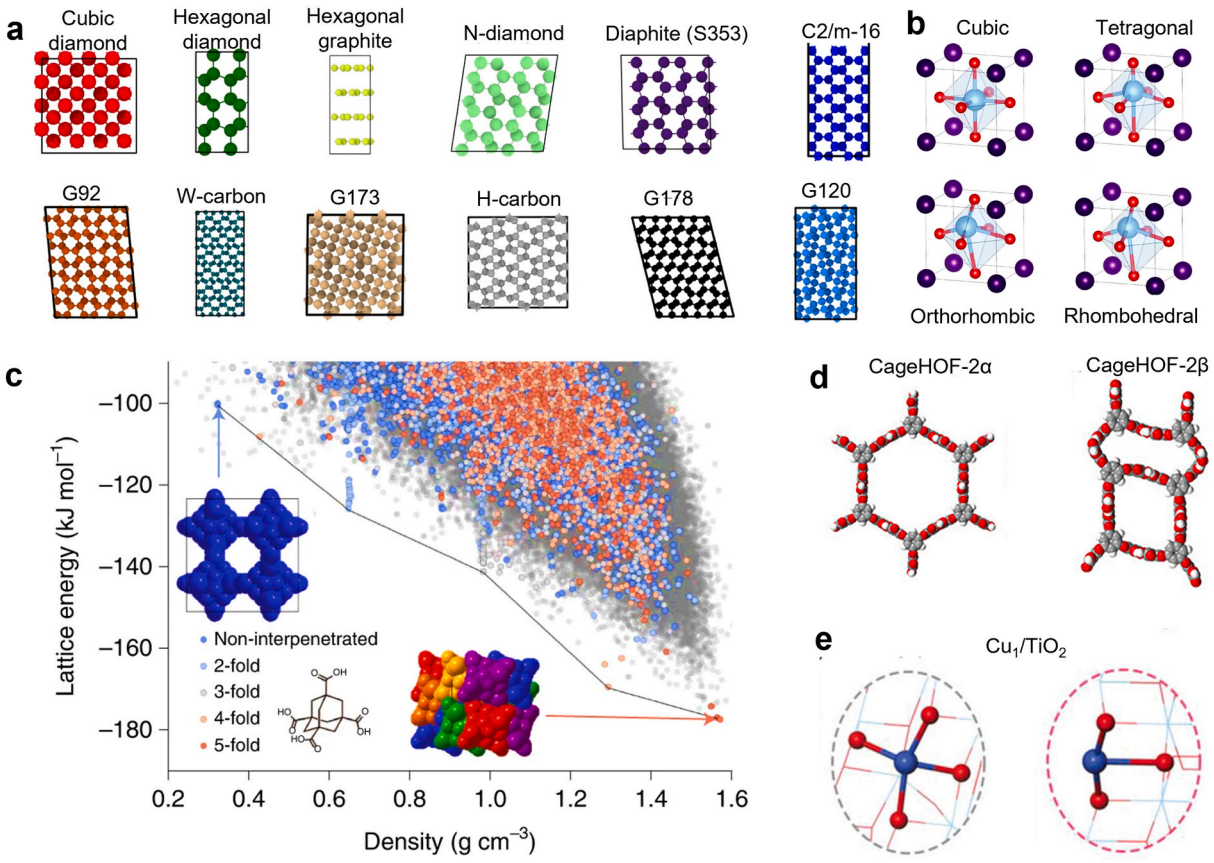

Fig. 7. Metastability of materials. (a) Metastability of elemental carbon. Reproduced with permission [1]. Copyright 2022, Springer Nature. (b) Metastability of $BaTiO_3$ due to symmetry breaking from Ti translation. Reproduced with permission [43]. Copyright 2021, Springer Nature. (c) Crystal structure prediction diagram of ADTA via an autonomous crystallography companion agent. Reproduced with permission [43]. Copyright 2021, Springer Nature. Reproduced with permission [29]. Copyright 2020, American Chemical Society. (d) Metastability of HOFs [44]. Reproduced with permission [44]. Copyright 2023, American Chemical Society. (e) Metastability of single-atom materials. [45]Reproduced with permission [45]. Copyright 2023, Wiley-VCH.

contributes to the superior functionality of metastable phases in catalysis. These factors allow metastable phase materials to demonstrate greater adaptability and tunability, making them ideal for applications requiring precise control over reaction kinetics. Overall, the ability to tailor the electronic structures and physical properties of metastable phase materials offers significant advantages at the application level. By understanding and leveraging the unique characteristics of these high-energy phases, researchers can more effectively screen and design tailored materials that deliver enhanced performance in catalytic processes. This adaptability positions metastable phases as key materials for future advancements in catalysis and related fields.

In MOFs, COFs and HOFs, structural dynamics provide several key advantages: (1) Refined pore environment: Structural dynamics modify pore geometry and size, improving molecular selectivity and diffusion efficiency. (2) Optimized adsorption and desorption: Distorted frameworks enhance interactions between reactant molecules and catalytic sites, reducing energy barriers for adsorption and desorption. (3) Greater structural flexibility: Distortions introduce dynamic adaptability, enabling the material to respond to external stimuli (e.g., temperature, pressure, or electric fields) and enhancing stability under extreme conditions. (4) Synergistic electronic effects: Local distortions facilitate charge redistribution, enhancing charge transfer and electron mobility, which is particularly beneficial for catalytic reactivity.

For example, let us consider the excited-state behavior of organic framework materials under photon stimulation. The photosensitive components absorb photons to generate excited-state electrons, which are then transferred to the final electron acceptor through a series of cofactors. These cofactors are typically spatially separated, and they undergo structural changes in their excited state when accepting electrons, thereby lowering the system's energy. This enhances the separation efficiency and extends the lifetime of the excited-state electrons (Fig. 9a). Researchers found that in Zn-MOF, under illumination, electrons are excited from one linker to another crystallographically distinct linker. Since Zn^{2+} has a closed-shell structure, there is no orbital overlap between the linkers at the conduction band minimum (CBM) and the valence band maximum (VBM). As a result, the CBM linker fully absorbs the energy of the excited electron, placing it in a high-energy state. The flexibility of the MOF linkers allows for dynamic structural distortions, which reduce the system's energy and induce corresponding MOF orbital rearrangements. As shown in Fig. 9b, this alters the potential energy surface and disrupts the relaxation path from the excited state to the original ground state. Consequently, electron-hole recombination in Zn-MOF is suppressed [48].

We further analyze the dynamic metastable properties in single-atom materials. As shown in Fig. 9c, dynamic evolution refers to changes in the position, electronic state, or chemical environment of individual atoms within a material or system over time. This evolution is influenced by factors such as temperature, pressure, external fields (e.g., electric or magnetic fields), and interactions with surrounding atoms or molecules [49–51]. Under electrical stimulation, single atoms reconstruct on the surface of the supports, enhancing electron transfer and injection capabilities of the reacting molecules. This process directly regulates the adsorption configuration of the reaction intermediates, guiding the breaking and recombination of bonds in the molecules toward the synthesis of the target product (Fig. 9d).

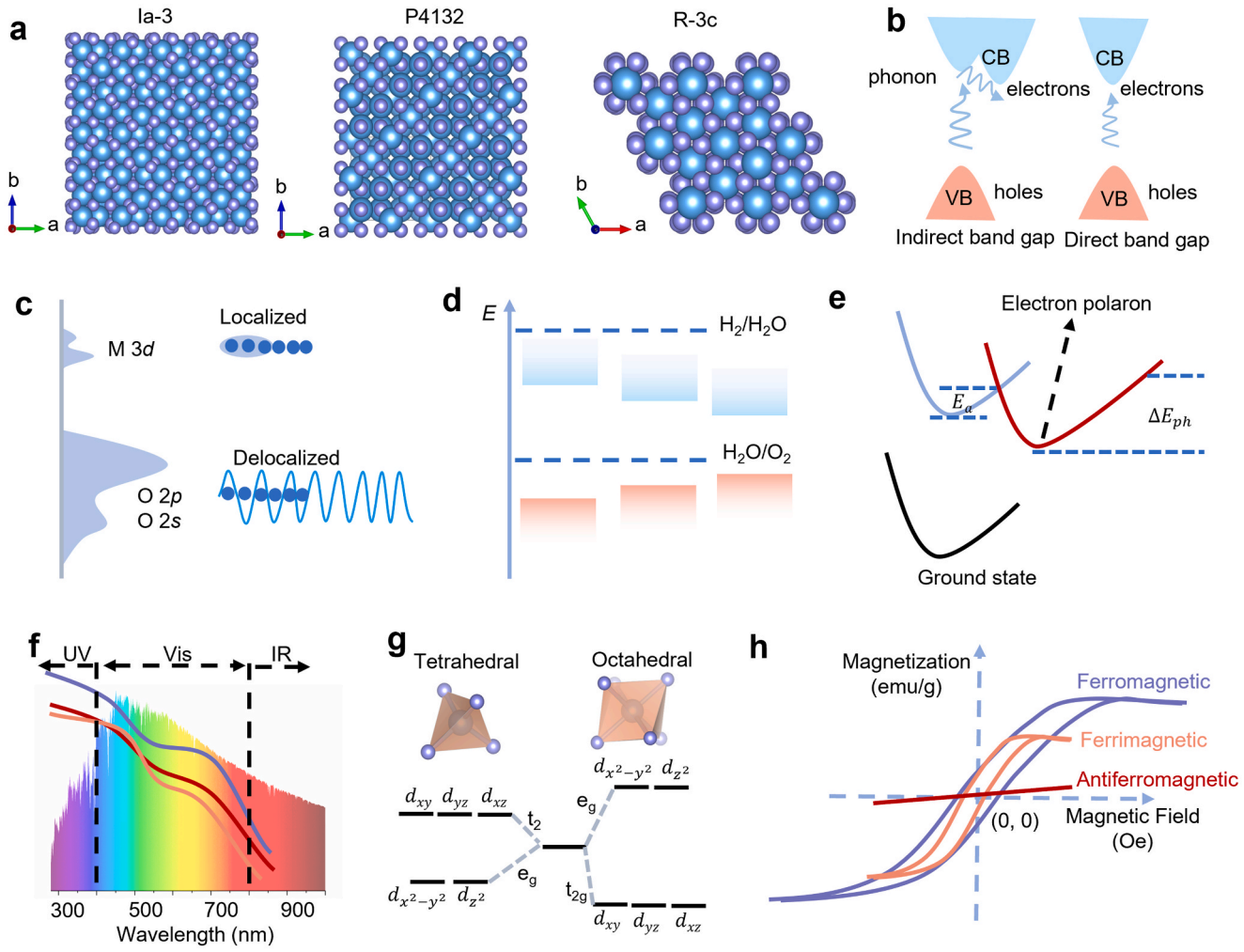

Fig. 8. Analysis of the physicochemical properties of metastable phases using Fe_2O_3 as a case study. (a) Taking the widely functionally diverse structures of Fe_2O_3 observed in nature as an example to discus the advantages of metastable phase materials. The blue balls represent Fe atoms, and the purple balls represent O atoms. From left to right, the phases shown are metastable phase β-Fe_2O_3, metastable phase γ-Fe_2O_3 and stable phase α-Fe_2O_3. (b) Differences in the electronic structure caused by variations in the crystal structure. (c) Charge localization in the form of polarons. Reproduced with permission [46]. Copyright 2022, Springer Nature. (d) Differences in the band structures of semiconductors based on the thermodynamic requirements of water splitting. (e) Configuration coordinate diagram of polaron formation in metal oxides. E_a represents the activation barrier generated by the polaron, and ΔE_{ph} represents the photon energy required to excite the localized state back to the band state. Reproduced with permission [46]. Copyright 2022, Springer Nature. Variation in (f) light absorption (The purple line represents metastable phase β-Fe_2O_3, the red line represents metastable phase γ-Fe_2O_3, and the yellow line represents stable phase α-Fe_2O_3), (g) spin structures induced by crystal field splitting energy (Reproduced with permission [47]. Copyright 2022, Springer Nature) and (h) magnetic properties. (For interpretation of the references to colour in this figure legend, the reader is referred to the web version of this article.)

Growth landscape of metastable phase materials

Complexity of metastable phase materials

The controlled synthesis of metastable phase materials remains a challenge, as they are typically less stable than their thermodynamically stable counterparts. However, recent advances in synthesis techniques have opened new pathways for the production of metastable phases, leveraging factors such as pressure, temperature, and chemical environments to achieve precise control over material properties. In this section, we explore various synthesis strategies along with their impact on the stabilization of metastable phase materials. In light of the scope of this review and the central focus of our research, we specifically concentrate on the metastability of inorganic materials, with the intent to drive the advancement of innovative and emerging material systems.

Before discussing synthesis strategies, it is essential to understand the prevalence and complexity of metastable phase materials. Researchers have begun to quantify these materials. The crystalline metastability properties of most materials constitute a vast database that is challenging to quantify in detail. Sun et al. quantified the thermodynamic scale of inorganic crystalline metastability through data-mining the Materials Project database using high-throughput computational materials science [4]. They found that approximately 50.5 % of the material entries filtered from 29,902 sources were metastable phases (Fig. 10a). The formation of equilibrium phases typically occurs through steady-state nucleation, following the full growth of metastable phases. If the nucleation energy of the metastable polycrystalline form is lower than that of the equilibrium phase ($\Delta G_{b\ \text{metastable}}^{2} < \Delta G_{b\ \text{stable}}$), the crystallization kinetics will be dominated by the growth of metastable phases (Fig. 10b) [42,52,53]. In the early stages of solid-state reactions, crystals grown from high-energy precursors often adopt metastable structures initially rather than forming thermodynamically stable ground state structures, depending on initial conditions such as temperature, pressure, or crystal size [54]. Before reaching the bulk equilibrium state, the materials first nucleate and grow within the nanoscale regime, where surface energy plays a crucial role. Small particle sizes with a large $1/R$

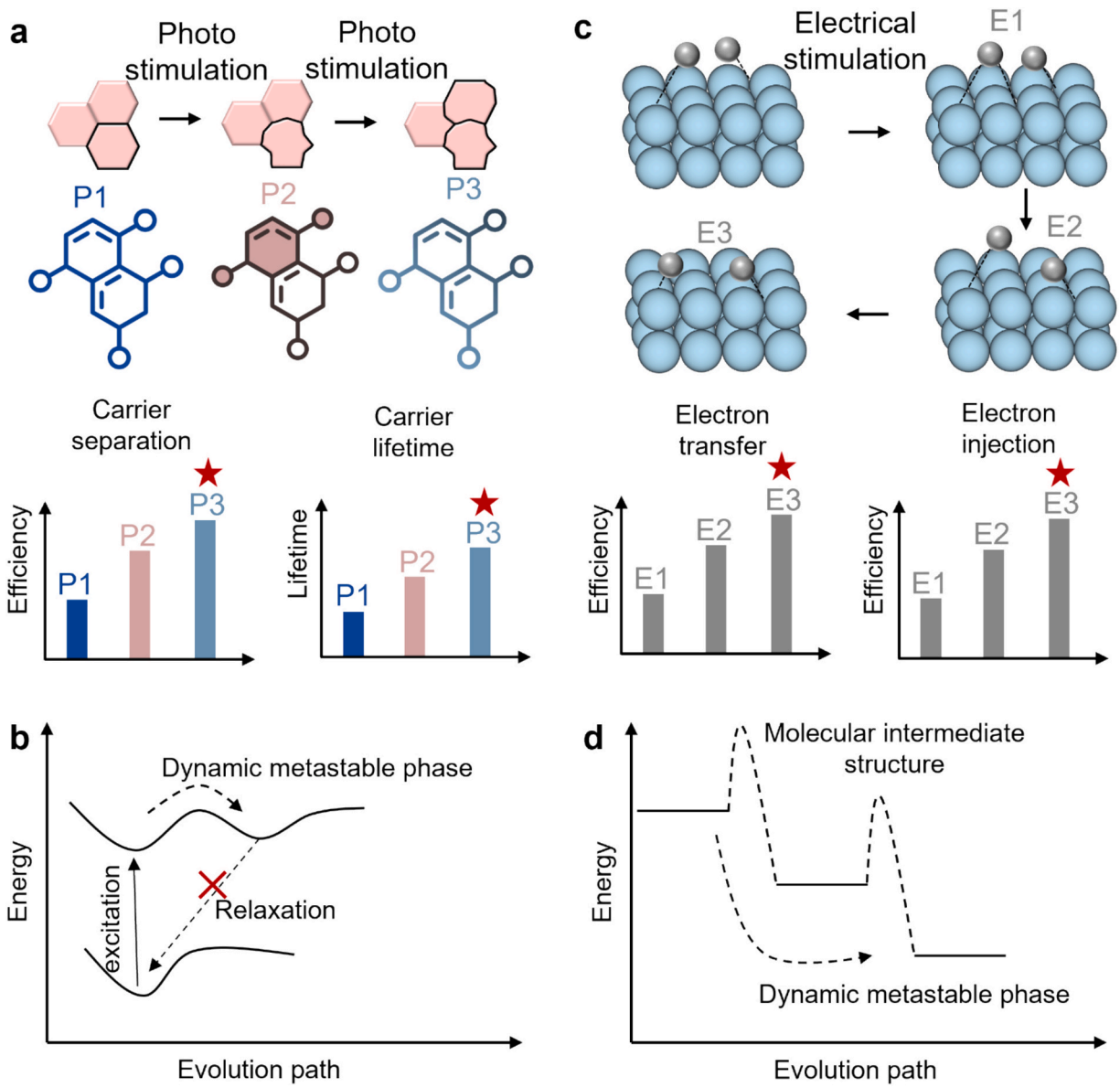

Fig. 9. Analysis of the physicochemical properties of dynamic metastable phases under photon and electrical stimulation. (a) Structural diversity of dynamic metastable phases under photo stimulation dynamics and the enhancement of carrier separation and lifetimes. P1, P2 and P3 represent different dynamic metastable phases in soft matter materials, respectively. (b) Schematic illustration of a long-lived charge-separated state in a dynamic metastable phase. Adapted with permission [48]. Copyright 2024, Springer Nature. (c) Structural diversity of dynamic metastable phases under electrical stimulation, highlighting enhanced electron transfer and injection behaviors. E1, E2 and E3 represent different dynamic metastable phases in single atom materials, respectively. (d) Schematic illustration of the optimization of molecular intermediate configuration by dynamic metastable phases.

(where R is the radius) can stabilize bulk-metastable polymorphs with lower surface energy, promoting the preferential nucleation of the metastable phase over the equilibrium phase. Starting from a supersaturated solution, a metastable phase with low surface energy will represent the lowest free-energy phase at small sizes, meaning it requires the smallest size fluctuation to nucleate. Once nucleated, the metastable phase reduces its free energy through crystal growth, consuming metal solute ions in the process. Since the barrier to crystal growth is typically lower than the barrier to nucleating a new phase, the metastable phase may continue to grow until it reaches a size where it is no longer stabilized by its small dimensions. At this stage, a thermodynamic driving force arises, favoring a phase transformation from the metastable phase to a more stable (lower free-energy) phase [55]. In order to stabilize these metastable phase materials (Fig. 10c), it is necessary to introduce external driving forces such as templates, electron donors or enhanced interfaces in the transient state [42,56,57].

Despite the discovery of various structural phases, there remains a lack of systematic and in-depth understanding, as well as effective descriptors, to accurately evaluate the complexity of materials. First-principles density functional theory (DFT) for all known inorganic crystal materials reveal that the median metastability is 15 ± 0.5 meV atom^{-1} with the highest energy structure of 20 % of entries in the inorganic crystal structure database (ICSD) being inconsistent with the observed crystalline polymorphs. The 90th percentile is 67 ± 2 meV atom^{-1}, indicating an approximately exponentially decreasing probability distribution for metastability of various proposed structures (Fig. 10d). Taking group VI compounds as an example, bivariate sample density is mapped as a function of metastability and cohesive energy, with darker regions representing higher scattering densities (Fig. 10e). The results indicate that stronger average cohesive energy in a given chemical substance corresponds to greater achievable crystal metastability. In the group VI chemistries, oxides which exhibit the strongest

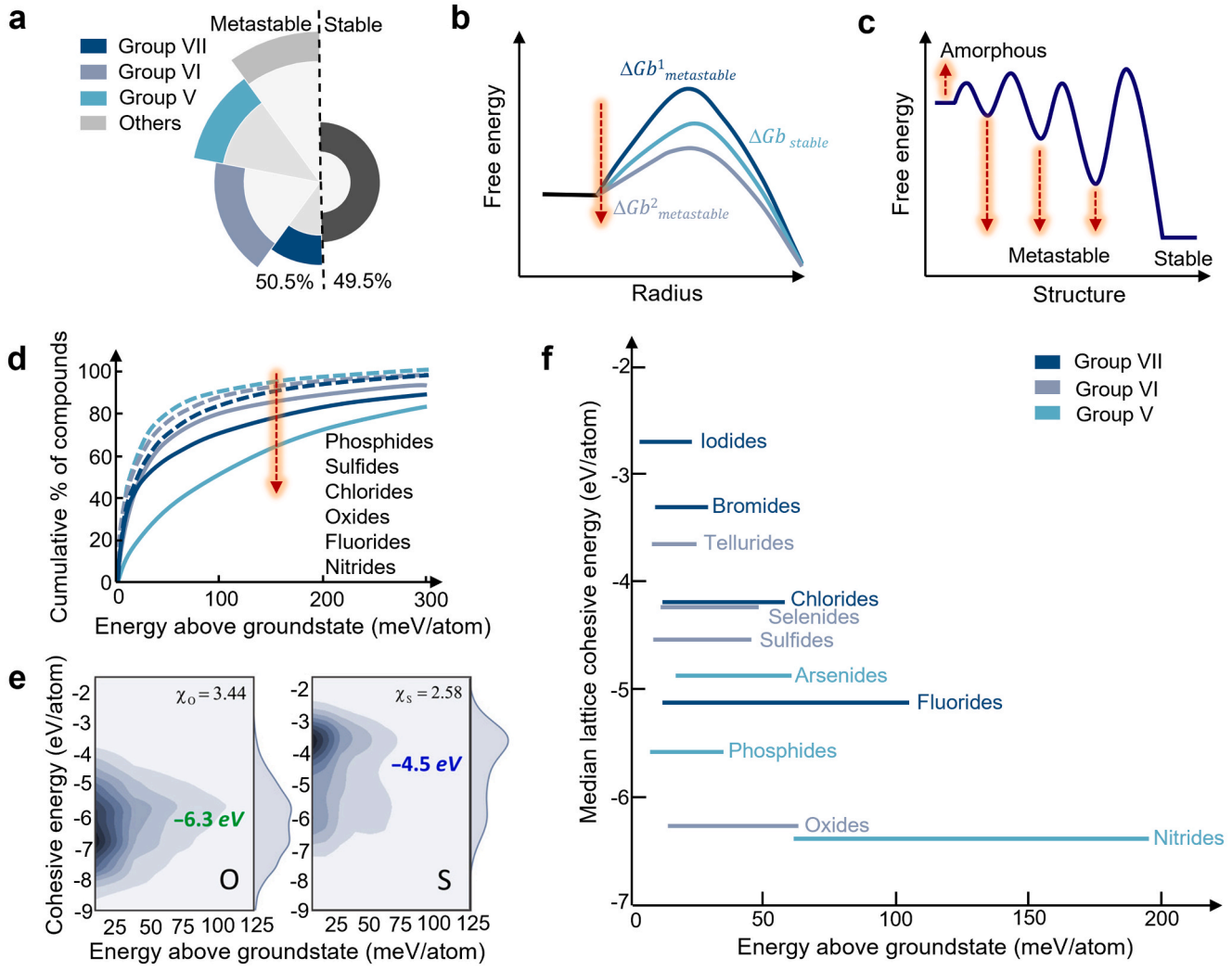

Fig. 10. Complexity of metastable phase materials. (a) Material library composed of metastable and stable phases. (b) Barriers to the nucleation of metastable and stable phases in a supersaturated solution. Reproduced with permission [42]. Copyright 2021, American Chemical Society. (c) Schematic diagram illustrating the transition pathways during the crystallization process of material. Reproduced with permission [42]. Copyright 2021, American Chemical Society. (d) Cumulative distribution function of the crystallization metastability of the most representative chemical substances in the Material Projects. Reproduced with permission [4]. Copyright 2016, the American Association for the Advancement of Science. (e) Bivariate sample density maps showing the relationship between metastability and the cohesive energy of group VI compounds. Reproduced with permission [4]. Copyright 2016, the American Association for the Advancement of Science. (f) Energy scale of metastability for various chemical substances arranged vertically according to the median cohesive energy. Reproduced with permission [4]. Copyright 2016, the American Association for the Advancement of Science.

average cohesive energy, also display the largest metastable range. As one moves down the periodic table, the decrease in average lattice cohesion leads to a smaller accessible metastable energy range [4]. We also observe that the cohesive energy becomes stronger with increasing anionic charge, which reflects the importance of electrostatic contributions to the cohesive energy. In general, the stronger the cohesive energy of a chemical compound, the higher the metastable state available, with fluorides, oxides, and nitrides showing the largest metastable energy scales in their respective groups (Fig. 10f). Researchers further expanded the scope to include all mixed ionic/covalent solids, concluding that stronger chemical cohesion energy is correlated with greater achievable metastability. Therefore, identifying effective methods to improve the metastability of materials is crucial to avoid the introduction of impurity phases during material synthesis.

Synthesis strategies

As shown in Fig. 11, current technologies for synthesizing metastable phase materials include ultrafast thermal synthesis [11,58,59], wet chemical synthesis [60,61], chemical vapor deposition [62–64], mechanochemical synthesis [65–68], high pressure phase transition synthesis [24,69] and electron/plasma-assisted synthesis [18,54].

Ultrafast thermal synthesis. Ultrafast thermal synthesis rapidly produces materials within milliseconds under non-equilibrium conditions, enabling the formation of metastable phases and controlled microstructures that are difficult to achieve with conventional methods [59,70,71]. Liu et al. [72] used a solid-state thermal shock strategy to synthesize metastable Pd nanoparticles on a carbon substrate, rich in twin boundaries and atomic steps. And molecular dynamics simulations showed that transient supercooling after the thermal shock facilitates twin boundary formation. Yang et al. [73] reported a rapid thermal shock non-equilibrium synthesis strategy to overcome the immiscibility of bimetallic materials. Using Cu-Ag and Cu-Ni systems as examples, they demonstrated the successful formation of uniformly alloyed bimetallic nanoparticles, establishing a library of such materials. Yan et al. [74] employed a Flash Joule Heating (FJH) method to synthesize $L1_2$-Pt_3Mn and $L1_0$-PtMn intermetallics with Pt-skin. Cui et al. [75] used disordered Pd_3Pb nanoparticles as precursors and obtained ordered $L1_2$-

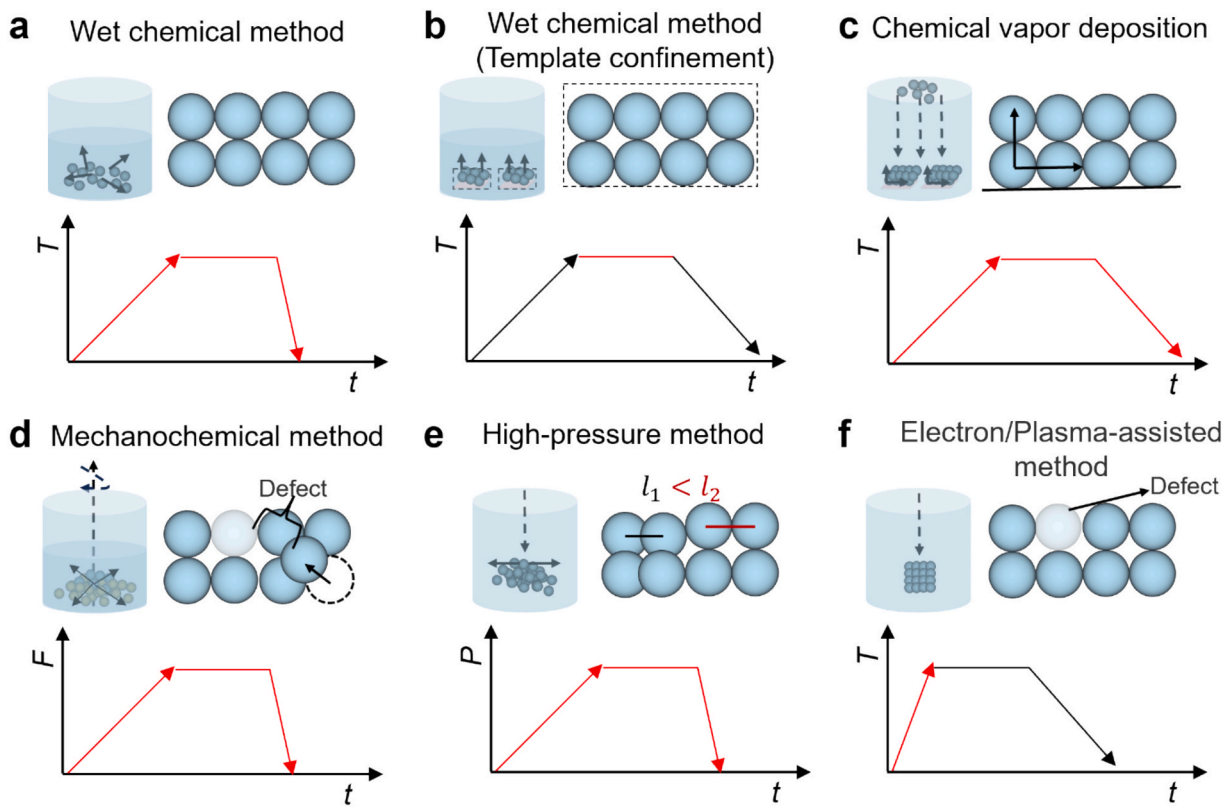

Fig. 11. Summary of the synthesis pathways for metastable phase materials. (a) The precipitation of high-purity metastable phases is primarily governed by careful control of reaction time and temperature during wet chemical synthesis. (b) The nucleation rate is suppressed by employing template confinement, facilitating the formation of a metastable phase. (c) Controlled atomic diffusion and the formation of a stable metastable phase are achieved via chemical vapor deposition. (d) The mechanochemical method applies intense mechanical energy to overcome thermodynamic constraints and diffusion limitations within a low-temperature, non-equilibrium environment, thereby inducing the formation of metastable structures that are preserved through kinetic hindrance. (e) The high-pressure method stabilizes denser phases by lowering their enthalpy, suppresses atomic diffusion, and alters the free energy landscape and reaction pathways. As a result, metastable phases that are inaccessible under ambient conditions can be formed under extreme pressure and subsequently stable at ambient pressure through techniques such as rapid decompression. (f) The electron/plasma-assisted method employs high-energy species to induce strong excitation, disrupting the material's thermodynamic equilibrium. This facilitates atomic rearrangement and enables the formation and kinetic stabilization of metastable phases under non-equilibrium, low-temperature conditions. The red line represents the primary influence of the metastable phase preparation process, while the black line indicates that the metastable phase synthesis remains largely unaffected. *T* denotes temperature, *F* denotes force, *P* denotes pressure, and *t* denotes time. The solid arrows within the cylinder indicate the direction of particle growth or movement, while the dotted arrows represent the influence of external factors. (For interpretation of the references to colour in this figure legend, the reader is referred to the web version of this article.)

phase Pd_3Pb nanoparticles with an average size of 6 nm via FJH. The abundant atomic vacancies generated during the Joule heating process promote atomic diffusion and facilitate structural ordering in the Pd_3Pb nanoparticles. Ultrafast thermal synthesis technology also offers advantages for the preparation of metastable phase compounds. Deng et al. selectively synthesized molybdenum carbides, including β-Mo_2C and metastable α-MoC_{1-x} and η-MoC_{1-x}, by controlling the pulse voltage during FJH. They demonstrated the excellent phase-engineering capability of FJH, which combines a widely tunable energy input exceeding 3000 K with dynamically controlled ultrafast cooling.

Wet chemical synthesis. During wet chemical synthesis, by adjusting reaction parameters including solvent composition, reaction temperature, and precursor concentration, metastable phases can be selectively crystallized from a solution before transitioning to their stable counterparts (Fig. 11a) [76]. The confinement effect and rapid cooling stabilizes metastable phases by limiting atomic diffusion and structural rearrangement during wet chemical synthesis (Fig. 11b). Akkerman et al. [77] synthesized highly crystalline, ultrathin metastble PbS nanosheets (~1.2 nm) via the decomposition of $Pb(SCN)_2$ in a mixture of 1-octadecene, oleylamine, and oleic acid, obtaining an orthorhombic structure with a direct bandgap and weak light absorption. Talapin et al. [78]. achieved controlled synthesis of CdSe nanocrystals in both wurtzite and zincblende phases by optimizing organic solvents. Using organic phosphonic acids (e.g., n-octylphosphonic acid and n-tetradecylphosphonic acid) as capping ligands with trioctylphosphine oxide as the solvent yielded wurtzite-phase CdSe nanocrystals. In contrast, employing oleylamine and oleic acid as capping ligands enabled the synthesis of zincblende CdSe nanocrystals through the reaction of cadmium myristate with selenium dissolved in 1-octadecene. Khannanov et al. [79] reported the synthesis of Fe nanoparticles exhibiting a FCC structure. Initially, Fe^{3+} ions complex with oxygen-containing functional groups on the graphene oxide surface in the liquid phase. Upon thermal annealing, this complex transforms into γ-Fe nanoparticles, a structure previously considered unattainable under ambient conditions.

Chemical vapor deposition. Chemical vapor deposition typically refers to the gradual pyrolysis of material precursors, layer by layer, onto a substrate in the presence of a gas, resulting in the formation of a high-energy structure (Fig. 11c). Wang et al. [80] synthesized FCC- and HCP-phase Ni nanoparticles of similar size by annealing a Ni-containing microporous metal–organic framework, $[Ni_3(HCOO)_6]$•DMF (DMF = N, N-dimethylformamide), under chemical vapor deposition conditions using hexamethylenetetramine. This approach enabled a meaningful evaluation of OER performance as a function of crystal structure. Okada et al. [81] reported the growth of atomic layers of 1 T′ WS_2 via alkali-metal-assisted chemical vapor deposition using gaseous H_2S and WF_6

precursors. The gaseous nature of the precursors, the reducing environment provided by H_2S, and the presence of Na^+ countercations together created optimal conditions for 1 T′ WS_2 growth, yielding high-quality crystals on the submillimeter scale. Zhao et al. [82] developed a ReS_2-template-assisted chemical vapor deposition strategy to synthesize layered MnS_2 microstructures, demonstrating that the template effectively directs the formation of single-layer MnS_2 with a well-defined distorted T phase.

Mechanochemical method. The above strategies typically produce metastable phase materials with high purity and excellent crystallinity. However, repeated mechanical force, such as high-energy ball milling, induces structural disorder, disrupts thermodynamic equilibrium, and stabilizes metastable phases by refining grains and increasing defect density (Fig. 11d). In a word, mechanochemistry, which employs mechanical forces to drive chemical transformations, has been shown to effectively access metastable phases that are challenging to obtain under equilibrium conditions [83]. Achimovičová et al. [84] employed high-energy ball milling of elemental Zn and Se to synthesize the wurtzite form of ZnSe, a metastable phase relative to the thermodynamically stable zinc blende structure. Ma et al. [85] employed high-energy ball milling of elemental powders to produce an immiscible metastable solid solution of Fe and Cu under equilibrium conditions. A single-phase FCC solid solution was obtained for $0 < x \leq 60$, whereas a BCC solid solution formed for $75 \leq x < 100$. Near $x \approx 70$, a transition from FCC to BCC occurs, resulting in a mixed phase comprising both FCC and BCC structures. The above examples highlight the versatility of mechanochemistry for stabilizing nonequilibrium phases across a wide range of material systems, offering promising pathways for applications in energy conversion, catalysis, and optoelectronic devices.

High-pressure method. Materials can be forced into a metastable phase by applying extreme pressures that are not typically achievable under ambient conditions (Fig. 11e). For instance, Sun et al. [86] reported two distinct structural transitions in Ag nanosheets under non-hydrostatic pressures up to 24 GPa. The local HCP structure, associated with multiple parallel twin planes, disappears at 1.03 GPa. When the external pressure reaches 12 GPa or higher, the FCC structure transforms into a face-centered tetragonal (FCT) phase. Upon release of the pressure, the metastable FCT phase reverts to the stable FCC structure. Lv et al. [87] discovered that single-crystalline Ta_2O_5 nanowires undergo pressure-induced amorphization at 19 GPa, driven by phonon softening and bond weakening. The transition originates from disrupted connectivity between TaO_6 octahedra and TaO_7 bipyramids along weak bonds on the *a*-axis. It is noteworthy that stabilizing high-pressure phases at ambient conditions remains a key challenge, but strategies like chemical pressure, interface engineering, and ultrafast quenching could kinetically trap these polymorphs, unlocking their transformative potential.

Electron/plasma-assisted method. Similarly, high-energy electron or plasma modifies atomic structures, introduces defects and stabilities metastable phases that do not typically form under equilibrium conditions (Fig. 11f). For example, gold typically crystallizes in its lowest free-energy structure, the FCC phase. However, the metastable hexagonal 4H phase of gold exhibits superior catalytic performance. Han et al. [88] employed *in situ* transmission electron microscopy to directly observe the interface expansion dynamics between 4H-Au nanorods and FCC-Au nanoparticles. Theoretical calculations suggest that CO molecules facilitate gold diffusion and enhance the flexibility of the gold particles during epitaxial growth. This growth initiates at the contact interface and subsequently propagates throughout the entire FCC nanoparticle, leading to its transformation into the 4H phase. He et al. [89]. activated the reversible wurtzite–BCT reconstruction of the outermost layer on the ZnO $(10\bar{1}0)$ surface using electron beam irradiation. By combining aberration-corrected transmission electron microscopy with DFT calculations, they directly visualized the reconstruction process at atomic resolution, uncovering a previously unknown intrinsic bistability of the ZnO $(10\bar{1}0)$ surface.

Typically, these strong external forces drive atomic movement on the surface of metastable phase materials, leading to the formation of defects and dislocations. Although these methods all leverage on kinetic barriers, confinement effects, or external stimuli to prevent phase transitions, the purity and crystallinity of the final products can vary significantly. In order to gain a deeper understanding of the specific synthesis conditions, by classifying and distinguishing the spatial structures of metastable phases from their stable counterparts, the synthesis methods of representative metastable phase materials are summarized in Table 1. The selection was based on the following criteria: (i) materials with high Gibbs free energy relative to their corresponding thermodynamically stable phases that are broadly recognized and significant in the field, (ii) cases where the synthesis approaches and the corresponding crystal/electronic structures are clearly documented and (iii) materials with practical potential in terms of cost and abundance.

Representative synthesis process

Here, we present more specific examples of promising materials and elucidate the atomic-scale mechanisms underlying the formation of metastable phase materials. One notable example is metallic 1T MoS_2 [102] which has attracted considerable attention due to its excellent conductivity [103], sulfur-rich properties, unique anisotropy, and permeable channels for ion transport and adsorption. Tour et al. have

Table 1
A brief overview of the synthesis methods for representative metastable phase materials.

Metastable phase materials	Space structures	Synthesis strategies	Specific conditions	References
1T-MoS_2	Trigonal	Wet chemistry	/	[90]
Zr_3O	Hexagonal	Wet chemistry	Nitrogen-doped carbon templates	[16]
CdS	Cubic (FCC)	Wet chemistry	PbS templates	[91]
CeO_2	Tetragonal	Wet chemistry	/	[24]
3R-MoS_2	Rhombohedral	Chemical vapor deposition	SiO_2/Si substrate	[92]
HfO_2	Hexagonal	Mechanochemistry	Molten KOH	[93]
$CsPbI_3$	Cubic	Mechanochemistry	/	[94]
β-Li_3N	Hexagonal	Mechanochemistry	9 MPa hydrogen pressure	[95]
$HoMnO_3$	Orthorhombic	High-pressure	5 Gpa	[96]
$TbPO_4$	Tetragonal	High-pressure	15.5 GPa	[97]
$TbPO_4$	Monoclinic	High-pressure	9.6 GPa	[97]
ZrO_2	Orthorhombic	High-pressure	4 GPa	[98]
BN	Cubic (FCC)	High-temperature and high-pressure	/	[99]
$ZnTiO_3$	Hexagonal	High-temperature and high-pressure	1000 °C for 30 min under a pressure of 7.5 GPa	[100]
α-Ga_2O_3	Rhombohedral	Plasma-assisted atomic layer deposition	On-axis, *c*-plane sapphire substrates	[101]
ε-Ga_2O_3	Orthorhombic	Plasma-assisted atomic layer deposition	On-axis, *c*-plane sapphire substrates	[101]
κ-Ga_2O_3	Orthorhombic	Plasma-assisted atomic layer deposition	On-axis, *c*-plane sapphire substrates	[101]
ZrO_2	Tetragonal	Heavy ion irradiation	1400 K	[98]
ZrO_2	Cubic (FCC)	Heavy ion irradiation	2600 K	[98]

developed a FJH technology that synthesizes metastable phase transition metal chalcogenides [11] and carbides [58] within a few milliseconds. Different degrees of phase transition can be achieved by controlling the reaction duration and additives. According to first-principles DFT calculations, during the phase formation of MoS_2, the energy provided to the system and adjustable substitutional defects. For instance, W can form substitutionaldefects W_{Mo} in MoS_2, create many vacancies that stabilize the 1T phase (Fig. 12a and b). Jiao and colleagues [62,104] designed a potassium (K)-assisted chemical vapour deposition technique guided by theoretical calculations, which directly produces high-purity and crystalline 1T′ MoS_2 with in-plane anisotropy. Zhang et al. [63,64] extended this preparation system to VIB transition metal dichalcogenides using K_2MoO_4 or K_2WO_4 as precursors (Fig. 12c). In wet chemical reactions, metastable phases can serve as intermediates to reform material defects. Taking the synthesis of perovskite materials as an example, a metastable phase forms due to the adhesion of L-arginine (L-Arg) and the phase separation of poly(vinylidene fluoride-co-hexafluoropropylene) (P-polymer), resulting in a uniformly mixed all-inorganic $CsPbI_{3-x}Br_x$ perovskite film through a lower energy barrier (E_1) at a lower annealing temperature. Subsequently, the metastable intermediate phase completely transforms into a stable and planar defect free perovskite film by overcoming a slightly higher energy barrier (E_2), and L-Arg is released from the internal lattice of the metastable phase through a higher-temperature annealing process (Fig. 12d) [61]. Shao et al. developed a general strategy using a microwave-assisted mechanochemical-thermal technique (Fig. 12e) to synthesize a wide range of metastable phase materials, including 3R-IrO_2 [65], 1T IrO_2 [66], monoclinic phase layered IrO_2 nanoribbons [67], hexagonal SnO_2 [68], etc.

A new paradigm for the discovery and synthesis of novel metastable phases was established when Chun et al. [54] synthesized a novel metastable hcp palladium hydride (PdH_x) via a liquid cell transmission electron microscope (Fig. 13). The diffraction patterns obtained from *in situ* TEM (Fig. 13a and b) and *ex situ* high-resolution scanning transmission electron microscopy (Fig. 13c) images of the synthesized nanoparticles corresponded to a hcp lattice, rather than the face-centered cubic (fcc) lattice typical of nearly all reported Pd compounds, irrespective of the growth pathway-whether monomer attachment or coalescence. The ABAB stacking, a typical feature of hcp phases, can be clearly seen in Fig. 13d. Moreover, the detection of a pronounced

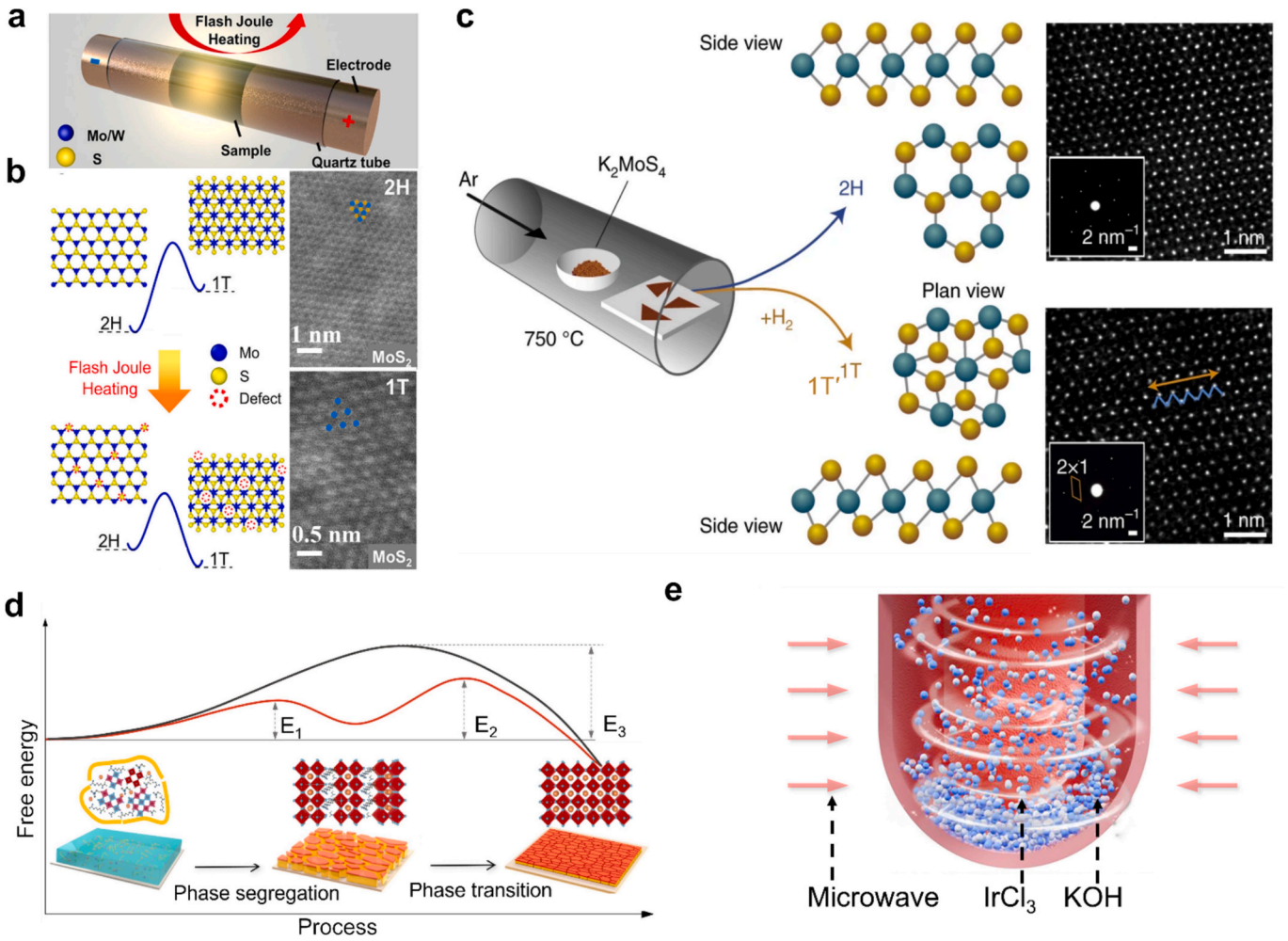

Fig. 12. Common synthesis strategies for metastable phase materials. (a) Schematic diagram of phase conversion through FJH. Reproduced with permission [11]. Copyright 2021, American Chemical Society. (b) Schematic diagram of energy levels before and after the FJH reaction and high-angle angular dark field-scanning transmission electron microscopy (STEM) atomic images of 2H and 1 T phases of MoS_2. Reproduced with permission [11]. Copyright 2021, American Chemical Society. (c) Schematic diagram of 1 T′ and 2H MoS_2 synthesis (Reproduced with permission [104]. Copyright 2018, Springer Nature) and STEM images. Reproduced with permission [62]. Copyright 2018, Springer Nature. (d) The consecutive two-step low-energy barrier (E_1 and E_2) pathway involves the proposed metastable intermediate phase crystallization process during mixed halide $CsPbI_{3-x}Br_x$ crystallization. The crystal structure models reflect the corresponding interactions among L-Arg, poly(vinylidene fluoride-co-hexafluoropropylene) (P-polymer), and perovskite units in the metastable phase crystallization process. Reproduced with permission [61]. Copyright 2022, the American Association for the Advancement of Science. (e) Schematic diagram of the synthesis of 3R-IrO_2 employing microwave-assisted mechano-thermal technique. Reproduced under terms of the CC-BY license [65]. Copyright 2021, Elsevier.

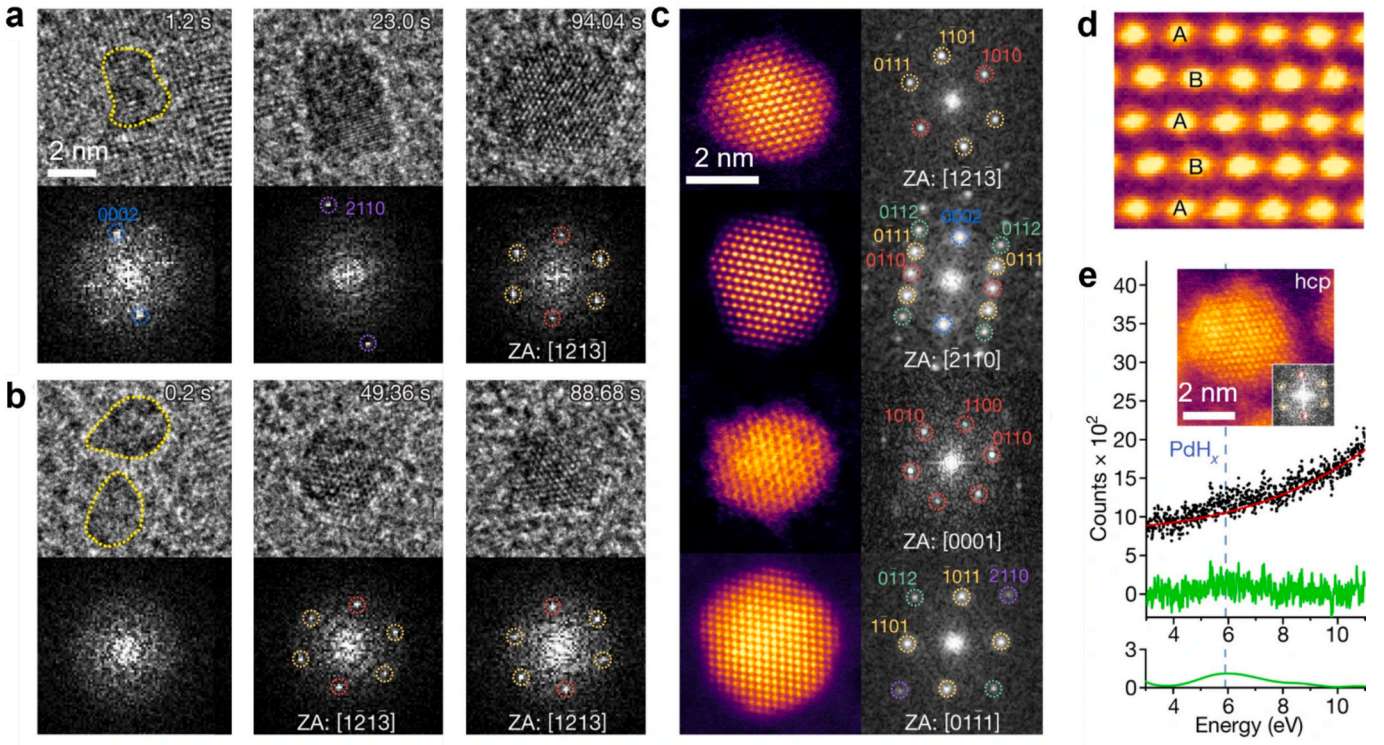

Fig. 13. Visual synthesis strategies for metastable phase materials. (a) Visualization of Pd nanoparticles through monomer attachment growth and corresponding fast Fourier transform. Reproduced with permission [54]. Copyright 2022, Springer Nature. (b) Visualization of Pd nanoparticles through coalescence growth and corresponding fast Fourier transform. Reproduced with permission [54]. Copyright 2022, Springer Nature. (c) Ex-situ high-resolution scanning transmission electron microscopy images and fast Fourier transforms of four different particles formed at an electron dose rate of 675 e^{-} $Å^{-2}$ s^{-1} in a graphene liquid cell, which is consistent with the $[1\bar{2}1\bar{3}]$, $[\bar{2}110]$, [0001] and $[01\bar{1}1]$ zone axis patterns of the hcp lattice. The dashed circles represent low-index planes colored according to each plane family. Reproduced with permission [54]. Copyright 2022, Springer Nature. (d) ABAB stacking of Pd atoms along the $[\bar{2}110]$ zone axis in (c). Reproduced with permission [54]. Copyright 2022, Springer Nature. (e) Raw and denoised electron energy loss spectra obtained from hcp nanoparticles arranged along the $[1\bar{2}1\bar{3}]$ axis. Reproduced with permission [54]. Copyright 2022, Springer Nature.

electron energy loss spectroscopy peak at approximately 5.9 eV, a well-established spectral signature of hcp PdH_x, in conjunction with the exclusive observation of a Pd signal in the energy dispersive X-ray spectroscopy spectrum, provides compelling evidence for the formation of PdH_x (Fig. 13e).

To further highlight the significance of pressure in the synthesis of metastable phase materials, we emphasize the advantages of extreme pressure fabrication [105–109]. Pressure can convert periodically ordered $CsPbBr_3$ perovskite nanocube superlattices into transverse 2D nanoplates with uniform thickness, good crystallinity and enhanced optical properties (Fig. 14a) [69]. Cao et al. [110] proposed the rational design of synthesis methods for metastable phase materials using low-pressure pathways. Exemplifying the environmental metastability of the rock salt phase in CdSe, CdS, or their nanocrystals, it has been elucidated that inter-particle sintering acts as the dominant process for the elimination of crystal defects and the relaxation of lattice distortions within high-pressure rock salt structures. This mechanism not only facilitates the controlled stabilization of metastable rock salt phases under ambient pressure conditions but also enables the precise engineering of their structural properties, thereby advancing the synthesis of metastable phases with tailored characteristics. The interconnected nanocrystalline network produced through this method effectively stabilizes high-energy metastable phases under environmental conditions (Fig. 14b). Fig. 14c illustrates the phase transition process of $NbOI_2$ under pressure.

At ambient pressure, $NbOI_2$ exhibits 2-fold rotational symmetry along the *b*-axis. As pressure increases, the eccentric displacement of Nb atoms along the *b*-direction is suppressed, eventually causing the Nb atoms to align within the plane formed by I atoms. This leads to additional mirror symmetry perpendicular to the *b*-axis, resulting in a structural phase transition of $NbOI_2$ from the C2 space group to C2/m space group under pressure [111]. While most studies report pressures below 100 GPa, at extreme pressures, such as close to 700 GPa, the metastability of materials becomes more prevalent. For instance, Fig. 14d shows that FeO transforms to the B2 structure at approximately 300 GPa, while in MgO, this phase transition occurs above 600 GPa (high temperature). The difference in the occurrence of the B1-B2 transition may affect the hybrid behavior of the MgO-FeO system.

Stabilization strategies for metastable phase materials

Stabilization mechanism

Thermal instability is a hallmark of metastable phases, wherein reducing the Gibbs free energy of formation is a fundamental requisite for the realization of high-purity metastable phases materials [113–116]. Here, we discuss the phase transition mechanisms at the atomic scale from the perspectives of atomic migration (diffusion and shear) and atomic pinning (Fig. 15). Atomic diffusion involves the migration of atoms or ions across the lattice, facilitating structural rearrangements that drive the system toward a lower-energy configuration. This process is typically thermally activated and can lead to phase transformations by enabling nucleation and growth of the stable phase. In contrast, shear mechanisms involve coordinated atomic displacements along specific crystallographic planes, often triggered by external stress, pressure, or strain. Shear-driven transformations, such as martensitic transitions, occur rapidly and are often diffusionless, preserving the overall composition while altering the atomic arrangement.

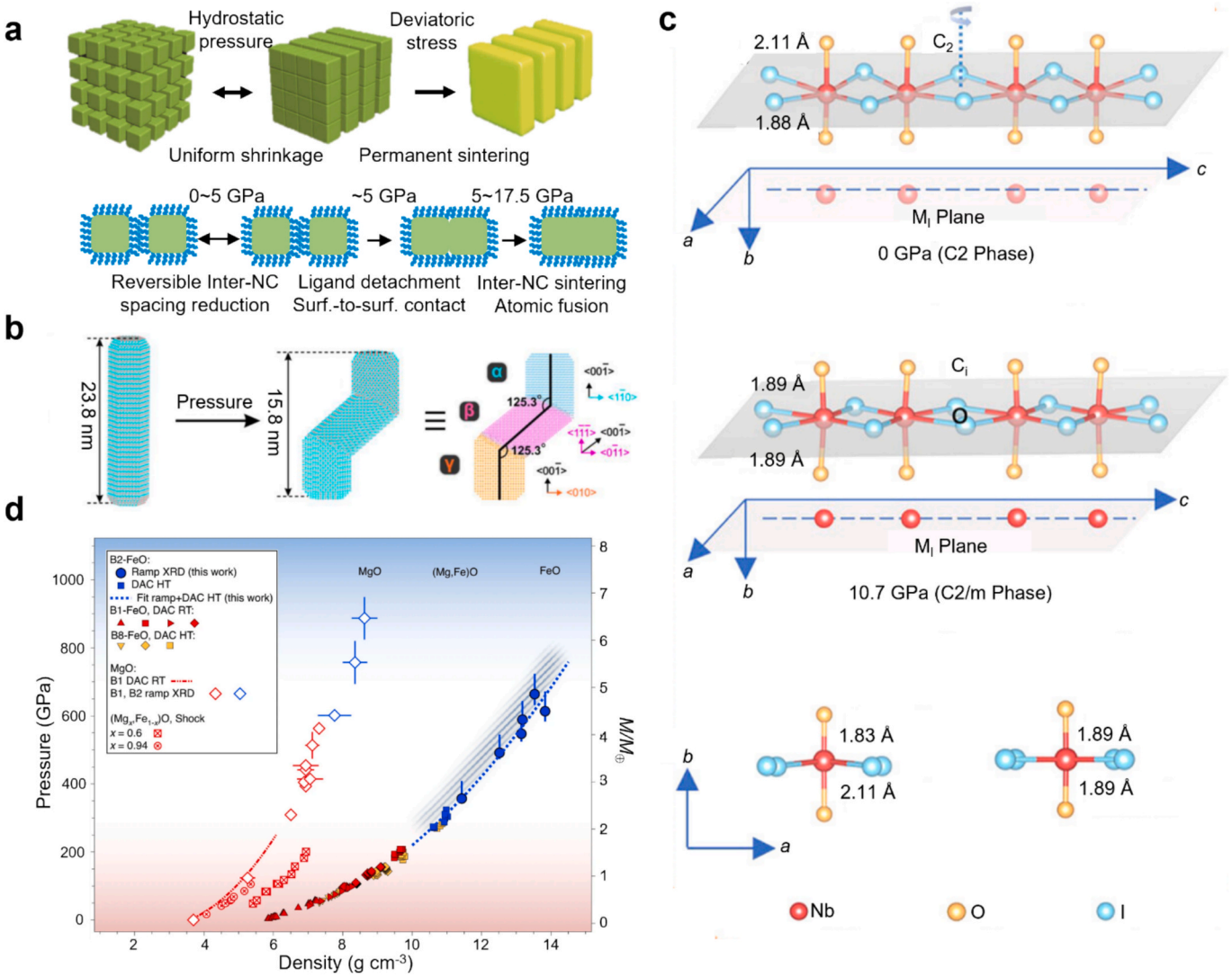

Fig. 14. Pressure-driven phase transitions. (a) Schematic illustration of the pressure sintering process: evolution of nanocube (NC) superlattice and interparticle fusion under pressure. Reproduced with permission [69]. Copyright 2017, Wiley-VCH. (b) Schematic diagram showing the conversion of CdSe/CdS wurtzite nanorods into double-bent three-domain CdSe/CdS rock salt nanorods. Reproduced with permission [61,110]. Copyright 2022, the American Association for the Advancement of Science. (c) Pressure driven transformation of $NbOI_2$ crystal structure from the C2 phase to the C2/m phase. Reproduced with permission [111]. Copyright 2024, American Chemical Society. (d) Pressure-density relationships of oxides. Reproduced with permission [112]. Copyright 2021, Springer Nature.

Atomic pinning primarily restricts atomic movement and increases the formation energy required for stable phases. Current strategies to achieve atomic pinning include doping/vacancies, solid solution formation/alloying, template-induced stress, confinement, and other nanoscale design strategies.

Representative stabilization process

Yu et al. proposed the use of a spatially confined template method to synthesize high phase purity 1T-MoS_2, which allows for modulation of the confined space and template structure to improve the purity of 1T-MoS_2 (Fig. 16a) [117]. In another study, Yu et al. [12] reported that cubic $CoSe_2$ generated many Se vacancies during the heating process, and the introduction of phosphorus atoms with different electronegativities filled these Se vacancies, resulting in the rotation of the original double Se bonds, thus promoting the phase transition of $CoSe_2$ from a stable cubic phase to a metastable orthorhombic phase (Fig. 16b). Another typical case is the phase transition of In_2Se_3. β′-In_2Se_3 was initially stretched and fixed by the substrate, causing layering to occur between β′-In_2Se_3 and the substrate during *in-situ* transmission electron microscopy (TEM) operation. The tensile strain initially exerted on β′-In_2Se_3 by the substrate was released and recovered, leading to a transition from β′-In_2Se_3 to α-In_2Se_3 [118]. Through DFT calculations, it was found that the energy levels of β′-In_2Se_3 and α-In_2Se_3 were very close, with the ground state of α-In_2Se_3 slightly lower than that of β′-In_2Se_3 (Fig. 16c) [118]. *In-situ* selected-area electron diffraction (SAED) and non-destructive X-ray photoelectron spectroscopy measurements revealed that Se-vacancies play a key role in inducing the phase transition and stabilizing β′-In_2Se_3 [119].

Additionally, *in-situ* Raman spectroscopy on a flexible polyethylene terephthalate substrate confirmed the strain induced phase transition mechanism from β′-In_2Se_3 to α-In_2Se_3 [119]. Our team has developed a doping strategy [13] and a substrate covalent bonding strategy [56] (Fig. 16d) to inhibit the phase transition from β-Fe_2O_3 to α-Fe_2O_3. Experiments have shown that high power Raman lasers can induce metastable phase transitions, and the precise Raman vibration peak of β-Fe_2O_3 has been calculated and experimentally verified (Fig. 16e), thus eliminating the controversies in previous literature. This finding highlights the inherent risk that modern microscopic analysis techniques may inadvertently induce metastable phase transitions, thereby

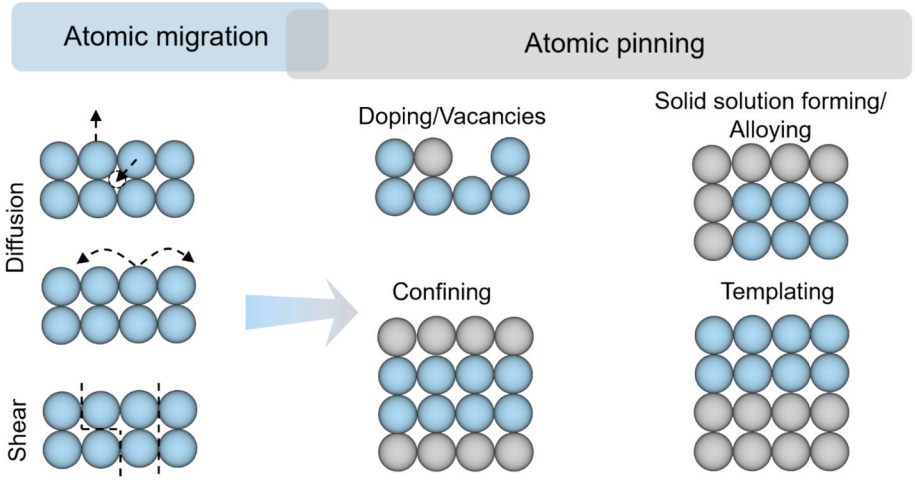

Fig. 15. Atomic mechanisms governing metastable phase transitions and stabilization. The left panel illustrates atomic migration processes, including diffusion (top) and shear (bottom), which facilitate phase transformations by enabling structural rearrangements. The right panel illustrates atomic pinning strategies, such as doping, vacancies, alloying, confining and templating which hinder atomic mobility, thereby stabilising metastable structures and increasing their resistance to transformation into equilibrium phases.

compromising the integrity of experimental data and potentially leading to misinterpretations or erroneous conclusions. As such, a rigorous and systematic evaluation of structural phase transitions in metastable phase materials is imperative. So, a continued advancement of this field will necessitate not only the refinement of stabilization strategies but also the development of more precise and minimally invasive analytical methodologies to ensure the reliability and accuracy of experimental findings.

Thermodynamic-kinetic adaptability in applications

Metastable phase materials excel in catalyzing reactions at active sites, where their metastable nature enables dynamic coupling with transient molecular intermediates. This adaptive interplay, influenced by external factors, modulates the reaction energy landscape, reducing energy barriers and optimizing reaction pathways. In this section, we provide a comprehensive analysis of their potential across various energy forms, including electrical, photonic, and thermal modalities. Table 2 summarizes and compares representative metastable phase materials and their application advantages.

Metastable phase electrocatalysis

An electrocatalytic reaction occurs on electrode surfaces, driven by an applied potential and facilitated by an electrocatalyst. It involves electron transfer between the electrode and the reactant, allowing specific reactions to proceed with lower energy consumption. The electrocatalyst plays a crucial role in lowering the reaction energy barrier and enhancing the reaction rate [134–137]. Common electrocatalytic materials include platinum (Pt), palladium (Pd), metal oxides, and carbon-based compounds [138,139]. Metastable phase materials have emerged as promising candidates in electrocatalysis due to their distinct catalytic behaviors, particularly in reactions such as oxygen evolution and hydrogen evolution in challenging environments like low-quality seawater or sewage, where controlling the number of active sites and their adsorption characteristics is key to enhancing performance [140]. Here, we summarize the potential advantages of metastable phase materials from the perspectives of the charge transfer effect, the Sabatier principle, and d-band center theory, which are of significant interest to researchers.

Metastable phase materials tend to exhibit symmetry breaking compared to stable phase materials, and their high Gibbs free energy can lead to changes in grain size, which enhances charge transfer effect (Fig. 17a). Additionally, modified crystallographic constants often increase the reaction rate or reduce overpotential, positioning most metastable phase materials within the optimal region of the Sabatier principle (Fig. 17b). When an adsorbed molecule approaches a catalyst surface, its orbitals interact with the metal's *s* and *d* orbitals. This interaction can cause energy level splitting, generating antibonding orbitals. If the antibonding state lies above the Fermi level, it favors adsorption because the high-energy orbital remains unoccupied. Conversely, if the antibonding state is lower than the Fermi level, adsorption is less favorable due to electron filling in the high-energy orbital. The d-band center of the metastable phase is positioned lower than that of the stable phase relative to the Fermi level, weakening the adsorption strength of intermediates on the active site, thereby optimizing electrocatalytic performance (Fig. 17c) [141–143].

For instance, 1T-IrO_2 with a space group of *P*-3m1 (164), as opposed to the rutile-IrO_2 with space group 136 (*P*42/*mnm*), manifests the lowest overpotential compared with the reference catalyst for the acidic oxygen evolution reaction (Fig. 18a). At the atomic level, Ir atoms are either buried or exposed by oxygen atoms on 1T-IrO_2 and rutile-IrO_2, respectively, which leads to strong adsorption of hydroxyl groups and arduous desorption of products on the rutile-IrO_2 surface. This calculations reveal that the formation of *OH on the active sites of rutile IrO_2 (110) surfaces is thermodynamically favorable, being either exothermic or only mildly endothermic. In sharp contrast, the same step is considerably more endothermic on 1T-IrO_2. This pronounced difference suggests that 1T-IrO_2 hosts a fundamentally different active site environment, which underpins its superior catalytic performance (Fig. 18b and c) [66]. The 3R-IrO_2 with a space group of *R*-3 *m* (166) achieves an ultralow overpotential of 188 mV at a current density of 10 mA cm_{geo}^{-2} (Fig. 18d). DFT calculations show that the thermodynamic OER overpotentials of 3R-IrO_2 and rutile-IrO_2 are 0.55 and 0.68 V, respectively, indicating that 3R-IrO_2 displays higher OER activity. Compared to rutile-IrO_2, the edge Ir–O bonds of 3R-IrO_2 show a greater bond orbital distribution, which confirms a weak adsorption mode at the coordinatively unsaturated Ir site exposed on the edge of 3R-IrO_2 (Fig. 18e) [65]. In comparison to rutile-IrO_2, Ir in the monoclinic phase layered IrO_2 nanoribbons (IrO_2NR) with a space group *C*2/*m* has a lower d-band center and free energy barrier (Fig. 18f and g) [67].

Ye et al. designed a metastable phase, β-$NiMoO_4$, with phosphate substitution that exhibited optimal hydrogen adsorption free energy and an ultralow overpotential in 1 M KOH for the hydrogen evolution reaction (Fig. 18h) [10]. According to the Bader charge calculations, the charge transfer of the O atom connected to the Mo and Ni atoms in P-

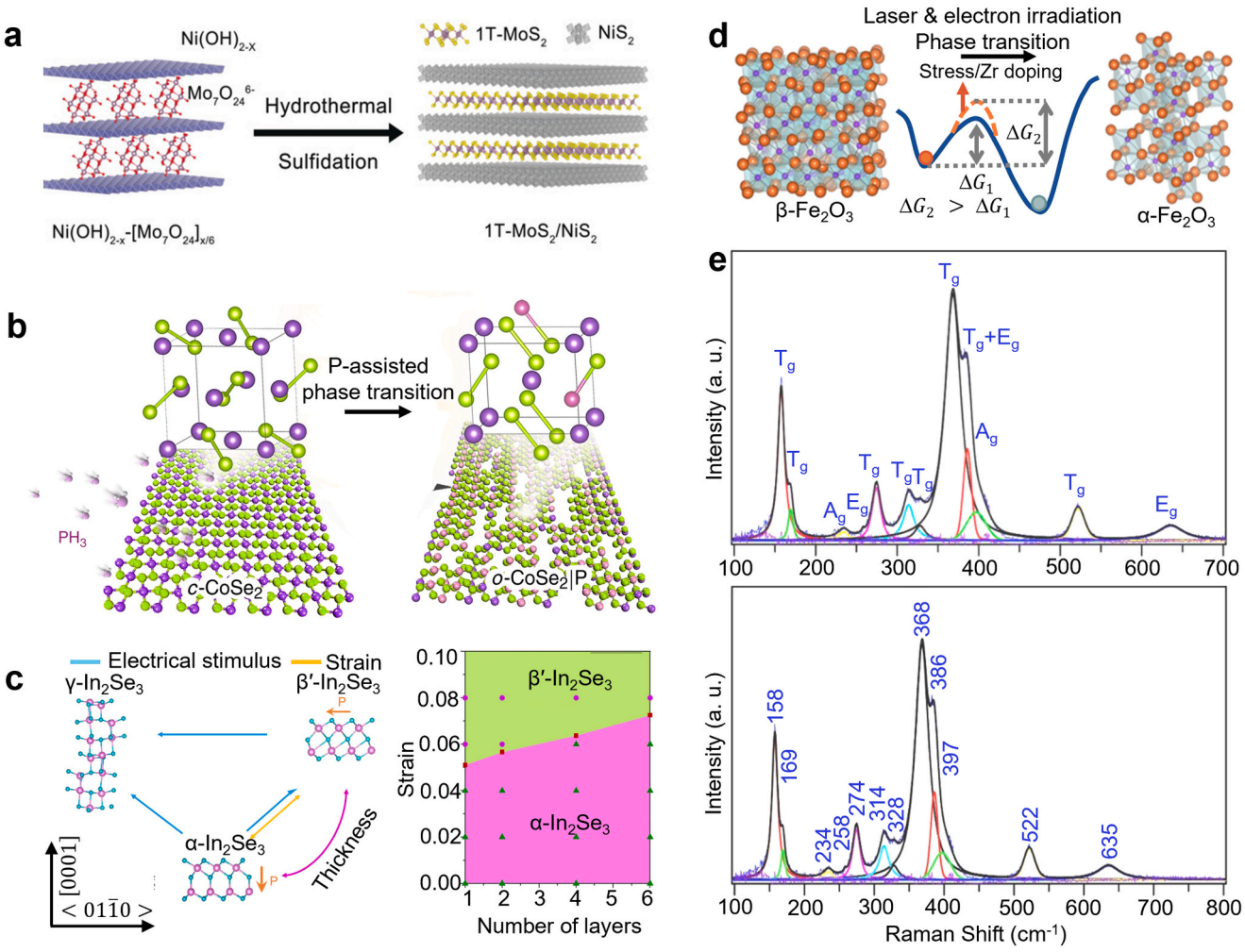

Fig. 16. Stabilization strategies for metastable phase materials. (a) Schematic diagram of 1 T-MoS_2 synthesis within NiS_2 interlayers by spatially confined templates. Reproduced with permission [117]. Copyright 2019, Wiley-VCH. (b) Schematic illustration of cubic $CoSe_2$ (c-$CoSe_2$) and orthorhombic marcasite o-$CoSe_2$ via phosphor-assisted phase transition. Reproduced with permission [12]. Copyright 2018, Springer Nature. (c) Schematic diagram of atomic structures during phase transition process and phase diagrams of β′-In_2Se_3 and α-In_2Se_3 obtained through DFT calculations. Reproduced with permission [118]. Copyright 2022, the American Association for the Advancement of Science. (d) Schematic diagram of the stabilization of β-Fe_2O_3 through covalent bonding of the substrate (Reproduced under terms of the CC-BY license [56]. Copyright 2021, Elsevier) and Zr doping. Reproduced with permission [13]. Copyright 2020, Oxford University Press. (e) Vibration modes and Raman spectroscopy of β-Fe_2O_3 under non-phase transition conditions. Reproduced with permission [13]. Copyright 2020, Oxford University Press.

Table 2
A brief overview of the advantages of representative metastable phase materials.

Metastable phase materials	Space structures	Catalytic forms	Advantages	References
1T-WS_2	Trigonal	Electrocatalysis	/	[120]
$CoCu_2O_4$	Orthorhombic	Thermal catalysis	Lewis-acidic surface sites	[121]
1T-MoS_2	Trigonal	Electrocatalysis	High electron transfer	[122]
α-MoC_{1-x}	Cubic (FCC)	Electrocatalysis	Large surface area	[123]
IrO_2	Monoclinic	Electrocatalysis	Low d-band center	[67]
IrO_2	Orthorhombic	Electrocatalysis	Optimal adsorption energy	[124]
β-Ag_2WO_4	Hexagonal	Photocatalysis	Narrow band gap	[125]
$K_2LaTa_2O_6N$	Tetragonal	Photocatalysis	Long carrier lifetime	[126]
CdS	Cubic (FCC)	Photocatalysis	Optimal adsorption energy	[91]
TiO_2	Orthorhombic	Photocatalysis	Optimal adsorption energy	[127]
TiO_2	Orthorhombic	Photocatalysis	Optimal adsorption energy	[128]
Fe_2O_3	Orthorhombic	Photocatalysis	/	[129]
Fe_2O_3	Cubic (BCC)	Photoelectrocatalysis	Narrow band gap	[130]
Fe_2O_3	Cubic (BCC)	Photoelectrocatalysis	Narrow band gap	[131]
Fe_2O_3	Cubic (BCC)	Photoelectrocatalysis	/	[132]
$CoCu_2O_4$	Orthorhombic	Thermal catalysis	Lewis-acidic surface sites	[121]
ZrO_2	Cubic (FCC)	Photothermal catalysis	Optimal activation energy	[133]

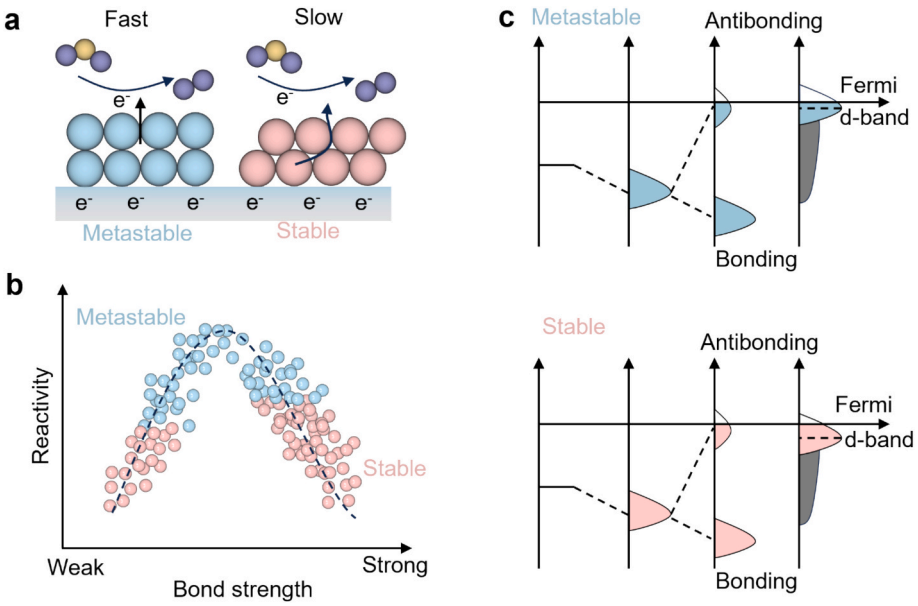

Fig. 17. Thermodynamic-kinetic adaptability of metastable phase electrocatalytic reactions. (a) Variations in interfacial charge transfer effects induced by metastable phases. (b) Enhanced catalytic reactivity of metastable phase materials based on the Sabatier principle. (c) Schematic diagram of the d-band center position relative to the Fermi level, highlighting its influence on adsorption strength. The primary distinction between the schematic diagrams is the relative position of their d-band centers: the metastable phase exhibits a d-band center closer to the Fermi level compared to the stable phase. Adapted with permission [144]. Copyright 2011, National Academy of Sciences.

β-$NiMoO_4$ was greater than that in α-$NiMoO_4$ (Fig. 18i). Other examples of metastable phase electrocatalysis include the hexagonal phase SnO_2 nanoribbon electrocatalytic synthesis of H_2O_2 [68], semimetal 1H-SnS_2 for electrocatalytic CO_2 reduction reactions [145], etc. By enhancing the exposure of active site and optimizing adsorption characteristics, the metastable phase materials can significantly accelerate reactions and improve efficiency across various electrocatalytic processes. Wang et al. [80] showed that HCP-Ni@NC (NC stands for nitrogen-coated carbon) benefits from nickel-induced electronic modulation of the N-coated carbon shell, achieving a current density of 10 mA cm^{-2} at an overpotential of just 305 mV, which is 55 mV lower than that of FCC-Ni@NC. The metastable Pd nanoparticles synthesized by Liu et al. are well-dispersed and uniformly anchored on a carbon substrate. Their abundant twinning structures endow the catalyst with superior electrocatalytic performance for the ethanol oxidation reaction and enhanced resistance to CO poisoning compared with commercial Pt/C [72]. Xing et al. [146] reported a monoclinic WP_2 electrocatalyst that enables acidic hydrogen evolution with an onset overpotential of 54 mV, a Tafel slope of 57 mV dec^{-1}, an exchange current density of 0.017 mA cm^{-2}, and a Faradaic efficiency approaching 100 %, while maintaining high activity and durability across neutral and alkaline conditions. These examples highlight the unique electronic structure of the metastable phase materials and its adaptable adsorption–desorption behavior toward reactive molecules.

Metastable phase photo/photoelectrocatalysis

Metastable phase materials offer exciting possibilities in photocatalysis and photoelectrocatalysis due to their unique electronic structures and bandgap tunability. By leveraging metastable phases, researchers have been able to enhance charge separation and improve the overall efficiency of light-driven reactions. In this section, we explore various innovations in phase junctions, vertical heterostructures, and metastable intermediate structures (MIS) that have contributed to advances in photocatalytic performance.

We analyze the adaptability of metastable phase materials from the perspective of photoexcited carrier generation and dynamic behavior. In direct bandgap semiconductors, photon absorption enables electrons to transit directly from the valence band maximum to the conduction band minimum, generating free electrons and holes without requiring additional lattice vibrations for momentum matching (Fig. 19a). This place stringent demands on the dielectric characteristics of semiconductors, where metastable phase materials present valuable opportunities. Taking typical oxides as an example, the conduction band in semiconductors arises from the hybridization of metal 3d orbitals and oxygen 2p orbitals, while the valence band is primarily composed of oxygen 2p orbitals. The diverse unit cell configurations of metastable phase materials contribute to the development of highly light-absorbing semiconductors with reduced bandgap (Fig. 19b). Carrier dynamics studies reveal significant variations in bulk carrier lifetimes among metal oxides, differing by several orders of magnitude, for instance, the bulk carrier lifetime of TiO_2 is approximately 1,000 times longer than that of α-Fe_2O_3. This discrepancy can be attributed to factors such as doping density and electronic structure. In practical reactions, a space charge layer forms at the metal oxide-electrolyte interface, extending the minority carrier lifetime (Fig. 19c). These long-lived carriers further enhance the material's performance in optoelectronic and catalytic applications [147].

Our research group has identified the metastable phase β-Fe_2O_3 with a direct band gap of approximately 1.9 eV, as a highly promising photocatalyst. According to the band structure of bulk β-Fe_2O_3, the conduction band is dominated by the Fe 3d orbital, while the valence band is dominated by the O 2p orbital. The conduction band minimum and valence band maximum occur at the same position in *k*-space, which confirms that it is a direct bandgap semiconductor. It does not require the participation of phonons in the process of absorbing photons, making it easier for electrons to be excited [56,131,148]. Therefore, β-Fe_2O_3 has higher light absorption and offers a higher theoretical solar to hydrogen energy conversion efficiency than the indirect bandgap of α-Fe_2O_3 [131]. To address the significant issue of photogenerated carrier recombination in β-Fe_2O_3, Zr doping offers a strategy for killing two birds with one stone which not only increases the carrier concentration, but also improves thermal stability. This strategy led to a five-fold increase in photocurrent density measured under 1 sun (100 mW cm^{-2})

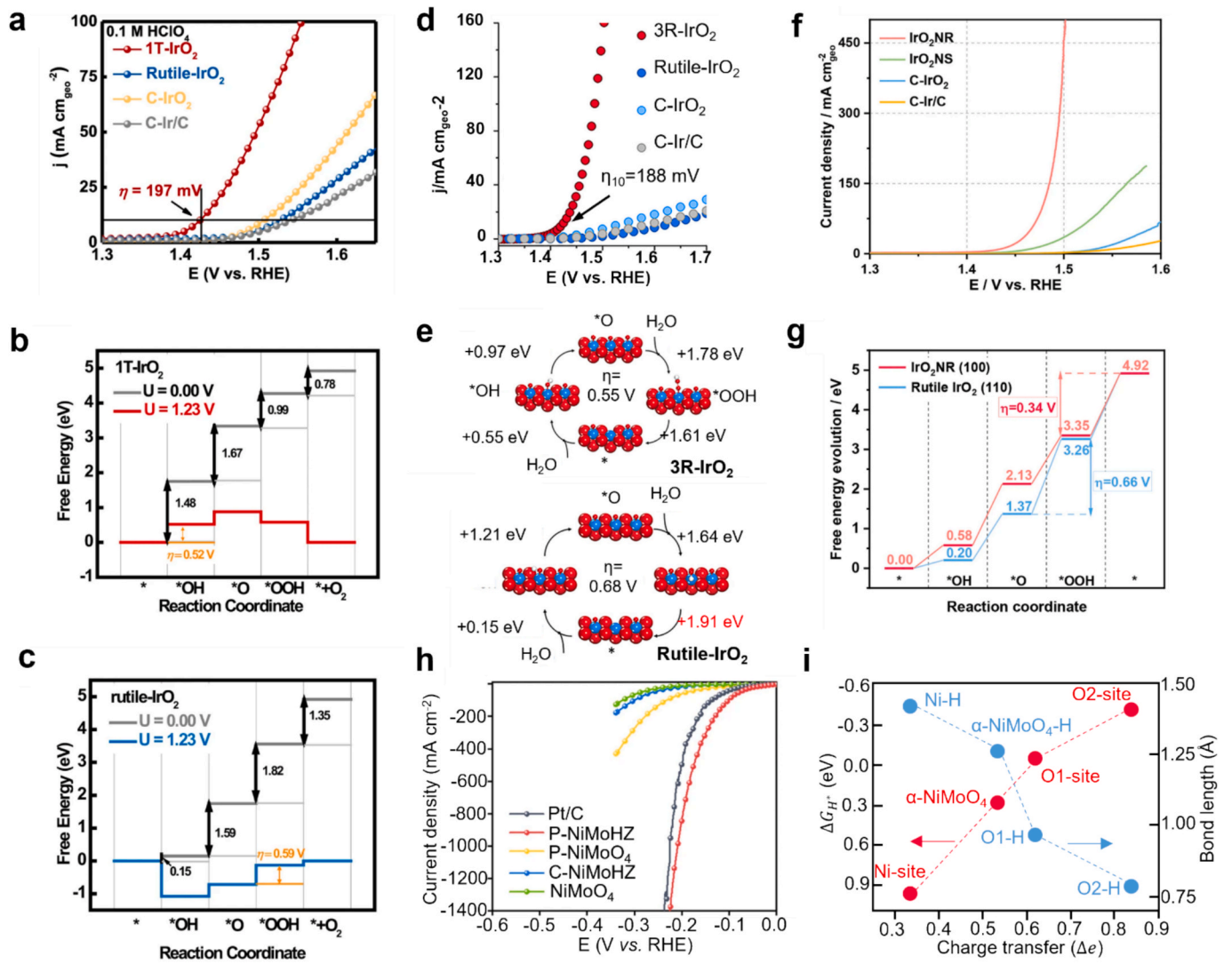

Fig. 18. Thermodynamics-kinetic adaptability of metastable phase electrocatalysis. (a) Polarization curves of 1T-IrO_2, rutile-IrO_2, and commercial catalysts (C-IrO_2 and C-Ir/C). Reproduced with permission [66]. Copyright 2021, Springer Nature. (b) Free energy curves of the OER on 1T-IrO_2. Reproduced with permission [66]. Copyright 2021, Springer Nature. (c) Free energy curves of OER on the Rutile-IrO_2 (110) surface. Reproduced with permission [66]. Copyright 2021, Springer Nature. (d) Polarization curves of 3R-IrO_2, rutile-IrO_2, C-IrO_2, and C-Ir/C. Reproduced under terms of the CC-BY license [65]. Copyright 2021, Elsevier. (e) Free energy curves of the OER on 3R-IrO_2 and rutile-IrO_2. Reproduced under terms of the CC-BY license [65]. Copyright 2021, Elsevier. (f) Polarization curves of nanoribbons (IrO_2NR), IrO_2 nanosheets (IrO_2NS), C-IrO_2 and C-Ir/C. Reproduced with permission [67]. Copyright 2023, Springer Nature. (g) Free energy curves of OER on IrO_2NR (100) and rutile-IrO_2 (110). Reproduced with permission [67]. Copyright 2023, Springer Nature. (h) Polarization curves of $NiMoO_4$, C-NiMoHZ (without phosphate feeding), P-$NiMoO_4$ (derived from the $NiMoO_4{\cdot}xH_2O$ precursor by phosphating), phosphate substituted β-$NiMoO_4$ (P-NiMoHZ), and Pt/C. Reproduced with permission [10]. Copyright 2021, Springer Nature. (i) Linear relationship between ΔG_{H^*}, P-β-$NiMoO_4$-H bond length, α-$NiMoO_4$-H bond length and the amount of charge transfer Δ e. Reproduced with permission [10]. Copyright 2021, Springer Nature.

[13]. Furthermore, engineering a phase transition from the γ-Fe_2O_3 phase to the β-Fe_2O_3 phase was used to increase the crystallinity and reduce the defect concentration to overcome the problem of a high onset potential caused by high defect concentration. Eventually, this led to a β-Fe_2O_3 photoelectrode with an onset potential of only 0.8 V *vs.* reversible hydrogen electrode, which is the lowest value reported so far for a β-Fe_2O_3 photoanode (Fig. 20a) [149]. We further enhanced the M–O bond energy of β-Fe_2O_3 by substituting Fe atoms with Sn atoms. The resulting Sn/β-Fe_2O_3 photoanode can resist severe Cl^- corrosion during the photoelectrochemical splitting of seawater (Fig. 20b) [150]. This approach provides new opportunities for long-term and stable seawater utilization technology.

Additionally, the Fe metal center in β-Fe_2O_3 also serves as an active site for the conversion of H_2O_2 into usable free radicals under light, which can be regarded as an environmentally friendly Fenton reagent for degrading various organic pollutants (Fig. 20c) [151]. We extended this application to binary metal metastable phase materials such as hexagonal $YFeO_3$ [153]. Our research group reported that the local coordination structure and electron density of $YFeO_3$ can be improved by adjusting the surface relaxation through Ti modification, which reduces the photoactivation barrier of H_2O_2 and enhances the production efficiency of hydroxyl radicals (Fig. 20d) [152].

Chu et al. utilized a vertical heterostructure composed of ε-Fe_2O_3 and $BiFeO_3$ to enahnce the efficiency of photoexcited carrier separation, thereby improving its photoelectrochemical properties (Fig. 21a) [154]. Li et al. proposed the concept of phase junctions and validated it across multiple research systems [14,155–159]. They reported that a tunable α-β phase junction in Ga_2O_3 semiconductors can stoichiometrically split water into H_2 and O_2 (Fig. 21b), improving charge separation and transfer [14]. Chen et al. designed a black phosphorus/red phosphorus photocatalyst with a direct Z-scheme heterophase junction. Benefiting from the appropriate band structure, staggered arrangement, and

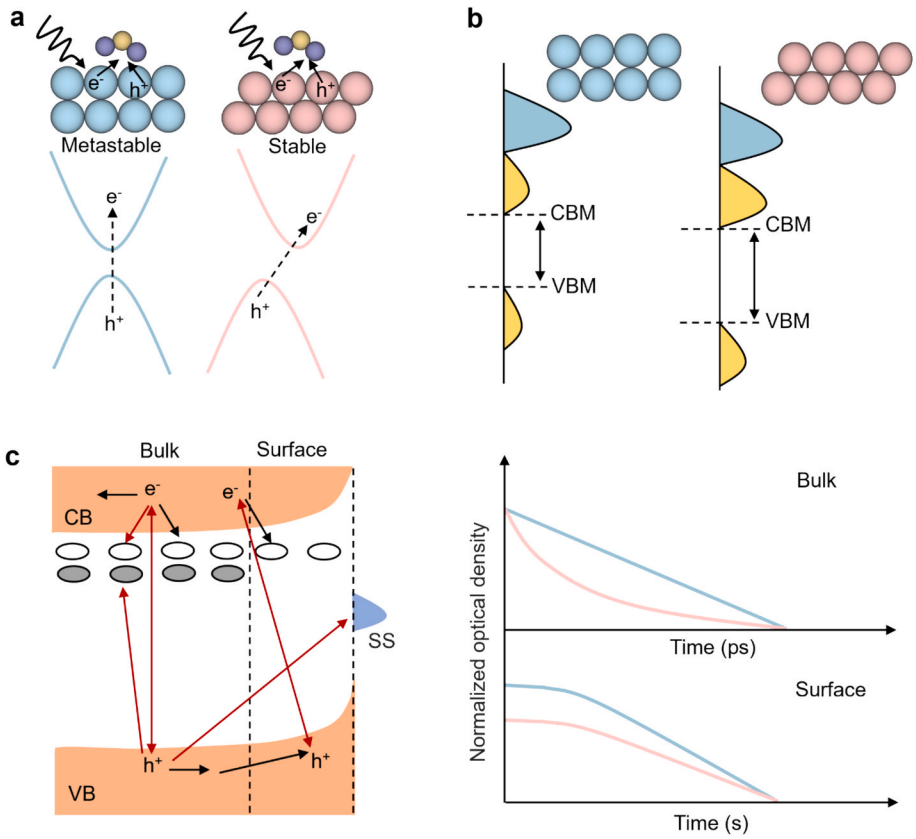

Fig. 19. Thermodynamic-kinetic adaptability of metastable phase photo/photoelectrocatalytic materials. (a) Direct generation of charge carriers (free electrons and holes) in photoexcited semiconductors. (b) Differences in electronic structure between metastable and stable phases. (c) Simplified band diagram of an n-type semiconductor. White ovals represent ionized defect states capable of capturing electrons, while gray ovals denote non-ionized (filled) states that can capture holes; black arrows represent the movement of charge carriers; red arrows indicate the primary recombination processes occurring in the semiconductor bulk after photoexcited electrons transition from the valence band to the conduction band, including interband recombination, capture via defect states, and subsequent recombination. SS represents surface states. The right panel illustrates the dynamic lifetime of carriers in both the bulk and surface regions (space charge layer). Adapted with permission [147]. Copyright 2021, Springer Nature. (For interpretation of the references to colour in this figure legend, the reader is referred to the web version of this article.)

perfect junction interface, the structure has the ability to efficiently separate photogenerated carriers and achieve photocatalytic water splitting without the use of sacrificial agents (Fig. 21c) [160]. Qiao et al. extended the concept of heterophase junctions to a triphasic complex structure. From the photocatalytic water decomposition results, it is evident that the structure exhibits superior photogenerated carrier separation efficiency (Fig. 21d) [161]. The intricate band alignment inherent to the metastable intermediate structure (MIS) is paramount in driving the efficient spatial dissociation of photogenerated electrons and holes. This finely optimized charge separation mechanism, facilitated by the MIS's unique electronic architecture, not only enhances charge carrier dynamics but also substantially elevates photocatalytic efficiency. Such an enhancement fosters a profound improvement in catalytic performance, positioning the MIS as a pivotal factor in advancing the theoretical and practical realms of photocatalytic and electrocatalytic systems. Taking the classic TiO_2 as a case study, the continuous phase transition path and MIS were determined by accurately calculating the band arrangement between the dual-phases. Using the accurate Heyd–Scuseria–Ernzerhof hybrid function, rigorous first-principles calculations of the supercell interface can obtain the offset between the valence band maximum (VBM) and conduction band minimum (CBM) values of the four structures. Among all phases, MIS has the lowest VBM and the highest CBM (Fig. 21e). Furthermore, compared to isolated anatase and rutile, the MIS interface produces a band gap distribution of 2.7 to 4.2 eV, which enhances light absorption (Fig. 21f) [162]. Ashok et al. [163] synthesized a mesoporous, metastable $CuTe_2$ binary crystalline compound with a cubic structure by precisely controlling crystallization via electrochemical methods combined with soft-template polymer micelle chemistry. The material exhibits an optical band gap of 1.67 eV and demonstrates excellent photoresponse. Guo et al. [164]. successfully synthesized α-Ag_2MoO_4/WO_3 composite materials via epitaxial growth on WO_3 nanosheets at room temperature and ambient pressure. The enhanced photocatalytic performance is primarily attributed to the efficient separation of photogenerated charges from WO_3 to α-Ag_2MoO_4 within the composite. Ge et al. [91] controllably synthesized zinc blende (*zb*) CdS and Au@*zb*-CdS core–shell nanocrystals with tunable termination facets, demonstrating their photocatalytic water-splitting capabilities. Theoretical calculations indicate that the {111} facets of *zb*-CdS exhibit higher intrinsic activity than the {100} facets due to their greater surface efficiency and stronger electronic transitions, which enhance adsorption and facilitate the dissociation of adsorbed water molecules. These findings elucidate the transformative potential of metastable photocatalysis/photoelectrocatalysis, offering novel pathways for the identification and application of direct bandgap semiconductors. Additionally, they catalyze groundbreaking innovations in the design of functional catalysts, particularly in the development of next-generation clean technologies.

Metastable phase thermal/photothermal catalysis

Thermal catalytic techniques, a cornerstone of traditional catalysis, play a crucial role in the development of industries such as petroleum

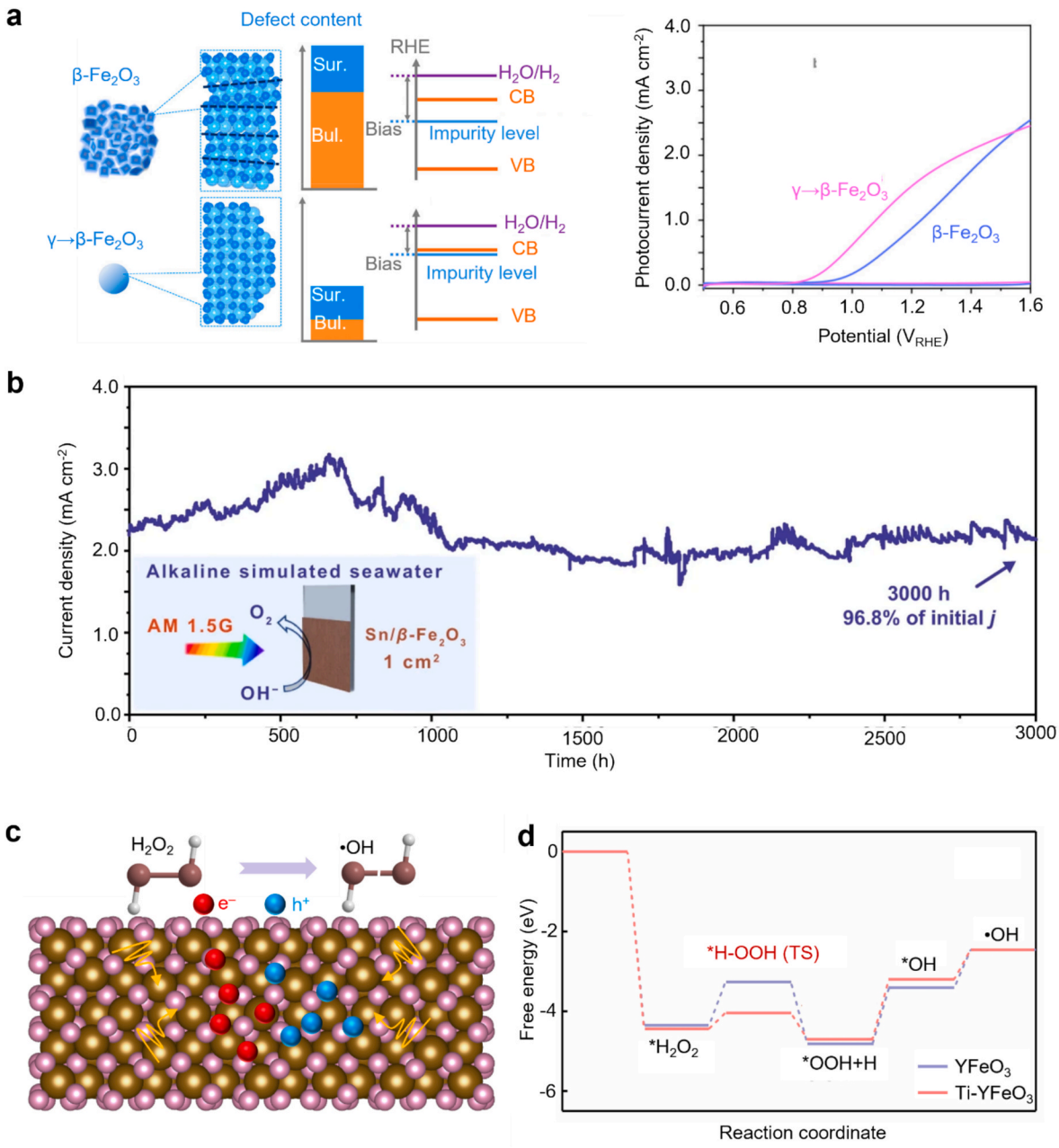

Fig. 20. Thermodynamic-kinetic adaptability of metastable phase materials in photoelectrocatalysis and photocatalysis. (a) Photocurrent density of γ → β-Fe_2O_3 and pure β-Fe_2O_3 samples under irradiation with 10 standard simulated solar radiations, illustrating the effect of the defect content and impurity levels in the γ → β-Fe_2O_3 and pure β-Fe_2O_3 samples. Sur.: Surface. Bul.:Bulk. Reproduced with permission [149]. Copyright 2022, American Chemical Society. (b) 3000-hour photoelectrochemical seawater splitting test for Sn/β-Fe_2O_3 in 1 M KOH/0.5 M NaCl. Reproduced with permission [150]. Copyright 2023, Springer Nature. (c) β-Fe_2O_3 as a catalyst for the photoactivation of H_2O_2. Reproduced under terms of the CC-BY license [151]. Copyright 2019, Elsevier. (d) Free energy curves of photoactivation of H_2O_2 on hexagonal $YFeO_3$ and Ti-$YFeO_3$. Reproduced with permission [152]. Copyright 2022, National Academy of Sciences.

processing, chemical manufacturing, and pharmaceuticals [165–167]. These techniques mainly provide energy to overcome internal energy barriers in catalytic reaction systems through heating, thereby promoting the conversion of reactants into products with high catalytic efficiency [168]. However, the sustainable application of metastable phase materials in thermal catalytic reactions, particularly at high temperatures and in reducing atmospheres, presents significant challenges due to the propensity of these catalysts to undergo structural phase transitions. Nevertheless, this does not hinder the ongoing development of metastable phase materials in this field. In the thermal catalysis process (Fig. 22a), metals typically serve as active sites. The position of the d-band center influences the adsorption energy, which in turn affects the interaction between the reactants and the catalyst surface, ultimately impacting the reaction activity and selectivity. When the d-band center is close to the Fermi level, the catalyst tends to bind reactants more strongly, which can facilitate the activation and subsequent initiation of the reaction. When the d-band center approaches the Fermi level, the catalyst typically exhibits stronger adsorption of reaction intermediates, which can modulate the energy barriers and reaction rates along the pathway. This electronic structural feature enhances catalytic activity, but the adsorption strength must be carefully balanced to avoid over-adsorption that could reduce catalytic performance. So, a well-positioned *d*-band centre allows the catalyst surface to fine-tune the adsorption energy (Fig. 22b), ensuring that reactants are neither

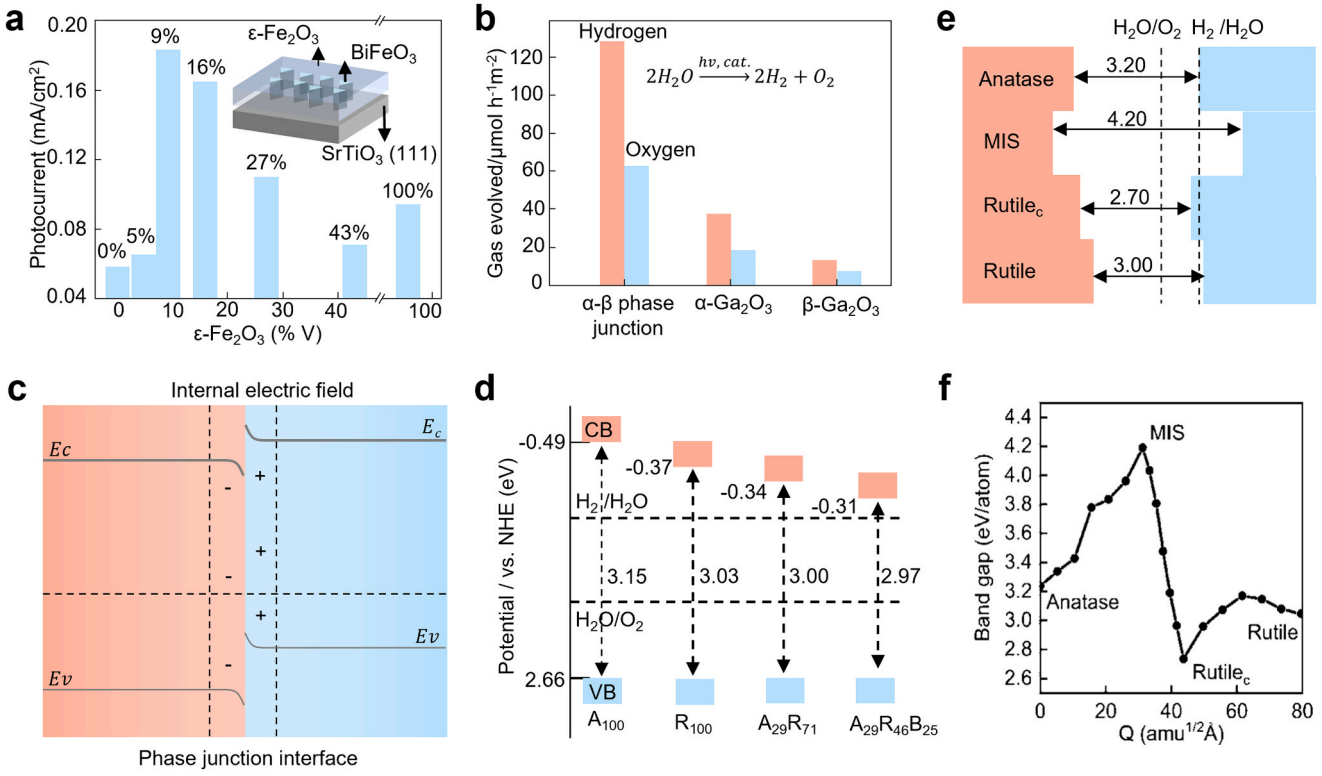

Fig. 21. Thermodynamic-kinetic adaptability of metastable phase materials as reinforcement in photoelectrocatalysis and photocatalysis. (a) Schematic diagram of vertical heterojunction of $BiFeO_3$ embedded in an ε-Fe_2O_3 matrix and the photocurrent density of various $BiFeO_3$-ε-Fe_2O_3 photoelectrodes. Reproduced with permission [154]. Copyright 2016, Wiley-VCH. (b) Enhancing photocatalytic overall water splitting performance by combining α-β phase junctions with Ga_2O_3 [14]. Reproduced with permission [14]. Copyright 2012, Wiley-VCH. (c) Phase junction interface between black phosphorus and red phosphorus. Reproduced with permission [160]. Copyright 2019, Wiley-VCH. (d) Schematic illustration of the band structures for anatase (A), rutile (R) and brookite (B) TiO_2. Reproduced with permission [161]. Copyright 2019, Wiley-VCH. (e) Band arrangement between rutile, MIS, rutile, and anatase. Reproduced with permission [162]. Copyright 2024, National Academy of Sciences. (f) Band gap variation for different transition paths. Reproduced with permission [162]. Copyright 2024, National Academy of Sciences. (For interpretation of the references to colour in this figure legend, the reader is referred to the web version of this article.)

excessively adsorbed (which would hinder desorption) nor insufficiently adsorbed (which would impair effective adsorption). Therefore, the abundance of metastable phase materials offers the necessary d-band characteristics for various reactions, presenting a simple approach for designing new catalysts.

Qiao et al. [30] found that Au/γ-Fe_2O_3 exhibits a higher CO conversion rate compared to Au/α-Fe_2O_3 at low temperatures (Fig. 23a). Through temperature-programmed reduction with CO (CO-TPR), measurements showed that γ-Fe_2O_3 is more readily reduced to Fe_3O_4 than α-Fe_2O_3 after the introduction of Au species (Fig. 23b), thereby catalyzing its reaction with CO. This performance difference is attributed to variations in surface redox properties. Zhang et al. [29] found that Mn on the surface of γ-Fe_2O_3 nanorods exhibited a low oxidation state due to the strong Fe–Mn interaction, which was conducive for the formation of iron carbide active phases, thereby achieving high selectivity for light olefins in Fischer–Tropsch synthesis (Fig. 23c). Tour et al. [58] applied DFT calculations and found that carbon vacancies dominate energy changes in the Mo-C system, serving as a driving factor for the topological transition from β-Mo_2C to α-MoC_{1-x} and then to η-MoC_{1-x} phase (Fig. 23d). Ma et al. employed cubic α-MoC as a support in various reactions such as the water–gas shift reaction (WGS) [170–172], hydrogen production from hydrolysis of ammonia borane [173], hydrogenation reaction of quinoline [174], etc.

They synthesized layered Au clusters on a α-MoC substrate to construct an interfacial catalyst system for the ultra-low-temperature water–gas shift (WGS) reaction. Water was activated on the catalyst surface at 303 K, while CO adsorbed on adjacent Au sites readily reacted with surface hydroxyl groups generated from water dissociation, resulting in high WGS activity at low temperatures (Fig. 23e) [171,172]. Song et al. [175] reported that the activity improvement in the reverse water gas shift (RWGS) reaction was induced by the phase transition of In_2O_3 (Fig. 23f). At temperatures of 450 °C and above, hexagonal phase In_2O_3 (h-In_2O_3) underwent phase transition to cubic phase In_2O_3 (c-In_2O_3). DFT results revealed that the arrangement of surface oxygen on the cubic polymorph was the key to fast adsorption of H_2, which facilitated the formation of oxygen vacancies and subsequent adsorption of CO_2, resulting in high RWGS reactivity. Yan et al. found that rhombic indium oxide outperforms the cubic polymorph in terms of photothermal catalytic activity, long-term stability and selectivity for hydrogenating gaseous CO_2 to CO and CH_3OH. Because the higher acidity and basicity of the surface hindered Lewis pairs in the rhombic polymorph more effectively than in the cubic polymorph [31]. Li et al. [133] developed an explosive approach to synthesize pristine fluorite ZrO_2 nanosheets. By integrating this material with a custom-built photothermal reactor, they achieved a pure CO yield of 83 mmol g^{-1} h^{-1} and a photochemical energy conversion efficiency of 12.3 % under 0.5 sun irradiation. And the system also demonstrated considerable potential under natural sunlight. Liu et al. [176] constructed a Cu_2O@CuS@SnS_2 ternary core–shell thermal structure for efficient and selective photothermal catalytic reduction of CO_2 to C_2H_6. Under light irradiation, the photothermal effect of the CuS interlayer induces a temperature rise, promoting the transformation of SnS_2 from the 2H phase to the 1T phase, which exhibits enhanced C–C coupling activity. Moreover, this phase transition significantly optimizes the dynamics of photogenerated carriers, thereby accelerating the photoreduction reaction. This finding also suggests that the structural specificity of metastable phase materials

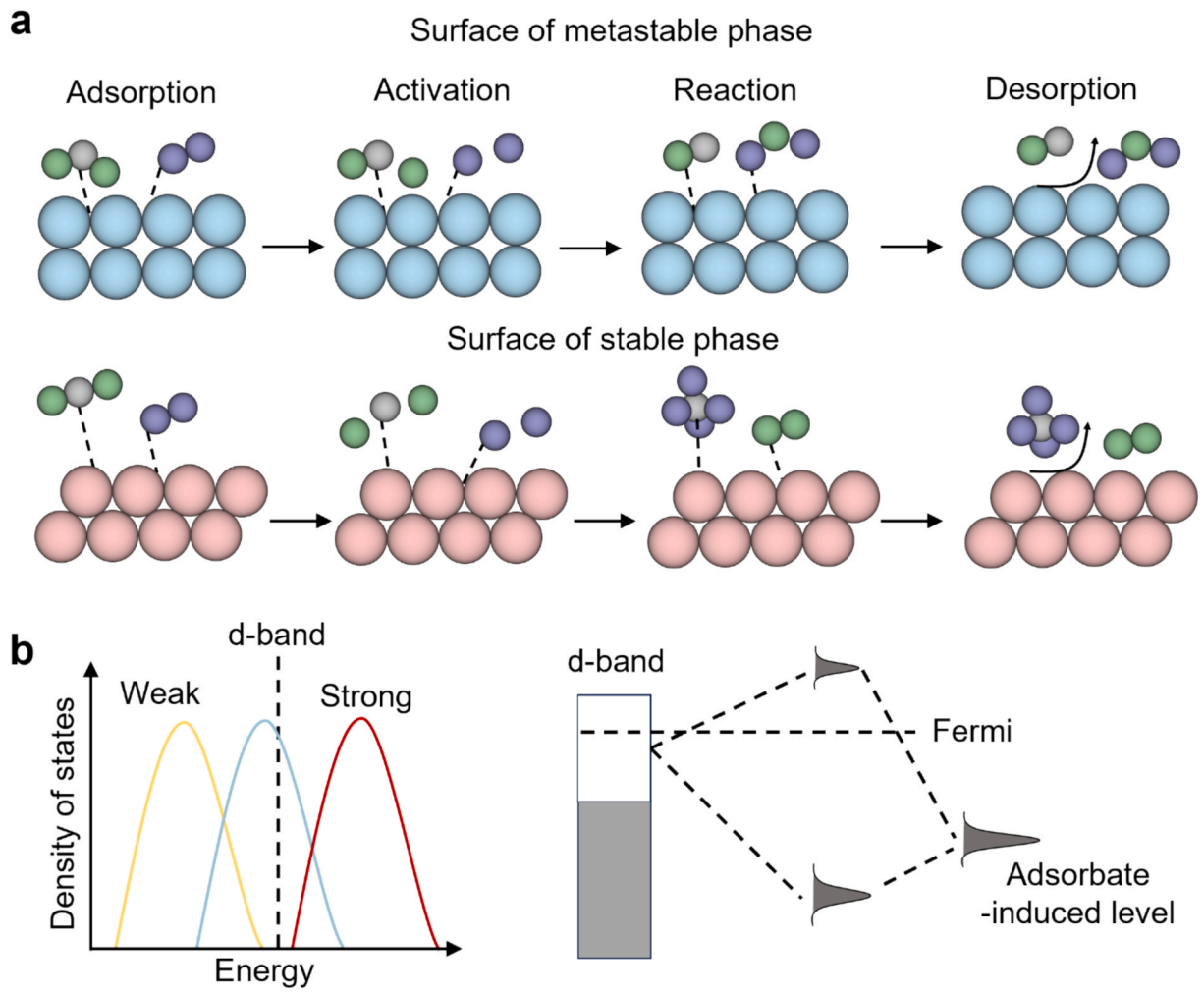

Fig. 22. Thermodynamic-kinetic adaptability of metastable phase materials in thermal catalysis. (a) Schematic illustration of the thermal catalytic process on the surfaces of metastable (blue atoms) and stable (red atoms) phase materials primarily involving four key steps, including adsorption, activation, surface reaction, and desorption of reactant molecules. (b) Adsorption behaviour based on d-band center theory, which links electronic structure to adsorption strength and catalytic activity. Adapted with permission [169]. Copyright 2024, Springer Nature. (For interpretation of the references to colour in this figure legend, the reader is referred to the web version of this article.)

may result in higher thermal conductivity and lower thermal radiation values, which could be advantageous for photothermal catalysis [177–179]. Moreover, undiscovered metastable phase materials may possess unique acid-base sites that could bring new opportunities for catalysis.

AI-assisted discovery of novel metastable phase materials

The discovery of novel metastable phase materials remains a considerable challenge, primarily due to the fundamental limitations of conventional thermodynamic phase diagrams. These diagrams, traditionally employed to predict equilibrium phases, fail to account for the complex formation of non-equilibrium products under fluctuating temperature and pressure conditions, thereby constraining the ability to predict and synthesize metastable phase materials with precision. This underscores the need for advanced, non-equilibrium modeling techniques to overcome these limitations and unlock new avenues in material design. Recent advances in artificial intelligence (AI), machine learning, and high-performance computing have paved the way for more accurate predictions and exploration of metastable phases. This section delves into the AI-assisted methodologies, including automated metastable phase diagrams (Fig. 24a), that are revolutionizing our understanding of these materials and their potential applications.

Researchers from the Argonne laboratory, for instance, have integrated first principles physics and atomic simulations with machine learning and high-performance computing to demonstrate the construction of an automated metastable phase diagram. This framework manages metastable structures from published literature/databases, while automatically discovering, identifying, and exploring novel metastable phase materials, and learning their state equations through deep neural networks (DNNs). Using carbon, which has many metastable allotropes as a case study, they constructed a metastable phase diagram over a wide range of temperatures (0–3000 K), pressures (0–100 GPa), and excess free energies (up to 400 meV atom^{-1} higher than thermodynamic equilibrium) [1]. Further research revealed that the transformation barrier from graphite to Z-carbon phase is lower than that from cubic diamond to the Z-carbon phase, indicating that graphite is the preferred starting material for achieving the Z-carbon metastable phase (Fig. 24b). The phase diagram provides a synthetic path to the metastable phase, as shown in Fig. 24c, showing a schematic diagram of the synthetic path on the energy scale in the Mg-Mo-N composition coordinate. The first step involves forming a high-energy, long-range disordered but short-range ordered RS-$MgMoN_2$ 3D crystal structure from gas-phase magnesium, molybdenum and nitrogen precursors. The second step transforms this 3D metastable intermediate structure into a stable layered 2D RL-$MgMoN_2$-like structure with short-range and long-

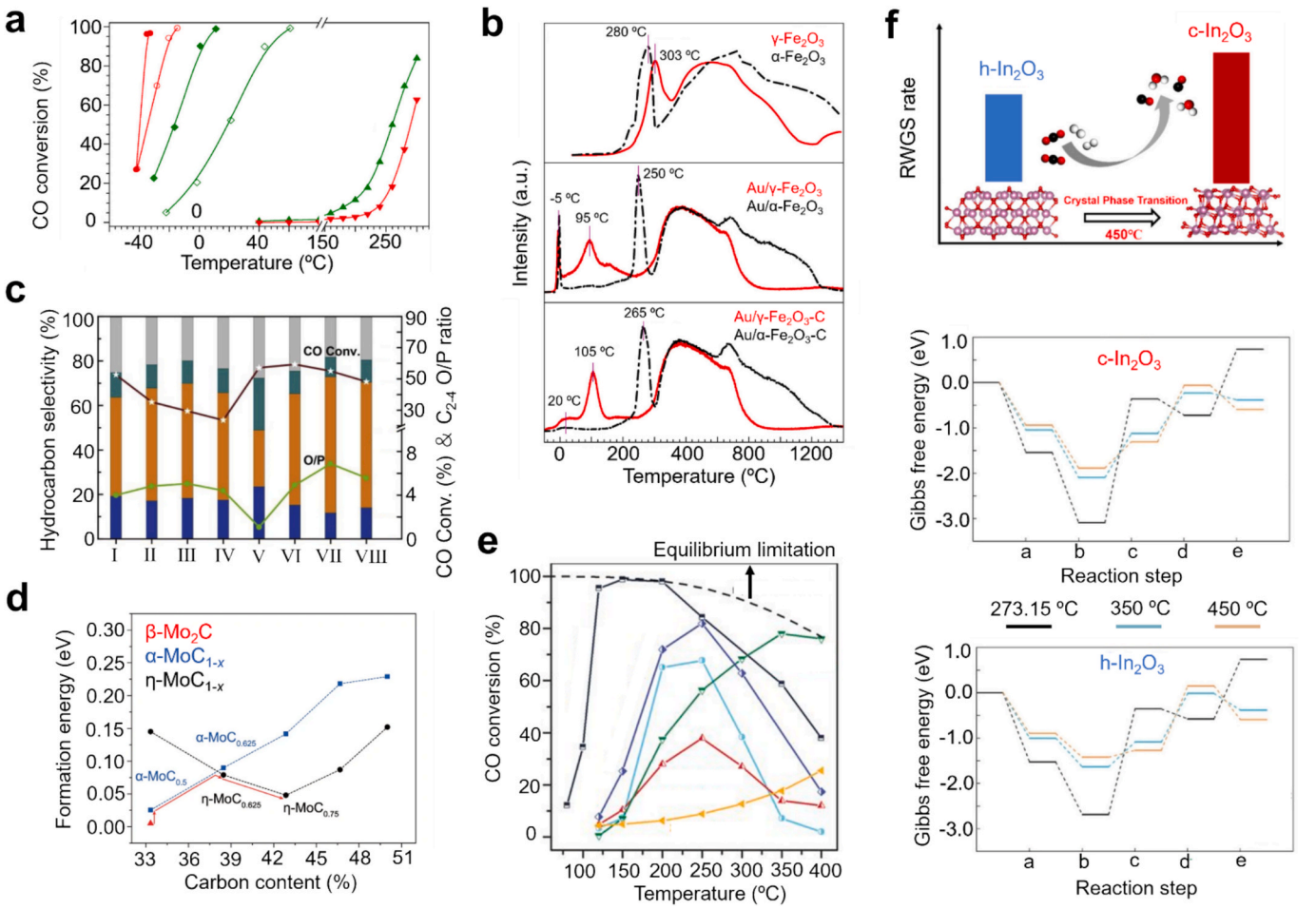

Fig. 23. Thermodynamic-kinetic adaptability of metastable phase materials in thermal catalysis. (a) CO conversion dependence on reaction temperature over different Au/Fe_2O_3 catalysts. The samples represented by the curves from left to right are Au/γ-Fe_2O_3-UC, Au/γ-Fe_2O_3-C3, Au/α-Fe_2O_3-UC, Au/α-Fe_2O_3-C3, α-Fe_2O_3 and γ-Fe_2O_3. Reproduced with permission [30]. Copyright 2015, American Chemical Society. (b) CO-TPR profiles of different catalysts. Reproduced with permission [30]. Copyright 2015, American Chemical Society. (c) Catalytic performance of different catalysts. I: α-Fe_2O_3; II: 0.3Mn/α-Fe_2O_3; III: 0.5Mn/α-Fe_2O_3; IV: 1Mn/α-Fe_2O_3; V: γ-Fe_2O_3; VI: 0.3Mn/γ-Fe_2O_3; VII: 0.5Mn/γ-Fe_2O_3; VIII: 1Mn/γ-Fe_2O_3. Reproduced under terms of the CC-BY license [29]. Copyright 2020, Elsevier. (d) Formation energy of samples with varying carbon atomic contents. Reproduced with permission [58]. Copyright 2022, Springer Nature. (e) CO conversion dependence on reaction temperature over different catalysts. Black curve: 2% Au/α-MoC; Blue curve: 0.9 % Au/α-MoC (NaCN); Cyan curve: α-MoC; Green curve: commercial Cu/ZnO/Al_2O_3; Red curve: 2 % Au/β-Mo_2C; Orange curve: 2 % Au/CeO_2. Reproduced with permission [171]. Copyright 2017, the American Association for the Advancement of Science. (f) Transition from h-In_2O_3 to c-In_2O_3 enhancing the RWGS reaction rate and reaction Gibbs free energy of the h-In_2O_3 (1 1 0) and c-In_2O_3 (1 1 1). Reproduced with permission [175]. Copyright 2020, American Chemical Society. (For interpretation of the references to colour in this figure legend, the reader is referred to the web version of this article.)

range cation order. In another example, $SrTiO_3$ is assigned to a set of appropriately dense discrete positions in space to obtain a candidate crystal structure, and then the structure prediction is completed by locally minimizing the low-energy assignment to provide the lowest energy structure with atomic positions in continuous space (Fig. 24d).

Aykol et al. [182] applied a fully ab initio procedure to approximate the energy of corresponding amorphous states, and calculated the amorphous structures of 41 materials along with the energy of their crystalline polymorphs relative to the ground state. On the one hand, the energy probability distribution functions (PDFs) of polycrystalline materials shows a heavy-tailed negative exponential distribution. On the other hand, there was a significant overlap between the low energy tails of the PDFs of the amorphous materials and the crystals. This suggests that amorphous structures remain more thermodynamically competitive and, to some extent, the amorphous phase structures are also metastable (Fig. 25a). Combined with phase analysis, new types of computer programs are developed to solve very complex problems using powerful algorithms and emerging quantum computers. Amil Merchant et al. from Google DeepMind used deep learning to predict the structures of 2.2 million new materials, of which over 700 have been sucessfully synthesized in the laboratory, greatly enriching the materials library [183]. However, managing such a huge amount of predictive data is challenging and inefficient relying solely on manual labor. In order to bridge the gap between computational screening and experimental realization of new materials, Ceder et al. built an autonomous experimental platform for inorganic powder synthesis (Fig. 25b) [184]. The platform integrates computational methods, historical data from the literature, machine learning, and active learning to plan and interpret the results of experiments conducted using robots. The synthesis formula is generated by a natural language model trained on literature data and optimized using a thermodynamics-based active learning method. The laboratory synthesized various oxides and phosphates, including those identified using large-scale ab initio phase stability data from the Materials Project and Google DeepMind. And the analysis of failed syntheses provides direct and actionable suggestions to improve current material screening and synthesis design techniques.

Meanwhile, these combinations hold great potential to accelerate the development of applications [185,186]. Likewise, the experimental

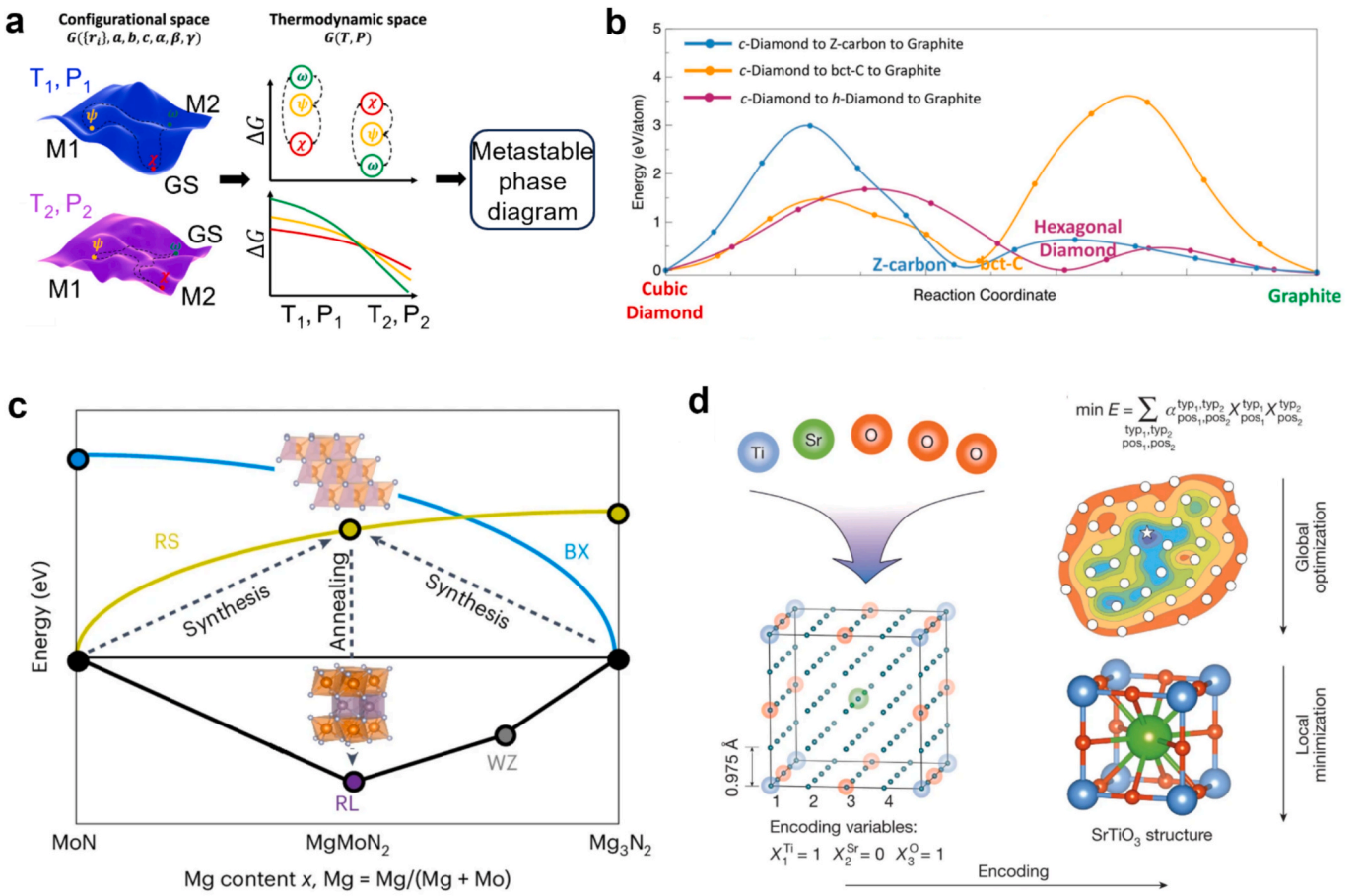

Fig. 24. Machine learning accelerates the establishment of metastable phase diagrams. (a) Schematic diagram of the process from free energy landscape to integration into metastable phase diagram. Reproduced with permission [1]. Copyright 2022, Springer Nature. (b) Conversion barrier curves of carbon materials with different structures. Reproduced with permission [1]. Copyright 2022, Springer Nature. (c) Competition diagram of different metastable phase nitrides. RS represents rocksalt structure and BX represents bixbyite structure. Reproduced with permission [180]. Copyright 2024, Springer Nature. (d) Crystal structure prediction using integer programming. A well-selected configured space leads to the correct crystal structure through a single local minimization of the global optimal allocation of the lowest energy. Reproduced with permission [181]. Copyright 2023, Springer Nature.

complexity of the application grows exponentially with the number of variables, limiting most searches to narrow regions of materials space. Robotic autonomous searches can identify more active components and can select beneficial elements while rejecting negative ones. This modular approach can be deployed in traditional laboratories to address a range of research questions related to new metastable phase materials. Considering the above discussions, the in-depth understanding of metastable phases has evolved from thermodynamic metastability to dynamic metastability and further to external potential field metastability, intertwined with concepts such as single atoms etc. By combining advanced simulations, data-driven approaches, and powerful computing technologies, researchers can now map out metastable phases with greater accuracy (Fig. 25c). Nevertheless, while these tools offer considerable promise, the practical applicability of metastable phase materials in industrial settings demands thorough, longitudinal validation and extensive research. It is essential to conduct a series of comprehensive, multidimensional assessments to critically evaluate the materials' thermodynamic stability, scalability, and performance under real-world conditions. Only through this rigorous approach can we ascertain their viability for integration into complex industrial processes, ensuring both reliability and operational sustainability over time.

The development of metastable phase catalysis requires a well-defined roadmap to minimize interference from its corresponding stable phase (Fig. 26). Details are as follows, metastable phase catalysis begins with the selection of catalytic scenarios, such as photocatalysis, electrocatalysis, or thermal catalysis. Catalyst design is then carried out, involving metals, compounds, or metastable phases predicted by AI or databases. Next, suitable synthesis strategies, including wet chemical, mechanochemical, or chemical vapor deposition methods, are employed. Subsequently, accurate characterization techniques, including X-ray diffraction and Raman spectroscopy, are used to ensure precise phase identification and structural analysis. Following characterization, catalytic performance is systematically evaluated in terms of yield, selectivity, durability, and scalability. The post-reaction diagnostics help to clarify phase evolution under working conditions. Furthermore, structure–activity relationship associated with high Gibbs free energy and variations in d-band centers are established. These insights, in turn, inform downstream development efforts that focus on exploiting thermodynamic and kinetic advantages, enabling automated synthesis, and assessing economic feasibility for potential large-scale applications.

Conclusions and prospects

In summary, we first introduced the concept of metastable phase catalysis to highlight the significance of metastable phase functionalization, followed by an in-depth exploration of the broader concept of metastability. In particular, we discussed the emerging phenomenon of dynamic metastability. We examined experimental strategies for regulating the stability of metastable phase materials during synthesis and demonstrated that these metastable phase materials can be functionalized while simultaneously enhancing their thermal stability. We also

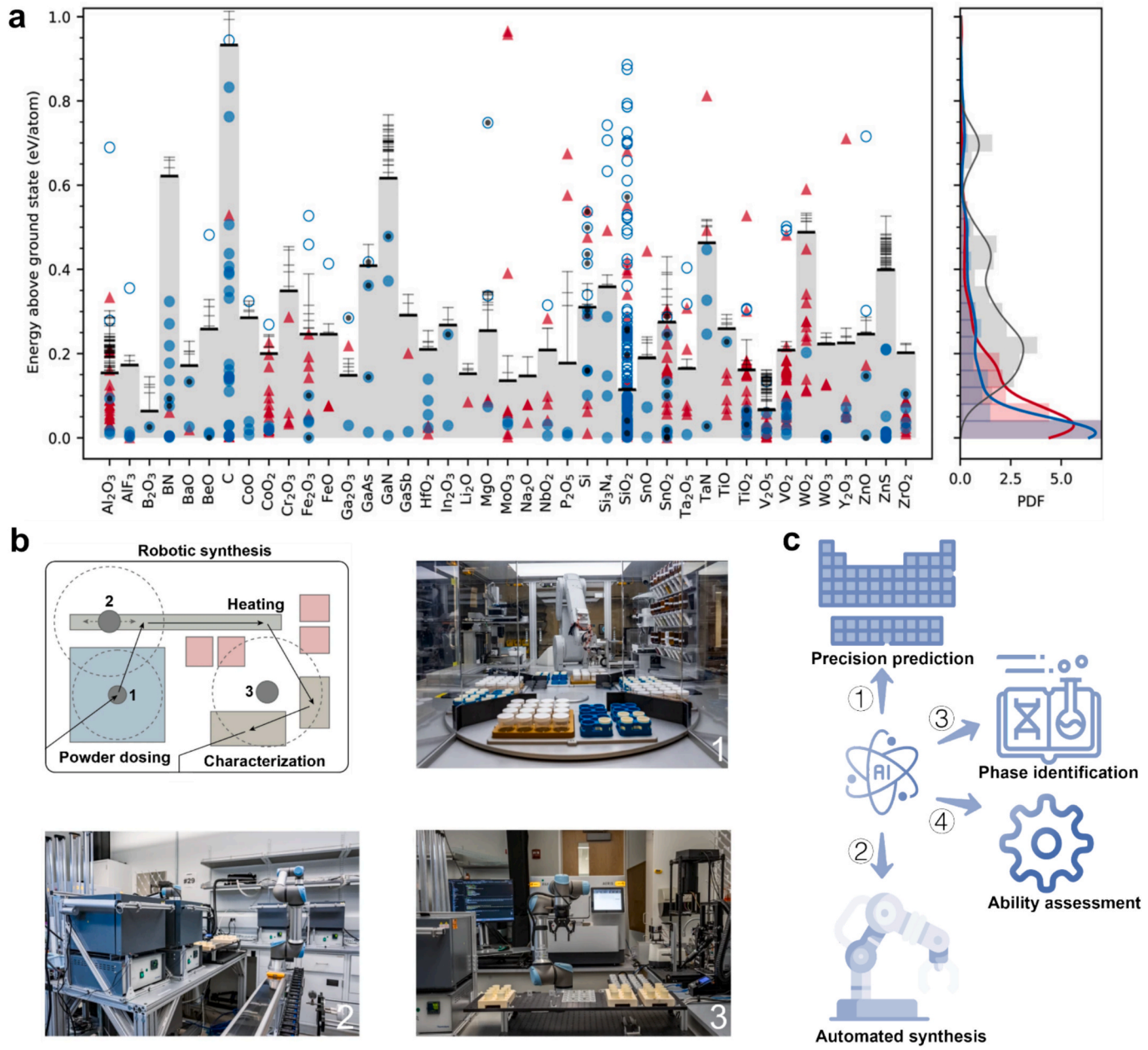

Fig. 25. Machine learning driven phase identification and autonomous materials synthesis. (a) Evaluation of the crystalline synthesizability of 41 material systems. Circles and triangles represent polymorphs with and without existing ICSD entries, respectively. An open circle indicates that the ICSD-identified polymorph lies above the amorphous limit and falls into at least one of the exception categories described in the text. Reproduced with permission [182]. Copyright 2018, the American Association for the Advancement of Science. (b) A robotic laboratory for automated powder batching, sample heating and phase characterization. Reproduced with permission [184]. Copyright 2023, Springer Nature. (c) An AI-assisted route for MPC with great prospects.

summarize the thermodynamic-kinetic adaptability of metastable phase materials under the influence of various external stimuli, including electricity, light and heat. These stimuli exhibit both distinct and overlapping effects on material behaviour. This adaptability is well exemplified in metastable metal oxides, where the interplay between lattice distortion, surface energy, charge transfer, and defect formation governs reactivity and selectivity across thermal, photo-, and electrochemical applications. We further discussed the potential of machine learning and theoretical calculations in studying metastable phase materials, and extended thermodynamic metastable phase materials to broader systems such as dynamic metastable phase materials. However, the integration of most metastable phase materials into the catalytic industry remains limited. Firstly, the development of metastable phase materials still relies on tedious experimental verification, and the inherent thermal instability poses challenges for macroscopic preparation, intrinsic properties, and easily occurring phase transition features of pure phase materials in practical application environments. Furthermore, modifications aimed at stabilizing metastable phase materials are constrained by their inherent instability, which affects the catalyst's long-term service life. Additionally, the micro mechanisms of transformations between different phases is still controversial, lacking a unified theoretical explanation. Therefore, in order to further enhance the application potential of metastable phase materials, it is necessary to consider the following aspects:

I. Developing efficient and high-quality synthesis processes for metastable phases: At present, the yield of metastable phase materials in the laboratory is poor, with numerous defects,

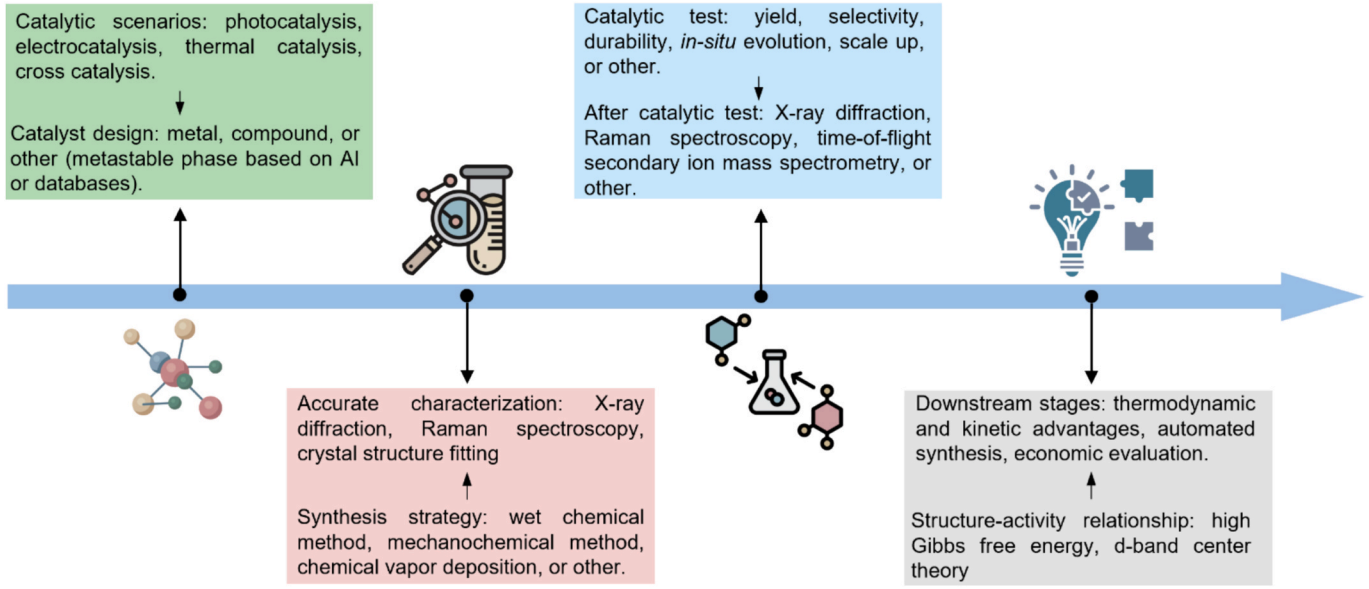

Fig. 26. A roadmap for developing metastable phase catalysis.

preventing full utilization of their intrinsic properties. In addition, emphasis should be placed on the preparation of metastable single crystals and the measurement of their electrical, magnetic and optical properties. By combining the thermodynamic properties of metastable phases, mechanochemical techniques that can rapidly and precisely adjust temperatures and pressure should be developed. This methodology may facilitate better control of the delicate balance between kinetics and thermodynamics, allowing the stabilization of phases that are otherwise inaccessible.

II. Stabilizing metastable phase materials in different catalytic environments: Efficient strategies should be explored to enhance thermal and chemical stability, ensuring that their unique properties are retained under operational conditions. Some of the techniques include doping to suppress atomic movement, surface coatings to suppress volume expansion and protection of the metastable phase from external environmental factors, such as oxygen, moisture, or reactive gases, that might otherwise destabilize it. Template support is another effective technique to counteract volume shrinkage and help maintain the metastable phase even under high temperatures or reactive conditions.

III. Deepening the understanding of active phases in metastable phase materials during practical reactions: for stable phases, research typically centers on identifying and optimizing the active site of mesophases that drive catalytic performance. However, metastable phase materials present unique challenges and opportunities, as their active phases can be more dynamic and less well-defined. It is crucial to first isolate the active phase during actual catalytic reactions, as metastable phases can undergo transformations under reaction conditions that affect their performance. This requires real-time monitoring techniques to capture transient states and dynamic changes in the catalyst structure. Once isolated, a detailed analysis of the electronic structures and active sites of these metastable phases is necessary to understand how they influence catalytic activity, selectivity, and stability. Investigating the interaction between the electronic configuration of active sites and reactants can reveal key insights into reaction pathways, energy barriers, and the overall efficiency of the catalytic process. So researchers can unlock new levels of performance that are not achievable with stable phases alone.

IV. Advanced characterization technologies have revolutionized materials research by enabling atomic-scale, real-time observation of dynamic processes. While metastable phase transitions have long concerned material scientists, traditional static observation methods failed to capture transient intermediate states. A critical challenge lies in developing non-destructive analysis techniques for metastable phase structures, where *in situ* environmental electron microscopy and atomic tomography have emerged as a powerful tool to explore transition micromechanisms. Cryo-electron microscopy preserves delicate structures during imaging, while operando spectroscopy (including synchrotron X-ray diffractometer, X-ray absorption spectroscopy, Raman spectra and infrared spectrum) reveals reaction pathways at active sites. These *in situ* techniques combine with emerging methods like AI-enhanced analysis and quantum sensing to provide comprehensive understanding of phase transitions in catalysts, energy materials, and biological systems. This paradigm shift enables unprecedented insights into metastable phenomena, from initial nucleation stage to final phase selection, fundamentally transforming our ability to design and optimize advanced functional materials.

V. Constructing metastable phase diagrams using machine learning and DFT calculations: Traditional phase diagrams primarily depict stable phases under equilibrium conditions, but the construction of metastable phase diagrams requires a different approach due to their complex, non-equilibrium nature. By utilizing machine learning and DFT calculations, researchers can predict and map the stability ranges and transformation pathways of metastable phases. The concept of metastable phases extends beyond conventional crystalline materials to include complex systems like amorphous materials, high-entropy materials, and atomic scale materials. The construction of metastable phase diagrams using these advanced computational tools requires collaboration of computational scientists who can develop and refine algorithms, validate predictions against experimental data, and interpret results to provide actionable insights. This interdisciplinary approach not only accelerates the discovery of new metastable phase materials but also guides their practical development by identifying optimal synthesis routes, predicting performance under different conditions, and suggesting modifications to enhance stability.

CRediT authorship contribution statement

Yuanming Zhang: Writing – review & editing, Writing – original draft, Visualization, Validation, Methodology, Investigation, Formal analysis, Data curation, Conceptualization. **Yang Li:** Writing – review & editing, Data curation. **Yong Chen:** Writing – review & editing. **Xiaoming Xu:** Writing – review & editing. **Zhonghua Li:** Writing – review & editing. **Tianxi Zhang:** Writing – review & editing. **Wei Li Ong:** Writing – review & editing. **Sergey M. Kozlov:** Writing – review & editing, Data curation. **Zhigang Zou:** Writing – review & editing, Supervision, Resources, Formal analysis, Data curation, Conceptualization. **Ghim Wei Ho:** Writing – review & editing, Project administration, Methodology, Formal analysis, Data curation, Conceptualization. **Zhaosheng Li:** Writing – review & editing, Supervision, Resources, Investigation, Data curation, Conceptualization.

Declaration of competing interest

The authors declare that they have no known competing financial interests or personal relationships that could have appeared to influence the work reported in this paper.

Acknowledgements

This work was financially supported by National Key Research and Development Program of China (No. 2023YFA1507104), National Natural Science Foundation of China (No. 22025202), and Natural Science Foundation of Jiangsu Province of China (No. BK20232021). This research is supported by A*STAR, under its RIE2025 Manufacturing, Trade and Connectivity (MTC), award Individual Research Grant (IRG award M23M6c0105) and Ministry of Education, Singapore, under the Academic Research Fund Tier 1 (FY2023), A-8002151-00-00.

Data availability

Data will be made available on request.

References

[1] S. Srinivasan, et al., Machine learning the metastable phase diagram of covalently bonded carbon, Nat. Commun. 13 (1) (2022) 3251.
[2] J. Chen, et al., Navigating phase diagram complexity to guide robotic inorganic materials synthesis, Nat. Synth. 3 (5) (2024) 606–614.
[3] Z. Wang, et al., Optimal thermodynamic conditions to minimize kinetic by-products in aqueous materials synthesis, Nat. Synth. 3 (4) (2024) 527–536.
[4] W. Sun, et al., The thermodynamic scale of inorganic crystalline metastability, Sci. Adv. 2 (11) (2016) e1600225.
[5] M. Bianchini, et al., The interplay between thermodynamics and kinetics in the solid-state synthesis of layered oxides, Nat. Mater. 19 (10) (2020) 1088–1095.
[6] Y. Wang, et al., Thermodynamics versus kinetics in nanosynthesis, Angew. Chem. Int. Ed. 54 (7) (2015) 2022–2051.
[7] B. Truc, et al., Light-induced metastable hidden skyrmion phase in the Mott insulator Cu_2OSeO_3, Adv. Mater. 35 (33) (2023) 2304197.
[8] T. Wang, et al., Pressure processing of nanocube assemblies toward harvesting of a metastable PbS phase, Adv. Mater. 27 (31) (2015) 4544–4549.
[9] G. Lin, et al., Intrinsic electron localization of metastable MoS_2 boosts electrocatalytic nitrogen reduction to ammonia, Adv. Mater. 33 (32) (2021) 2007509.
[10] Z. Wang, et al., Manipulation on active electronic states of metastable phase β-$NiMoO_4$ for large current density hydrogen evolution, Nat. Commun. 12 (1) (2021) 5960.
[11] W. Chen, et al., Millisecond conversion of metastable 2D materials by Flash Joule heating, ACS Nano 15 (1) (2021) 1282–1290.
[12] Y.-R. Zheng, et al., Doping-induced structural phase transition in cobalt diselenide enables enhanced hydrogen evolution catalysis, Nat. Commun. 9 (1) (2018) 2533.
[13] N. Zhang, et al., Paving the road toward the use of β-Fe_2O_3 in solar water splitting: Raman identification, phase transformation and strategies for phase stabilization, Natl. Sci. Rev. 7 (6) (2020) 1059–1067.
[14] X. Wang, et al., Photocatalytic overall water splitting promoted by an α–β phase junction on Ga_2O_3, Angew. Chem. Int. Ed. 51 (52) (2012) 13089–13092.
[15] Y. Shen, et al., Ferroelectric freestanding hafnia membranes with metastable rhombohedral structure down to 1-nm-thick, Nat. Commun. 15 (1) (2024) 4789.
[16] H. Hu, et al., Electrocatalytic oxygen reduction using metastable zirconium suboxide, Angew. Chem. Int. Ed. 63 (30) (2024) e202404374.
[17] K. Liu, et al., Coherent hexagonal platinum skin on nickel nanocrystals for enhanced hydrogen evolution activity, Nat. Commun. 14 (1) (2023) 2424.
[18] W. Wen, et al., Metastable phase Cu with optimized local electronic state for efficient electrocatalytic production of ammonia from nitrate, Adv. Funct. Mater. 33 (6) (2023) 2212236.
[19] X. Wang, et al., Design metastability in high-entropy alloys by tailoring unstable fault energies, Sci. Adv. 8 (36) (2022) eabo7333.
[20] J. Zhang, et al., Atomic-thick metastable phase RhMo nanosheets for hydrogen oxidation catalysis, Nat. Commun. 14 (1) (2023) 1761.
[21] S. Chen, et al., High-temperature superconductivity up to 223 K in the Al stabilized metastable hexagonal lanthanum superhydride, Natl. Sci. Rev. 11 (1) (2024) nwad107.
[22] S. Liu, et al., Modeling of metastable phase formation for sputtered $Ti_{1-x}Al_xN$ thin films, Acta Mater. 165 (2019) 615–625.
[23] X. Tan, et al., Closest packing polymorphism interfaced metastable transition metal for efficient hydrogen evolution, Adv. Mater. 32 (40) (2020) 2002857.
[24] C. Liu, et al., A metastable crystalline phase in two-dimensional metallic oxide nanoplates, Angew. Chem. Int. Ed. 58 (7) (2019) 2055–2059.
[25] Z. Shi, et al., Phase-dependent growth of Pt on MoS_2 for highly efficient H_2 evolution, Nature 621 (7978) (2023) 300–305.
[26] Y. Yang, et al., Anomalous enhancement of the Nernst effect at the crossover between a Fermi liquid and a strange metal, Nat. Phys. 19 (3) (2023) 379–385.
[27] C. Gu, et al., Soft chemistry of metastable metal chalcogenide nanomaterials, Chem. Soc. Rev. 50 (12) (2021) 6671–6683.
[28] J. Hu, et al., Understanding the phase-induced electrocatalytic oxygen evolution reaction activity on FeOOH nanostructures, ACS Catal. 9 (12) (2019) 10705–10711.
[29] Y. Liu, et al., Effects of initial crystal structure of Fe_2O_3 and Mn promoter on effective active phase for syngas to light olefins, Appl. Catal. B 261 (2020) 118219.
[30] K. Zhao, et al., High activity of Au/γ-Fe_2O_3 for CO oxidation: effect of support crystal phase in catalyst design, ACS Catal. 5 (6) (2015) 3528–3539.
[31] T. Yan, et al., Polymorph selection towards photocatalytic gaseous CO_2 hydrogenation, Nat. Commun. 10 (1) (2019) 2521.
[32] C. Yang, et al., Fe_5C_2 nanoparticles: a facile bromide-induced synthesis and as an active phase for Fischer–Tropsch synthesis, J. Am. Chem. Soc. 134 (38) (2012) 15814–15821.
[33] L. Yu, et al., Shell-induced ostwald ripening: simultaneous structure, composition, and morphology transformations during the creation of hollow iron oxide nanocapsules, ACS Nano 12 (9) (2018) 9051–9059.
[34] P. Wu, et al., Interfacial effects in hierarchically porous α-MnO_2/Mn_3O_4 heterostructures promote photocatalytic oxidation activity, Appl. Catal. B 268 (2020) 118418.
[35] J. Li, et al., Multiple structural and phase transformations of MOF and selective hydrocarbon gas separation in its amorphous, glass phase states, Angew. Chem. Int. Ed. 64 (9) (2025) e202411150.
[36] E. Jiang, et al., Zero- to one-dimensional transformation in a highly porous metal–organic framework to enhance physicochemical properties, J. Am. Chem. Soc. 147 (20) (2025) 16766–16772.
[37] Y. Li, et al., Origin of enhanced oxygen evolution in restructured metal–organic frameworks for anion exchange membrane water electrolysis, Angew. Chem. Int. Ed. 64 (1) (2025) e202413916.
[38] F. Auras, et al., Dynamic two-dimensional covalent organic frameworks, Nat. Chem. 16 (8) (2024) 1373–1380.
[39] A. Yao, et al., Guest-induced structural transformation of single-crystal 3D covalent organic framework at room and high temperatures, Nat. Commun. 16 (1) (2025) 1385.
[40] B. Qiao, et al., Single-atom catalysis of CO oxidation using Pt_1/FeO_x, Nat. Chem. 3 (8) (2011) 634–641.
[41] A. Walther, Viewpoint: from responsive to adaptive and interactive materials and materials systems: a roadmap, Adv. Mater. 32 (20) (2020) 1905111.
[42] H. Jin, et al., Metastable two-dimensional materials for electrocatalytic energy conversions, Acc. Mater. Res. 2 (7) (2021) 559–573.
[43] P.M. Maffettone, et al., Crystallography companion agent for high-throughput materials discovery, Nat. Comput. Sci. 1 (4) (2021) 290–297.
[44] Q. Zhu, et al., Soft hydrogen-bonded organic frameworks constructed using a flexible organic cage hinge, J. Am. Chem. Soc. 145 (42) (2023) 23352–23360.
[45] Q. Wang, et al., Photoinduced metastable asymmetric Cu single atoms for photoreduction of CO_2 to ethylene, Adv. Energy Mater. 13 (42) (2023) 2302692.
[46] E. Pastor, et al., Electronic defects in metal oxide photocatalysts, Nat. Rev. Mater. 7 (7) (2022) 503–521.
[47] Y. Sun, et al., Covalency competition dominates the water oxidation structure–activity relationship on spinel oxides, Nat. Catal. 3 (7) (2020) 554–563.
[48] K. Sun, et al., Dynamic structural twist in metal–organic frameworks enhances solar overall water splitting, Nat. Chem. 16 (10) (2024) 1638–1646.
[49] X. Zhang, et al., Dynamic structural evolution of single-atom catalysts at the catalyst–electrolyte interface: insights from electrochemical coupled field, Nano Lett. 25 (15) (2025) 6332–6339.
[50] L. Zhang, et al., Direct observation of dynamic bond evolution in single-atom Pt/C_3N_4 catalysts, Angew. Chem. Int. Ed. 59 (15) (2020) 6224–6229.
[51] J. Yang, et al., Potential-driven restructuring of Cu single atoms to nanoparticles for boosting the electrochemical reduction of nitrate to ammonia, J. Am. Chem. Soc. 144 (27) (2022) 12062–12071.
[52] M.S. Sokolikova, C. Mattevi, Direct synthesis of metastable phases of 2D transition metal dichalcogenides, Chem. Soc. Rev. 49 (12) (2020) 3952–3980.

[53] W. Sun, G. Ceder, Induction time of a polymorphic transformation, CrstEngComm 19 (31) (2017) 4576–4585.
[54] J. Hong, et al., Metastable hexagonal close-packed palladium hydride in liquid cell TEM, Nature 603 (7902) (2022) 631–636.
[55] B.-R. Chen, et al., Understanding crystallization pathways leading to manganese oxide polymorph formation, Nat. Commun. 9 (1) (2018) 2553.
[56] Y. Li, et al., Metastable-phase β-Fe_2O_3 photoanodes for solar water splitting with durability exceeding 100 h, Chin. J. Catal. 42 (11) (2021) 1992–1998.
[57] H. Yang, et al., Metastable-phase platinum oxide for clarifying the Pt–O active site for the hydrogen evolution reaction, Energ. Environ. Sci. 16 (2) (2023) 574–583.
[58] B. Deng, et al., Phase controlled synthesis of transition metal carbide nanocrystals by ultrafast flash Joule heating, Nat. Commun. 13 (1) (2022) 262.
[59] X. Cui, Y. Liu, Y. Chen, Ultrafast micro/nano-manufacturing of metastable materials for energy, Natl. Sci. Rev. 11 (4) (2024) nwae033.
[60] M.S. Sokolikova, et al., Direct solution-phase synthesis of 1T' WSe_2 nanosheets, Nat. Commun. 10 (1) (2019) 712.
[61] Y.-H. Song, et al., Planar defect–free pure red perovskite light-emitting diodes via metastable phase crystallization, Sci. Adv. 8 (45) (2022) eabq2321.
[62] L. Liu, et al., Phase-selective synthesis of 1T′ MoS_2 monolayers and heterophase bilayers, Nat. Mater. 17 (12) (2018) 1108–1114.
[63] Y. Yu, et al., High phase-purity 1T′-MoS_2- and 1T′-$MoSe_2$-layered crystals, Nat. Chem. 10 (6) (2018) 638–643.
[64] Z. Lai, et al., Metastable 1T′-phase group VIB transition metal dichalcogenide crystals, Nat. Mater. 20 (8) (2021) 1113–1120.
[65] Z. Fan, et al., Extraordinary acidic oxygen evolution on new phase 3R-iridium oxide, Joule 5 (12) (2021) 3221–3234.
[66] Q. Dang, et al., Iridium metallene oxide for acidic oxygen evolution catalysis, Nat. Commun. 12 (1) (2021) 6007.
[67] F. Liao, et al., Iridium oxide nanoribbons with metastable monoclinic phase for highly efficient electrocatalytic oxygen evolution, Nat. Commun. 14 (1) (2023) 1248.
[68] Y. Zhang, et al., Metastable hexagonal phase SnO_2 nanoribbons with active edge sites for efficient hydrogen peroxide electrosynthesis in neutral media, Angew. Chem. Int. Ed. 135 (20) (2023) e202218924.
[69] Y. Nagaoka, et al., Nanocube superlattices of cesium lead bromide perovskites and pressure-induced phase transformations at atomic and mesoscale levels, Adv. Mater. 29 (18) (2017) 1606666.
[70] Q. Liu, S.W. Chen, Ultrafast synthesis of electrocatalysts, Trends Chem. 4 (10) (2022) 918–934.
[71] Q. Chen, et al., Rapid synthesis of metastable materials for electrocatalysis, Chem. Soc. Rev. 54 (9) (2025) 4567–4616.
[72] C. Liu, et al., Multiple twin boundary-regulated metastable Pd for ethanol oxidation reaction, Adv. Energy Mater. 12 (8) (2022) 2103505.
[73] C. Yang, et al., Overcoming immiscibility toward bimetallic catalyst library, Sci. Adv. 6 (17) (2020) eaaz6844.
[74] W. Yan, et al., PCTS-controlled synthesis of $L1_0$/$L1_2$-typed Pt-Mn intermetallics for electrocatalytic oxygen reduction, Adv. Funct. Mater. 34 (6) (2024) 2310487.
[75] M. Cui, et al., Rapid atomic ordering transformation toward intermetallic nanoparticles, Nano Lett. 22 (1) (2022) 255–262.
[76] Q. Yun, et al., Recent progress on phase engineering of nanomaterials, Chem. Rev. 123 (23) (2023) 13489–13692.
[77] Q.A. Akkerman, et al., Ultrathin orthorhombic PbS nanosheets, Chem. Mater. 31 (19) (2019) 8145–8153.
[78] D.V. Talapin, et al., Seeded growth of highly luminescent CdSe/CdS nanoheterostructures with rod and tetrapod morphologies, Nano Lett. 7 (10) (2007) 2951–2959.
[79] A. Khannanov, et al., γ-Iron phase stabilized at room temperature by thermally processed graphene oxide, J. Am. Chem. Soc. 140 (29) (2018) 9051–9055.
[80] C. Wang, et al., Revealing the role of electrocatalyst crystal structure on oxygen evolution reaction with nickel as an example, Small 14 (40) (2018) 1802895.
[81] M. Okada, et al., Large-scale 1T′-phase tungsten disulfide atomic layers grown by gas-source chemical vapor deposition, ACS Nano 16 (8) (2022) 13069–13081.
[82] Y. Zhao, et al., Experimental evidence of room-temperature ferromagnetism in semiconducting MnS_2, J. Am. Chem. Soc. (2025).
[83] V. Martinez, et al., Advancing mechanochemical synthesis by combining milling with different energy sources, Nat. Rev. Chem. 7 (1) (2023) 51–65.
[84] M. Achimovičová, et al., Characterization of mechanochemically synthesized ZnSe in a laboratory and an industrial mill, Solid State Ion. 192 (1) (2011) 632–637.
[85] E. Ma, M. Atzmon, F.E. Pinkerton, Thermodynamic and magnetic properties of metastable Fe_xCu_{100-x} solid solutions formed by mechanical alloying, J. Appl. Phys. 74 (2) (1993) 955–962.
[86] Y. Sun, et al., Multiple-step phase transformation in silver nanoplates under high pressure, Small 7 (5) (2011) 606–611.
[87] X. Lü, et al., Pressure-induced amorphization in single-crystal Ta_2O_5 nanowires: a kinetic mechanism and improved electrical conductivity, J. Am. Chem. Soc. 135 (37) (2013) 13947–13953.
[88] S. Han, et al., Gas-assisted transformation of gold from fcc to the metastable 4H phase, Nat. Commun. 11 (1) (2020) 552.
[89] M.-R. He, R. Yu, J. Zhu, Reversible Wurtzite–tetragonal reconstruction in ZnO 1010 surfaces, Angew. Chem. Int. Ed. 51 (31) (2012) 7744–7747.
[90] H. Xia, et al., Evolution of stabilized 1T-MoS_2 by atomic-interface engineering of 2H-MoS_2/Fe−N towards enhanced sodium ion storage, Angew. Chem. Int. Ed. 62 (14) (2023) e202218282.
[91] F. Ge, et al., Elucidating facet-dependent photocatalytic activities of metastable CdS and Au@CdS core–shell nanocrystals, ACS Appl. Mater. Interfaces 16 (25) (2024) 32847–32856.
[92] H. Jiang, et al., Vapor deposition of bilayer 3R MoS_2 with room-temperature ferroelectricity, Adv. Mater. 36 (32) (2024) 2400670.
[93] Q. Wang, et al., 2D metastable-phase hafnium oxide triggers hydrogen spillover for boosting hydrogen production, Adv. Mater. 37 (13) (2025) 2415978.
[94] Z. Hong, et al., Completely solvent-free protocols to access phase-pure, metastable metal halide perovskites and functional photodetectors from the precursor salts, iScience 16 (2019) 312–325.
[95] Z. Li, et al., Mechanochemistry of lithium nitride under hydrogen gas, PCCP 17 (34) (2015) 21927–21934.
[96] K. Uusi-Esko, et al., Characterization of $RMnO_3$ (R=Sc, Y, Dy-Lu): High-pressure synthesized metastable perovskites and their hexagonal precursor phases, Mater. Chem. Phys. 112 (3) (2008) 1029–1034.
[97] J. López-Solano, et al., Theoretical and experimental study of the structural stability of $TbPO_4$ at high pressures, Phys. Rev. B 81 (14) (2010) 144126.
[98] A.P. Solomon, et al., Atomic-scale structure of ZrO_2: formation of metastable polymorphs, Sci. Adv. 11 (1) (2025) eadq5943.
[99] Y. Bu, et al., Activating deformation twinning in cubic boron nitride, Nat. Mater. 24 (3) (2025) 361–368.
[100] Y. Inaguma, et al., High-pressure synthesis, crystal structure, and phase stability relations of a $LiNbO_3$-type polar titanate $ZnTiO_3$ and its reinforced polarity by the second-order Jahn–Teller effect, J. Am. Chem. Soc. 136 (7) (2014) 2748–2756.
[101] V.D. Wheeler, et al., Phase control of crystalline Ga_2O_3 films by plasma-enhanced atomic layer deposition, Chem. Mater. 32 (3) (2020) 1140–1152.
[102] C. Wu, et al., Monoatomic platinum-anchored metallic MoS_2: correlation between surface dopant and hydrogen evolution, J. Phys. Chem. Lett. 10 (20) (2019) 6081–6087.
[103] M.D. Capobianco, et al., Terahertz conductivity of semiconducting 2H and metallic 1T phases of molybdenum disulfide, J. Phys. Chem. Lett. 13 (35) (2022) 8319–8326.
[104] A.D. Mohite, J.-C. Blancon, Scaling-up phase selection, Nat. Mater. 17 (12) (2018) 1058–1059.
[105] C. Li, et al., Superconductivity in quasi-one-dimensional ferromagnet $CrSbSe_3$ under high pressure, J. Am. Chem. Soc. 146 (14) (2024) 9688–9696.
[106] Z. Deng, et al., A pressure-induced inverse order–disorder transition in double perovskites, Angew. Chem. Int. Ed. 59 (21) (2020) 8240–8246.
[107] Z. Deng, et al., Giant exchange-bias-like effect at low cooling fields induced by pinned magnetic domains in Y_2NiIrO_6 double perovskite, Adv. Mater. 35 (17) (2023) 2209759.
[108] M. Weidemann, et al., High-pressure synthesis of Ruddlesden–Popper nitrides, Nat. Chem. 16 (2024) 1723–1731.
[109] L. Dubrovinsky, et al., Materials synthesis at terapascal static pressures, Nature 605 (7909) (2022) 274–278.
[110] T. Xiao, et al., Nanocrystals with metastable high-pressure phases under ambient conditions, Science 377 (6608) (2022) 870–874.
[111] L. Yue, et al., Radical n–p conduction switching and significant photoconductivity enhancement in $NbOI_2$ via pressure-modulated peierls distortion, J. Am. Chem. Soc. 146 (36) (2024) 25245–25252.
[112] F. Coppari, et al., Implications of the iron oxide phase transition on the interiors of rocky exoplanets, Nat. Geosci. 14 (3) (2021) 121–126.
[113] L. Liu, et al., A metastable pentagonal 2D material synthesized by symmetry-driven epitaxy, Nat. Mater. 23 (2024) 1339–1346.
[114] K. Eom, et al., Surface triggered stabilization of metastable charge-ordered phase in $SrTiO_3$, Nat. Commun. 15 (1) (2024) 1180.
[115] J. Zhang, et al., Cooperative photoinduced metastable phase control in strained manganite films, Nat. Mater. 15 (9) (2016) 956–960.
[116] R. Wang, et al., Defect engineering in metastable phases of transition-metal dichalcogenides for electrochemical applications, Chem. – Asian J. 15 (23) (2020) 3961–3972.
[117] X. Chen, et al., High phase-purity 1T-MoS_2 ultrathin nanosheets by a spatially confined template, Angew. Chem. Int. Ed. 58 (49) (2019) 17621–17624.
[118] X. Zheng, et al., Phase and polarization modulation in two-dimensional In_2Se_3 via in situ transmission electron microscopy, Sci. Adv. 8 (42) (2022) eabo0773.
[119] W. Han, et al., Phase-controllable large-area two-dimensional In_2Se_3 and ferroelectric heterophase junction, Nat. Nanotechnol. 18 (1) (2023) 55–63.
[120] A. Han, et al., One-step synthesis of single-site vanadium substitution in 1T-WS_2 monolayers for enhanced hydrogen evolution catalysis, Nat. Commun. 12 (1) (2021) 709.
[121] M. D'Andria, T.E.-R. Silva, E. Consogno, F. Krumeich, A.T. Güntner, Metastable $CoCu_2O_3$ nanocrystals from combustion-aerosols for molecular sensing and catalysis, Adv. Mater. 36 (47) (2024) 2408888.
[122] S. Geng, et al., Two-dimensional confined synthesis of metastable 1T-phase MoS_2 nanosheets for the hydrogen evolution reaction, ACS Appl. Nano Mater. 5 (1) (2022) 1377–1384.
[123] D.S. Baek, et al., Metastable phase-controlled synthesis of mesoporous molybdenum carbides for efficient alkaline hydrogen evolution, ACS Catal. 12 (12) (2022) 7415–7426.
[124] K. Lee, et al., Epitaxial stabilization and oxygen evolution reaction activity of metastable columbite iridium oxide, ACS Appl. Energy Mater. 4 (4) (2021) 3074–3082.
[125] X. Wang, et al., Hierarchically porous metastable β-Ag_2WO_4 hollow nanospheres: controlled synthesis and high photocatalytic activity, Nanotechnology 24 (16) (2013) 165602.

[126] H. Mogi, et al., Control of the photocatalytic activity of metastable layered oxynitride $K_2LaTa_2O_6N$ through topochemical transformation of tuned oxide precursors, Chem. Mater. 33 (16) (2021) 6443–6452.
[127] G. Ren, M. Zhou, H. Wang, Weakened interfacial hydrogen bond connectivity drives selective photocatalytic water oxidation toward H_2O_2 at water/brookite-TiO_2 interface, J. Am. Chem. Soc. 146 (9) (2024) 6084–6093.
[128] S.M.H. Hejazi, et al., Defect engineering over anisotropic brookite toward substrate-specific photo-oxidation of alcohols, Chem Catal. 2 (5) (2022) 1177–1190.
[129] G. Carraro, et al., Enhanced hydrogen production by photoreforming of renewable oxygenates through nanostructured Fe_2O_3 polymorphs, Adv. Funct. Mater. 24 (3) (2014) 372–378.
[130] J.D. Emery, et al., Atomic layer deposition of metastable β-Fe_2O_3 via isomorphic epitaxy for photoassisted water oxidation, ACS Appl. Mater. Interfaces 6 (24) (2014) 21894–21900.
[131] N. Zhang, et al., A beta-Fe_2O_3 nanoparticle-assembled film for photoelectrochemical water splitting, Dalton Trans. 46 (32) (2017) 10673–10677.
[132] H. Yin, et al., Epitaxial growth of phase-pure and stable β-Fe_2O_3 films by the pulsed laser deposition method, J. Mater. Chem. A 13 (2025) 10701–10708.
[133] Y. Li, et al., High-purity carbon monoxide production via photothermal formic acid decomposition over fluorite ZrO_2, Nat. Catal. 7 (12) (2024) 1350–1358.
[134] J.T. Mefford, et al., Correlative operando microscopy of oxygen evolution electrocatalysts, Nature 593 (7857) (2021) 67–73.
[135] W. Feng, et al., Proton exchange membrane water splitting: advances in electrode structure and mass-charge transport optimization, Adv. Mater. 37 (15) (2025) 2416012.
[136] D. Escalera-López, et al., Allotrope-dependent activity-stability relationships of molybdenum sulfide hydrogen evolution electrocatalysts, Nat. Commun. 15 (1) (2024) 3601.
[137] J. Su, X. Huang, Q. Shao, Emerging two dimensional metastable-phase oxides: insights and prospects in synthesis and catalysis, Angew. Chem. Int. Ed. 63 (11) (2024) e202318028.
[138] Z. Xu, et al., Recent advances in microenvironment regulation for electrocatalysis, Natl. Sci. Rev. 11 (12) (2024) nwae315.
[139] A. Kulkarni, et al., Understanding catalytic activity trends in the oxygen reduction reaction, Chem. Rev. 118 (5) (2018) 2302–2312.
[140] H. Luo, Y. Jin, Q. Shao, Metastable-phase two-dimensional metal oxides for advanced electrocatalysis, Chem. Mater. 36 (13) (2024) 6310–6320.
[141] A.J. Medford, et al., From the Sabatier principle to a predictive theory of transition-metal heterogeneous catalysis, J. Catal. 328 (2015) 36–42.
[142] R. Jiang, et al., Non-equilibrium synthesis of stacking faults-abundant Ru nanoparticles towards electrocatalytic water splitting, Appl. Catal. B 316 (2022) 121682.
[143] J. Li, Oxygen evolution reaction in energy conversion and storage: design strategies under and beyond the energy scaling relationship, Nano-Micro Lett. 14 (1) (2022) 112.
[144] J.K. Nørskov, et al., Density functional theory in surface chemistry and catalysis, Proc. Natl. Acad. Sci. 108 (3) (2011) 937–943.
[145] J. Xu, et al., Semimetal 1H-SnS_2 enables high-efficiency electroreduction of CO_2 to CO, Small Methods 4 (10) (2020) 2000567.
[146] Z. Xing, et al., High-efficiency electrochemical hydrogen evolution catalyzed by tungsten phosphide submicroparticles, ACS Catal. 5 (1) (2015) 145–149.
[147] S. Corby, et al., The kinetics of metal oxide photoanodes from charge generation to catalysis, Nat. Rev. Mater. 6 (12) (2021) 1136–1155.
[148] W. Wang, et al., Effects of transition metal doping on electronic structure of metastable β-Fe2O3 photocatalyst for solar-to-hydrogen conversion, PCCP 24 (11) (2022) 6958–6963.
[149] N. Zhang, et al., Onset potential shift of water oxidation in the metastable phase transformation process of β-Fe_2O_3, Energy Fuel 36 (19) (2022) 11567–11575.
[150] C. Liu, et al., Long-term durability of metastable β-Fe_2O_3 photoanodes in highly corrosive seawater, Nat. Commun. 14 (1) (2023) 4266.
[151] Y. Zhang, et al., Heterogeneous degradation of organic contaminants in the photo-Fenton reaction employing pure cubic β-Fe_2O_3, Appl Catal B 245 (2019) 410–419.
[152] X. Xu, et al., Revealing *OOH key intermediates and regulating H_2O_2 photoactivation by surface relaxation of Fenton-like catalysts, Proc. Natl. Acad. Sci. 119 (36) (2022) e2205562119.
[153] Y. Guo, et al., A novel wide-spectrum response hexagonal $YFeO_3$ photoanode for solar water splitting, RSC Adv. 7 (30) (2017) 18418–18420.
[154] L.T. Quynh, et al., Self-assembled $BiFeO_3$-ε-Fe_2O_3 vertical heteroepitaxy for visible light photoelectrochemistry, Adv. Energy Mater. 6 (18) (2016) 1600686.
[155] M.-G. Ju, et al., Tuning the energy band-gap of crystalline gallium oxide to enhance photocatalytic water splitting: mixed-phase junctions, J. Mater. Chem. A 2 (40) (2014) 17005–17014.
[156] P. Yan, et al., Photovoltaic device based on TiO_2 rutile/anatase phase junctions fabricated in coaxial nanorod arrays, Nano Energy 15 (2015) 406–412.
[157] A. Li, et al., Understanding the anatase–rutile phase junction in charge separation and transfer in a TiO_2 electrode for photoelectrochemical water splitting, Chem. Sci. 7 (9) (2016) 6076–6082.
[158] Y. Gao, et al., Directly probing charge separation at interface of TiO_2 phase Junction, J. Phys. Chem. Lett. 8 (7) (2017) 1419–1423.
[159] J. Qu, et al., Unraveling the role of interface in photogenerated charge separation at the anatase/rutile heterophase junction, J. Phys. Chem. C 127 (1) (2023) 768–775.
[160] F. Liu, et al., Direct Z-scheme hetero-phase junction of black/red phosphorus for photocatalytic water splitting, Angew. Chem. Int. Ed. 58 (34) (2019) 11791–11795.
[161] H. Xiong, et al., Controllable synthesis of mesoporous TiO_2 polymorphs with tunable crystal structure for enhanced photocatalytic H_2 production, Adv. Energy Mater. 9 (31) (2019) 1901634.
[162] Q.-S. Huang, et al., Interface-confined intermediate phase in TiO_2 enables efficient photocatalysis, Proc. Natl. Acad. Sci. 121 (6) (2024) e2318341121.
[163] A. Ashok, et al., Mesoporous metastable $CuTe_2$ semiconductor, J. Am. Chem. Soc. 145 (43) (2023) 23461–23469.
[164] R. Guo, et al., Epitaxial growth of metastable phase α-Ag_2MoO_4 on WO_3 surface: Visible light-driven photocatalysis, sterilization, and reaction mechanism, J. Alloy. Compd. 814 (2020) 152255.
[165] M. Ahmadi Khoshooei, et al., An active, stable cubic molybdenum carbide catalyst for the high-temperature reverse water-gas shift reaction, Science 384 (6695) (2024) 540–546.
[166] L. Chen, et al., Ternary NiMo-Bi liquid alloy catalyst for efficient hydrogen production from methane pyrolysis, Science 381 (6660) (2023) 857–861.
[167] K. Zuraiqi, et al., Unveiling metal mobility in a liquid Cu–Ga catalyst for ammonia synthesis, Nat. Catal. 7 (9) (2024) 1044–1052.
[168] R.M. Bullock, et al., Using nature's blueprint to expand catalysis with Earth-abundant metals, Science 369 (6505) (2020) eabc3183.
[169] X. Zhang, et al., Enhancing photocatalytic H_2O_2 production with Au co-catalysts through electronic structure modification, Nat. Commun. 15 (1) (2024) 3212.
[170] L. Lin, et al., Low-temperature hydrogen production from water and methanol using Pt/α-MoC catalysts, Nature 544 (7648) (2017) 80–83.
[171] S. Yao, et al., Atomic-layered Au clusters on α-MoC as catalysts for the low-temperature water-gas shift reaction, Science 357 (6349) (2017) 389–393.
[172] X. Zhang, et al., A stable low-temperature H_2-production catalyst by crowding Pt on α-MoC, Nature 589 (7842) (2021) 396–401.
[173] Y. Ge, et al., Maximizing the synergistic effect of CoNi catalyst on α-MoC for robust hydrogen production, J. Am. Chem. Soc. 143 (2) (2021) 628–633.
[174] S. Li, et al., Atomically dispersed Ir/α-MoC catalyst with high metal loading and thermal stability for water-promoted hydrogenation reaction, Natl. Sci. Rev. 9 (1) (2022) nwab026.
[175] J. Wang, et al., Variation in the In_2O_3 crystal phase alters catalytic performance toward the reverse water gas shift reaction, ACS Catal. 10 (5) (2020) 3264–3273.
[176] Y. Liu, et al., Photothermally inducing SnS_2 phase transition in Cu_2O@CuS@SnS_2 core–shell heterostructure to trigger efficient photocatalytic CO_2 reduction, Chem. Eng. J. 510 (2025) 161537.
[177] J. Wang, et al., Photochemical CO_2 hydrogenation to carbon nanotubes and H_2O for oxygen recovery in space exploration, Joule 8 (11) (2024) 3126–3141.
[178] Y. Chen, et al., Cooperative catalysis coupling photo-/photothermal effect to drive Sabatier reaction with unprecedented conversion and selectivity, Joule 5 (12) (2021) 3235–3251.
[179] T. Ding, G.W. Ho, Using the sun to co-generate electricity and freshwater, Joule 5 (7) (2021) 1639–1641.
[180] A. Zakutayev, et al., Synthesis pathways to thin films of stable layered nitrides, Nat. Synth. 3 (2024) 1471–1480.
[181] V.V. Gusev, et al., Optimality guarantees for crystal structure prediction, Nature 619 (7968) (2023) 68–72.
[182] M. Aykol, et al., Thermodynamic limit for synthesis of metastable inorganic materials, Sci. Adv. 4 (4) (2018) eaaq0148.
[183] A. Merchant, et al., Scaling deep learning for materials discovery, Nature 624 (7990) (2023) 80–85.
[184] N.J. Szymanski, et al., An autonomous laboratory for the accelerated synthesis of novel materials, Nature 624 (7990) (2023) 86–91.
[185] A. Slattery Z. Wen P. Tenblad J. Sanjosé-Orduna D. Pintossi T. den Hartog T. Noël, Automated self-optimization, intensification, and scale-up of photocatalysis in flow, Science 383 (6681), eadj1817.
[186] B. Burger, et al., A mobile robotic chemist, Nature 583 (7815) (2020) 237–241.